

---

**Three-dimensional finite-element modeling of slip  
rate variations on faults caused by glacial-interglacial  
changes in ice and water volumes: Parameter study  
and application to nature**

---

Dissertation  
zur Erlangung des akademischen Grades  
Doctor rerum naturalium (Dr. rer. nat.)  
vorgelegt der  
Ruhr-Universität Bochum  
Fakultät für Geowissenschaften

von

**Tobias Karow**

geb. am 28.07.1978 in Osnabrück

Tag der Disputation:

6.2.2009

**Gutachter:**

**Dr. Andrea Hampel**

**Prof. Dr. Bernhard Stöckhert**

**Prof. Dr. Harald Zepp**



Bochum, den 18. November 2008

## Erklärung

Hiermit versichere ich, dass ich die vorliegende Doktorarbeit ohne unerlaubte Hilfen ausgeführt und verfasst habe. Die Arbeit wurde in dieser oder ähnlicher Form an keiner anderen Fakultät oder Hochschule eingereicht.

---

(Tobias Karow)



## Abstract

Paleoseismological data indicate that many active faults in different tectonic settings experienced variations in their slip rate after the last glacial period. Examples include the post-glacial formed or reactivated Pärve and Stuoragurra reverse faults in northern Scandinavia (Lapland Fault Province), and faults being constantly active on a million year time scale like the Wasatch normal fault in the Basin and Range Province and the Dead Sea Transform fault. This work uses three-dimensional finite-element models to evaluate the response of individual faults to changes in surface load. The models consist of a lithosphere divided into an elastic upper crust, which contains the fault, a visco-elastic lower crust, and a visco-elastic lithospheric mantle. Gravity and isostasy are included in the models. By applying velocity boundary conditions, the models are deformed such that the faults develop as thrust, normal, or strike-slip faults in different experiments. A parameter study has been carried out to investigate the influence of parameters like e.g. the load thickness, the rheology, and the deformation rate on the slip rate evolution of a fault subjected to variations in the load on the Earth's surface. The results of this study show that climate-controlled changes in the volumes of ice and water bodies on the Earth's surface considerably alter the state of stress in the crust. These stress changes are large enough to affect the slip rate of an active fault. In general, faulting is suppressed or decelerated during loading and accelerated during unloading.



## Table of contents

<b>1 Introduction</b>	<b>1</b>
<b>2 Model setup</b>	<b>7</b>
2.1 Setup of the thrust and normal fault model	8
2.2 Setup of the strike-slip fault reference model	10
<b>3 Model results</b>	<b>13</b>
3.1 Results of the reference models	13
3.1.1 Results of the thrust fault reference model	13
3.1.2 Results of the normal fault reference model	17
3.1.3 Results of the strike-slip fault reference model	21
3.2 Parameter study	25
3.2.1 Influence of the load thickness on the slip rate variations	25
3.2.2 Influence of the spatial distribution of the load on the slip rate variations	28
3.2.3 Influence of the duration of unloading on the slip rate variations	34
3.2.4 Influence of the rheology on the slip rate variations	35
3.2.5 Influence of the shortening rate, the extension rate, the lateral shear velocity, and the fault dip on the slip rate variations	38
<b>4 Discussion</b>	<b>43</b>
4.1 Discussion of the results	43
4.2 Cause of the slip rate variations	45
4.3 The principal stress evolution of selected experiments from the parameter study	52
4.4 Application to natural faults	59
4.4.1 Normal faults	59
Estimation of the volume of the Lake Bonneville and Lake Lahontan water body	61
Model approach	63
Lake Bonneville, model and nature	65
Lake Lahontan, model and nature	68
4.4.2 Thrust faults	71
4.4.3 Strike-slip faults	72

## Table of contents

---

<b>5 Conclusions and outlook</b>	<b>75</b>
References	77
Acknowledgements	85
Curriculum Vitae	86



# 1 Introduction

Deformation of the Earth's brittle crust mainly occurs along discrete faults (Jackson, 2002). The slip on the fault plane and can be determined e.g. by dating the offset of stratigraphic markers or sedimentary layers in paleoseismologic trenches (e.g. McCalpin, 2002a, b). Another method is to determine the offset of geomorphic markers or uplift rates by cosmogenic nuclides (Brown et al., 1998; Hetzel et al., 2002). In situ monitoring on the fault plane is possible by using fault monitoring devices like strain-meters detecting sub-millimeter displacements on the fault (Maniatis et al., 2003). The different methods document the fault slip on different time scales. The slip on faults can differ by orders of magnitude with slip rates ranging from less than 0.1 mm/a up to the order of centimeters per year e.g. as proposed for parts of the San Andreas fault (e.g. Seagall and Harris 1986). The slip rates determined for active faults are not based on continuous motion on the fault as the term "rate" may imply. The slip rate of a fault describes the sum of discrete displacements, as a result of numerous seismic events, divided by time (Scholz, 2002). These events are the consequence of a tectonic stress field leading to crustal strain and thus to the accumulation of elastic strain energy. If the stress exceeds the critical stress of the crust, the accumulated strain energy is

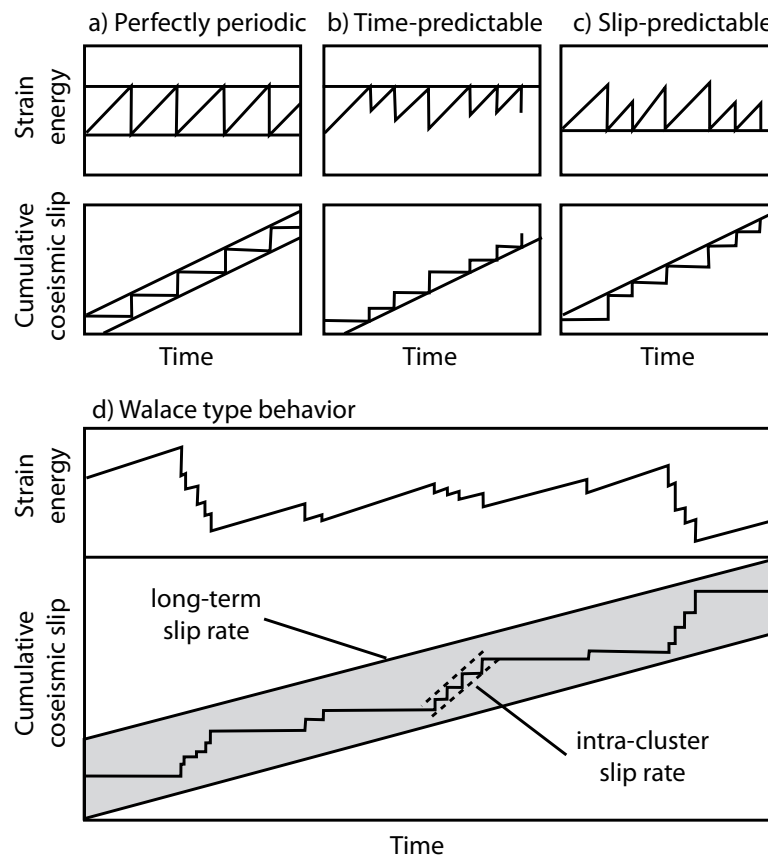


**Fig. 1:** Schematic sketches of the four earthquake recurrence models. a) Perfectly-periodic model (Reid, 1906), b) time-predictable model (Shimazaki and Nakata, 1980): the displacement during the last earthquake predicts the timing of the future earthquake, c) slip-predictable model: the time elapsed since the last earthquake predicts the displacement of the next seismic event, and d) Wallace type model: a constant long-term slip rate interrupted by short periods of clustered earthquakes leading to short-term increase of the slip rate. Modified after Friedrich et al. (2003).

released during an earthquake, leading to rupture of the crust or reactivation of preexisting faults. This way the accumulated crustal strain is converted into discrete displacement on the fault. This behavior of interseismic stress accumulation and coseismic stress release led to the development of a simple, perfectly periodic earthquake recurrence model by Reid (1910) (Fig. 1a), who assumed that the interseismic stress increase, the coseismic stress release, the crustal strain rate, and the accumulation of elastic strain energy are constant over time. This earthquake recurrence model has later been modified by Shimazaki and Nataka (1980), who added the time-predictable earthquake recurrence model, where the size of the last seismic event, i.e. the accumulated discrete slip on the fault predicts the timing of the next earthquake but not the amount of displacement that can be expected (Fig. 1b). The slip-predictable model (Shimazaki and Nataka, 1980) assumes that the time since the last earthquake can be used to predict the size of the next earthquake but not the timing (Fig. 1c). A fourth model was introduced by Wallace (1987) to account for earthquake clusters over time and for short-term slip rate changes. The Wallace type model assumes a periodic variation in the slip rate on the fault, as Schwartz and Coppersmith (1984) propose that faults tend to accumulate a similar amount of slip during each seismic event (Fig. 1d). All four earthquake recurrence models assume that the far-field displacement, which is proportional to the accumulation of strain in a crustal block, is constant over time and equal to the displacement rate recorded by earthquakes on the fault (Friedrich et al., 2003). The earthquake history of the Wasatch normal fault in the eastern Basin and Range (McCalpin and Nishenko, 1996), the Oued Fodda thrust fault in Algeria (Swan, 1988), and the Dead Sea Transform (Marco et al., 1996), reveal that the paleoseismologic record of all three fault types show a slip behavior that lacks a periodicity of the earthquake clusters during the last thousand to million years. Earthquake clustering on these faults occurs on totally variable timescales. In contrast to the slip rate variations on the Wasatch Fault, the far-field displacement rate of the Basin and Range Province has been rather constant over the last 10 Ma (Wernicke and Snow, 1998). Considering such a constant far-field displacement, this slip behavior cannot be satisfactorily explained using the Wallace-type earthquake recurrence model. This poses the question of the origin of slip rate variations on active faults. One approach to explain changes in the slip behavior of active normal faults is given by Cowie (1998) discussing the effect of the interaction of neighboring normal faults. An earthquake on a normal fault leads to the creation of stress shadows in hanging wall and footwall areas (Hodgkinson et al., 1996). According to Cowie (1998), neighboring normal faults with overlapping stress shadows experience stress feedback. Depending on the location and orientation of the fault relative to its neighbors, Cowie (1998) shows that a fault may experience rapid growth triggered by positive stress feedback or exhibit a slow growth or even ceases to slip when falling into a stress shadow zone. Cowie and Roberts (2001) predict that an along-strike array of normal faults will link over time as the faults grow, leading to accelerated slip in the center of the fault array during the linkage of the faults (Fig. 2). Stress changes in normal faulting earthquakes increase the stress levels along-strike, and thus promote the timing of future earthquakes on neighboring along-strike faults (Hodgkinson et al., 1996; Caskey and Wesnousky, 1997). The same phenomenon has been described by Iwata

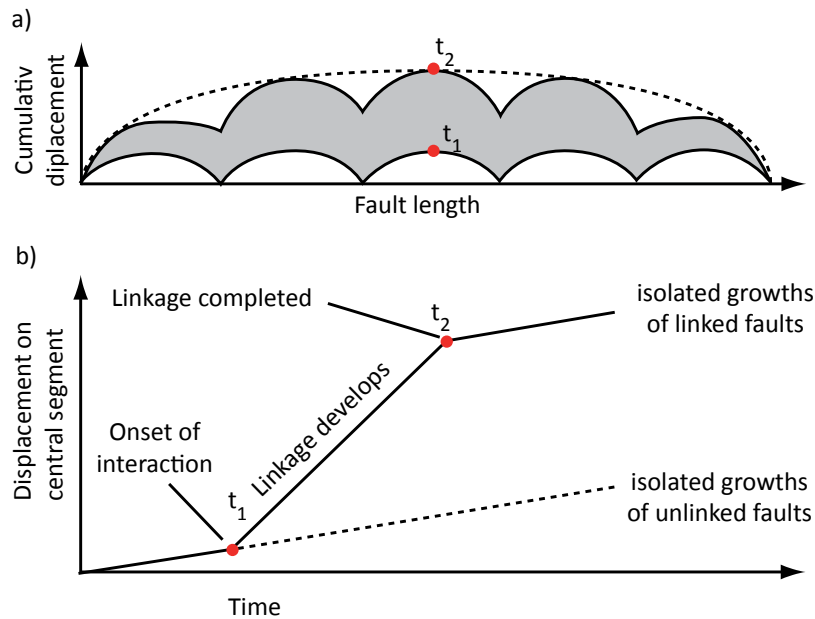


**Fig. 2:** Growth of an idealized extensional fault array. a) Displacement profile prior to interaction and after displacement profile readjustment (SB = segment boundary). b) Displacement as function of time on the central fault shows an increase in the slip rate during linkage of faults. Modified after Cowie and Roberts (2001).

and Nakanishi (2004), proposing a hastening of the occurrence of earthquakes due to dynamic triggering of neighboring faults. All these explanations of short-term slip rate variations are based on the interaction of faults, but there is evidence that short-term slip rate variations may also be caused by external input.

Data from reservoir induced earthquakes of the Koyna freshwater reservoir in India 1967, Lake Mead in the United States, Kremasta in Greece 1966, and the Hsinfengkiang Dam in China 1962, all exceeding an earthquake magnitude of  $M = 6$ , show that loading or unloading of the Earth's crust should have an impact on the stability of adjacent faults (Talwani, 2000; Gupta, 2002 and references within). The Earth's crust is considered to be close to its critical stress in tectonically active regions, which has also been proposed for tectonically quiet regions (Johnston, 1987, 1989; Zoback et al., 1989). For example the disposal of waste fluid through injection into the ground near Denver, Colorado by the U.S. Military had to be discontinued as it triggered earthquakes (Evans, 1966). Moreover Lin (2005) proposed that the construction of the 500-m-high Taipei 101 skyscraper in Taiwan lead to the trigger of several  $M_L = 3.3$  to  $M_L = 3.8$  earthquakes. The fact that load induced by artificial freshwater reservoirs or fluid injections can trigger earthquakes leads to the conclusion that a similar behavior can be expected regarding natural changes in the load on the Earth's surface.

Field studies from formerly glaciated regions like northern Scandinavia give evidence for large earthquakes forming up to 15-m-high fault scarps (Mörner, 1978; Lagerbäck, 1992; Arvidson, 1996; Dehls et al., 2000; Stewart et al., 2000; Mörner, 2005). These faults are located in the so called Lapland Fault Province. The majority of faults in this region are thrust faults, striking NNE-SSW. Two prominent examples are the 80-km-long Stuoragurra Fault (Fig. 3a) in Finnmark County in northern Norway (Dehls et al., 2000) or even larger the 150-km-long Pärve Fault in northern

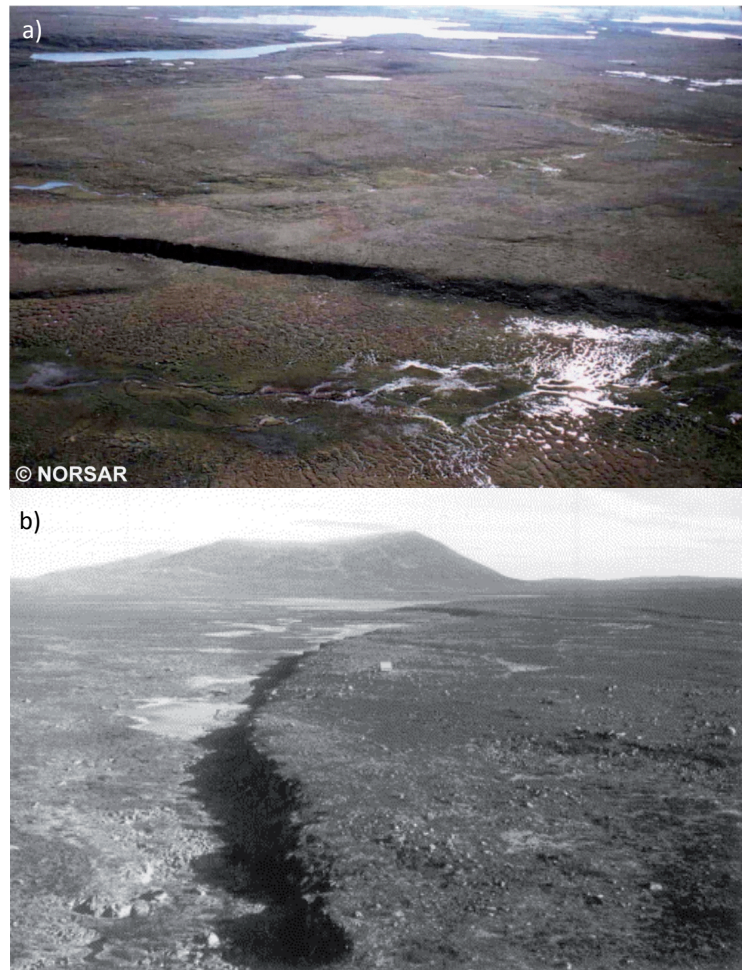


**Fig. 3:** Aerial view of the a) Stuoragurra thrust fault in Finnmark County in northern Norway (image taken from (Dehls et al, 2000) and b) the Pärve fault in northern Sweden (image taken from Lundqvist, 2000).

Sweden (Lundqvist and Lagerbäck, 1976; Lundqvist, 2000) (Fig. 3b). Being part of an old continental shield, northern Scandinavia is considered to be tectonically quiet (Johnston, 1987, 1989). Present seismic activity is reported from faults like the Stuoragurra Fault. The magnitude of seismic events normally does not exceed magnitudes of  $M_W \approx 5$  as reported by Dehls et al. (2000) and Mörner (2004). For the Pärve fault, Arvidson (1996) and Mörner (2005) estimate the magnitude of one single paleo-earthquake leading to a 150-km-long fault scarp with a displacement between 5 and 15 m to be as large as  $M_W \approx 8$ . The scarps in the Lapland fault Province offset deposits from the last glacial period making it possible to postulate a postglacial age of formation (Mörner, 1978; Lagerbäck, 1979). Data from paleoseismologic trenching in combination with dated earthquake-induced landslides and soil liquefaction phenomena document a cluster of large earthquakes in the Lapland fault Province at about 9 ka BP (Lagerbäck, 1992; Mörner, 2005).

The deglaciation of northern Sweden after the Last Glacial Maximum has been dated by luminescence data at about 9.4 – 9.2 ka BP with the ice margin retreating southwards (Lunquist and Mejdahl, 1995) and reaching the center of the Lapland fault Province at about 9 ka BP, dated by radiocarbon data of bogs (Lunquist, 1986). Both, the Pärve fault and the Stuoragurra fault have been dated to have formed postglacial right after the retreat of the glacial ice (Mörner, 1978;

Lagerbäck, 1979; Arvidson, 1996; Mörner, 2005).

The Fennoscandian Ice Shield represented a significant load to the Earth's surface causing flexure of the lithosphere with a maximum depression of over 700 m (Mörner, 1980). The removal of this mass resulted in isostatic rebound. The uplift is still continuing today with a rate of 9-10 mm/a in central Scandinavia (Ekman, 1989; Milne et al., 2001; Nocquet et al., 2005). The deglaciation of the Lapland Fault Province and the cluster of earthquakes appeared nearly coeval. This fact led to the hypothesis of postglacial faults, ruptured by earthquakes that have been triggered by the removal of large ice sheets from the Earth's surface (Mörner, 1978; Arvidson, 1996). Adams (1989, 1996) describes similar postglacial faults located in intracratonic stable eastern Canada that indicate postglacial seismicity as compiled by Adams and Basham (1989). The concept of postglacial seismicity is supported by earthquake related postglacial mud slumpings in southeastern Canada (Shilts et al., 1992) that reveal seismic activity in another region of former seismic quiescence.

Another region where the lithosphere has experienced a prominent change in the surface load is the Basin and Range Province in the central United States. This region is located between the Colorado Plateau and the Rocky Mountains to the East, and the Sierra Nevada-Great Valley Block to the West. It is characterized by north-south-trending mountain ranges which are divided by basins, both uniform in size and spacing. Some of the ranges, such as the Wasatch Mountains reach altitudes of up to 1500 m above the basins and thus were subjected to glaciation during the Last Glacial Maximum (Bartsch, 2006). Most of the ranges are delimited by a major normal fault on one side with significant slip during the Quaternary (Dohrenwend et al., 1996). The ranges are spaced about 30 km apart. The whole Basin and Range reaches a width of up to 750 km, containing 20-25 basin-range pairs (Wernicke et al., 2000).

The formation of the Basin and Range Province began between 10 to 15 Ma ago as the Sierra Nevada Block began to move westwards relative to the Colorado Plateau-Rocky Mountain area at rates of 20 mm/a in north-western direction (Wernicke and Snow, 1998). Since 10 Ma rates of 12 mm/a have been reconstructed (Hearn and Humphreys, 1998; Bennett et al., 1999; Thatcher et al., 1999; Dixon et al., 2000). This led to a total extension of about 250 km over 16 Ma (Wernicke and Snow, 1998). Today's extension rates relative to the Colorado Plateau have been determined by the Basin and Range Geodetic Network (BARGEN) to be 6-7 mm/a (Wernicke et al., 2000). During the Last Glacial Maximum many of the basins were covered by large pluvial lakes like the Lake Bonneville on the eastern border of the Basin and Range Province and the Lake Lahontan on the western border close to the Sierra Nevada-Great Valley block. Remnants of ancient Lake Bonneville, being the Great Salt Lake and Utah Lake are still visible today. Regarding the ranges in that region, e.g. like Antelope Island in the center of the Great Salt Lake, coastlines of different highstands of Lake Bonneville are also visible today (Fig. 4). Like the ice sheets in Scandinavia or Northern US, Canada and Alaska, these lakes represented a significant load to the Earth's surface, and their removal is supposed to have the same effect on the slip behavior of faults as proposed for the Scandinavian postglacial faults.

The Wasatch Fault Zone with an overall length of 370 km is the most prominent normal fault

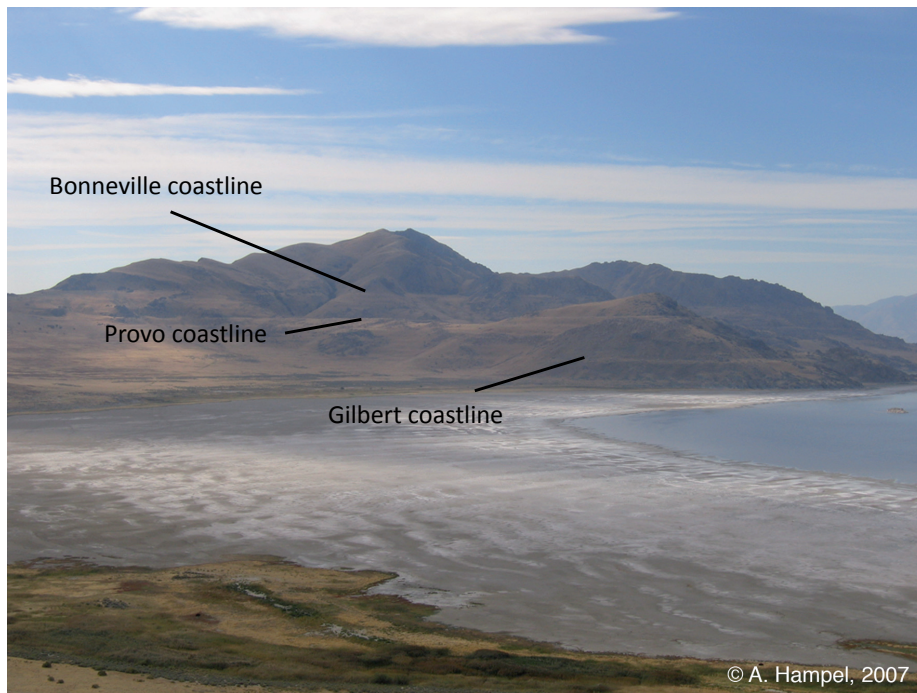


**Fig. 4:** View of Antelope Island in the center of The Great Salt Lake. Three ancient coastlines can be determined.

of the Basin and Range Province, striking from North to South and dipping westwards at  $30^{\circ}$ - $45^{\circ}$ . It is part of the Intermountain Seismic Belt which runs north-south through the Intermountain West, starting in northwestern Montana in the North and running through Wyoming, Idaho, Utah, southern Nevada and northern Arizona. The Wasatch Fault marks the eastern boundary of the Basin and Range Province with its footwall in the East, building up the Wasatch Mountains. Simultaneously the fault represents the eastern coastline of Lake Bonneville. The fault can be subdivided into ten segments (Swan et al., 1980; Schwartz and Coppersmith, 1984; Machette et al., 1991; McCalpin and Nishenko, 1996), starting with the Malad City segment in the North, being followed by the Collinston segment, the Brigham City segment, the Weber segment, the Salt Lake City segment, the Provo segment, the Nephi segment, the Levan segment and ending with the Fayette segment in the South. Paleoseismologic data show that active faults in the Basin and Range Province experience short-term variations in their slip rates. The Wasatch Fault shows an increased slip rate for the last 6 ka compared to the integrated slip rate for the last 130 ka (Friedrich et al., 2003). Data by McCalpin (2002a, 2002b) derived by trenching three segments of the Wasatch Fault Zone show a cluster of seismic events during the past 10 ka.

Both examples mentioned above, the postglacial thrust faults in Scandinavia and the normal faults in the Basin and Range seem to be influenced by more than just the tectonic stress field caused by crustal shortening or extension. Glacial unloading and rebound alter the state of stress of the lithosphere as stated for former glaciated regions (e.g. Walcott, 1970; Muir-Wood, 2000; Stewart et al., 2000). These changes of stress, related to the removal of ice have been inferred to be sufficient to affect the behavior of faults (e.g. Wu and Hasegawa, 1996a, 1996b; Johnston 1987; Johnston et al., 1998; Wu et al., 1999). Johnston (1987) proposed that large continental ice sheets

might be the reason for the lack of seismicity in Greenland and Antarctica. By using Mohr-Coulomb failure stress analysis, Johnston (1987) estimated the stress changes caused by the application of a large ice load. These analyses as well as three dimensional finite element experiments by Wu and Hasegawa (1996a, 1996b) investigating the fault stability, using Mohr-Coulomb failure stress analysis, solely regard the influence of vertical stresses, induced by an ice load, on the lithospheric stress field. In these models, the crustal stress state has been calculated for several timestamps after the Last Glacial Maximum, but these models do not contain any fault and thus make it difficult to determine fault-slip behavior during a glacial loading and postglacial unloading scenario.

A lot of attempts have been undertaken to model fault behavior, but the inability of the majority of numerical codes to implement discrete fault planes within a modeled body made it difficult to focus on the slip behavior of a fault and to quantify accumulated slip and slip rate changes. A common approach to model deformation on an orogenic scale is to implement the crust or lithosphere as a thin viscous shell consisting of a single layer of elements (England and McKenzie, 1982; Houseman and England, 1986; Medvedev and Podladchikov, 1999). The inability to model a discrete fault plane led to the implementation of finite element codes, able to handle large strain, to simulate the fault by a narrow zone of high strain or stress leading to highly deformed meshes (Willett et al., 1993; Beaumont et al., 1994; Burg and Podladchikov, 2000; Medvedev, 2002; Gerya et al., 2004; Seyferth and Henk, 2004). Beginning with two-dimensional models of normal faults consisting of a lithospheric block that was subdivided into an elasto-plastic crust and an elasto-visco-plastic lithospheric mantle, Hetzel and Hampel (2005) and later Hampel and Hetzel (2006) set up a model using the commercial code ABAQUS (Hibbitt et al., 2007). This model contained a discrete normal fault, which made it possible to investigate the slip evolution on a fault experiencing changes in the surface load. To account for isostatic flexure due to a surface load, the bottom of the model was based on springs and dashpot elements simulating the asthenosphere and giving it the ability to move vertically. Using this model approach, these two-dimensional models suggest that glacial-interglacial changes in surface loads may trigger slip rate variations on a 10 ka timescale (Hetzel and Hampel, 2005). In contrast to the models set up e.g. by Johnston (1987) or Wu and Hasegawa (1996a, 1996b) that investigated the fault stability, the model by Hetzel and Hampel (2005) or later Hampel and Hetzel (2006) put emphasis on the effect of horizontal stress evolution on the slip rate behavior of the fault. These models meant a great improvement in numerical fault modeling but still these models, due to their two-dimensional nature, were restricted to generalized plane strain and thus ignored the influence of three-dimensional effects on the stress evolution in the model, caused by surface loading and unloading.

This work is an attempt to investigate the slip behavior of faults exposed to changes in the surface load using three-dimensional finite element models of thrust faults, normal faults, and strike-slip faults. In the following a parameter study has been conducted on faults during a glacial loading and postglacial unloading cycle, where key parameters like the load and the rheology have been varied. The knowledge gained through this parameter study has been subsequently used to apply these three-dimensional models to nature, comparing the model results with field data.

## 2 Model setup

The basis for the parameter study carried out are three-dimensional finite element models of a thrust fault, a normal fault, and a strike-slip fault, constructed and solved using the finite element software ABAQUS (Hibbitt et al., 2007). For each fault type one reference model is designed reflecting the typical rheology and tectonic background for the setting. All models represent a lithospheric block including a discrete fault plane cutting through the upper crust of the lithosphere (Hetzl and Hampel, 2005; Schwarz and Henk, 2004; Hampel and Hetzel, 2006; Hampel et al., 2007). Slip on the fault is controlled by the Mohr-Coulomb failure criterion  $\tau = C + \mu \sigma_n$ . In this study a friction coefficient  $\mu = 0.4$  and a cohesion  $C = 0$  is used. Gravity is included in the model as a body force. The asthenosphere is implemented by applying springs and dashpot elements to the bottom of the model. The stiffness of the springs and the viscosity of the dashpots simulate an asthenosphere with a density of  $\rho = 3200 \text{ kg/m}^3$  and a viscosity of  $\eta_{\text{asth.}} = 1 \times 10^{19} \text{ Pa s}$ . The model is free to move in z-direction giving it the possibility to react to surface load with isostasy and flexure.

### 2.1 Setup of the thrust and normal fault model

The thrust and normal fault reference models consist of a lithospheric block with a lateral extension of 1000 km times 1000 km and a thickness of 100 km. The model lithosphere is subdivided into a 15-km-thick elastic upper crust, a 15-km-thick viscoelastic lower crust and a 70-km-thick viscoelastic lithospheric mantle (Fig. 5). The upper crust material is given a density of  $\rho = 2700 \text{ kg/m}^3$ , an elastic modulus of  $E = 0.5 \times 10^{11} \text{ Pa}$ , and a Poisson ratio of  $\nu = 0.25$ . The lower crust of the thrust fault reference model has a density of  $\rho = 2900 \text{ kg/m}^3$ , an elastic modulus of  $E = 0.7 \times 10^{11} \text{ Pa}$ , and a Poisson ratio of  $\nu = 0.25$ . The lithospheric mantle has been modeled using a density of  $\rho = 3300 \text{ kg/m}^3$ , an elastic modulus of  $E = 1.5 \times 10^{11} \text{ Pa}$ , and a Poisson ratio of  $\nu = 0.25$  (Twiss and Moores, 1992). The rheology used in the thrust fault reference model is intended to imitate the rheology of the Scandinavian shield and Alaska. The lithospheric mantle has been modeled having a higher viscosity than the lower crust, as proposed by Brace and Kohlstedt (1980), Chen and Molnar (1983) or Burov and Watts (2006) for compressional tectonic settings. The lower crust has been modeled with a viscosity of  $\eta_{\text{lower c.}} = 1 \times 10^{20} \text{ Pa s}$  and the lithospheric mantle with a viscosity of  $\eta_{\text{litho. m.}} = 1 \times 10^{23} \text{ Pa s}$ . The rheology of the normal fault reference model is designed to represent a continental extensional regime like in the Basin and Range Province, with a strong lower crust with a viscosity of  $\eta_{\text{lower c.}} = 1 \times 10^{22} \text{ Pa s}$ , underlain by a weak lithospheric mantle with a viscosity of  $\eta_{\text{litho. m.}} = 1 \times 10^{20} \text{ Pa s}$  (Nakiboglu and Lambeck, 1983; Bills and May, 1987; Bills et al., 1994, Kaufmann and Amelung, 2000; Amelung and Bell, 2003; Nishimura and Thatcher, 2003; Gourmelen and Amelung, 2005, Bills et al., 2007).

A 70-km-long fault is implemented in the upper crust in the center of the model. The fault plane cuts through the entire upper crust down to a depth of 15 km. By applying a velocity boundary



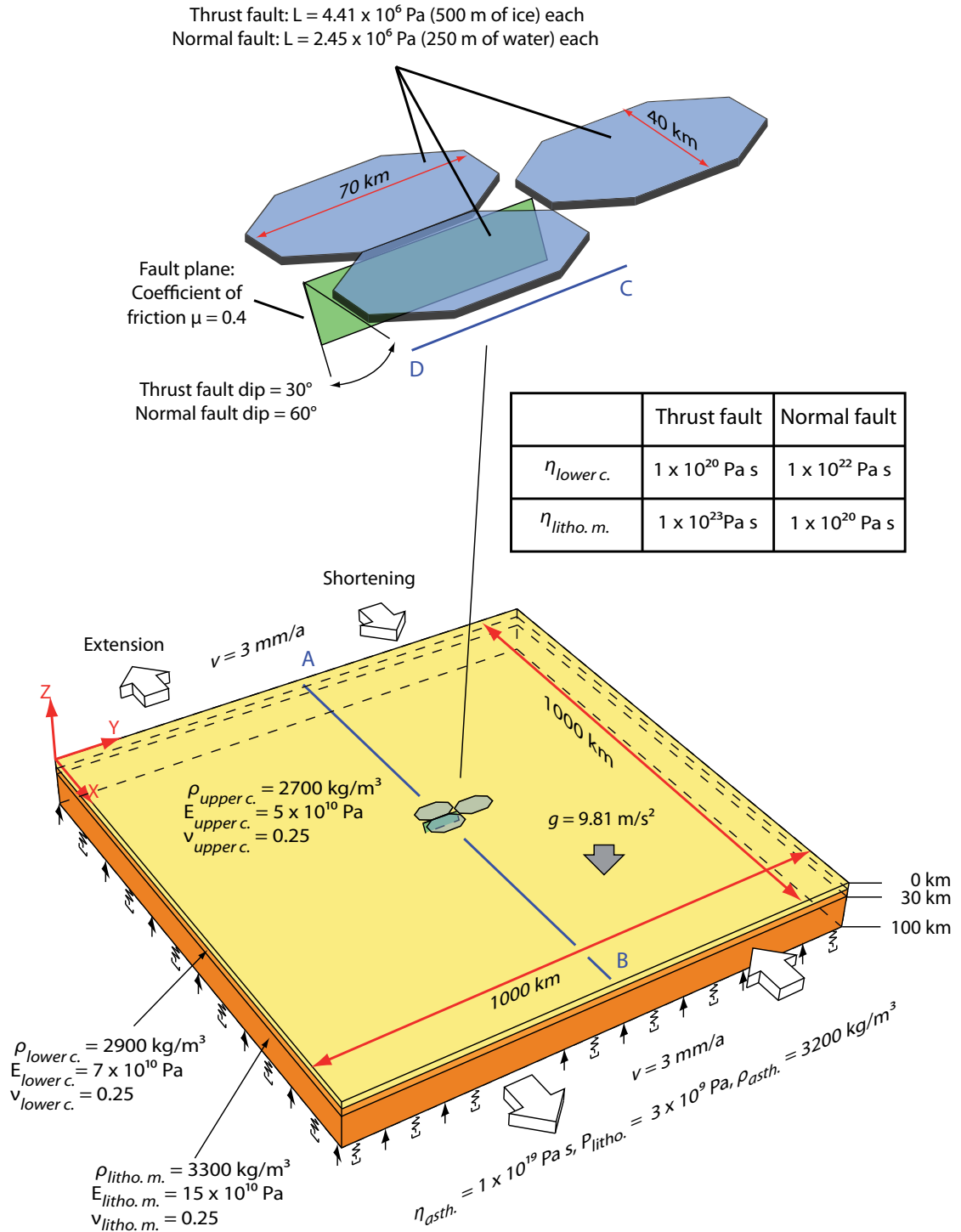


**Fig. 5:** Setup of the thrust and normal fault reference model. The rheological parameters are density ( $\rho$ ), elastic modulus ( $E$ ), Poisson ratio ( $\nu$ ), viscosity ( $\eta$ ), acceleration due to gravity ( $g$ ), surface load ( $L$ ), velocity ( $v$ ) and lithostatic pressure ( $P_{litho.}$ ). Isostasy is implemented by the boundary conditions at the bottom of the model, which is free to move in  $z$  direction. The sides of the model parallel to the  $xz$ -plane are fixed in  $y$ -direction. The model is shortened or extended by applying a velocity boundary condition to the sides in the  $y$ - $z$  plane. A 70-km-long fault is situated in the center of the model in the upper crust. The thrust fault dips with  $30^\circ$  or  $60^\circ$ . The profiles A-B and C-D show the orientations of cuts through the model.

condition, the model can be shortened or extended along the x-axis. The sides of the model parallel to shortening or extension are fixed in y-direction. According to the velocity boundary condition, the fault develops freely as a thrust or normal fault. Shortening the model at a constant rate of  $v = 6 \text{ mm/a}$  leads to the development of a compressional stress regime with the maximum principal stress  $\sigma_1$  being horizontal and the minimum principal stress  $\sigma_3$  being vertical. This stress field implies reverse slip on the fault. On the other hand, extending the model at a constant rate of  $v = 6 \text{ mm/a}$ , leads to the development of an extensional stress regime with the maximum principal stress  $\sigma_1$  being vertical and the minimum principal stress  $\sigma_3$  being horizontal. This stress regime leads to normal slip on the fault plane. Each model run is started with the activation of the velocity boundary condition resulting in slip on the fault. After an initial phase the fault reaches steady-state slip behavior. The duration of the initial phase varies between the thrust and normal fault reference models.

The models surface contains three octahedral partitions equal in shape and size, measuring 70 km times 40 km, one located on the footwall, one on the hanging wall, and one along-strike of the fault. These partitions are used to apply a pressure to the surface, in order to simulate a load. For the reference models, the load is applied to the hanging wall and footwall simultaneously. The temporal evolution of the load is controlled by a 35-ka-lasting loading function, which mimics the last glacial period loading history until today. The onset of the last major glacial advance in Northern Europe and North America started at about 35 ka BP reaching the largest lateral extension from 22 ka to 18 ka BP (Talbot, 1999). Deglaciation began at about 18 ka ago over a period of 2 ka. Accordingly, loading of the reference models starts at 35 ka BP, then linearly increases to the maximum at 22 ka BP. The maximum load is maintained until 18 ka BP before it linearly decreases to zero until 16 ka BP. In case of the thrust fault, the load represents 500 m of ice, being simulated by a surface pressure of  $L = 4.4145 \times 10^6 \text{ Pa}$ . The load in the normal fault reference model represents a 250-m-deep lake, being simulated by a surface pressure of  $L = 2.453 \times 10^6 \text{ Pa}$  (Fig. 5). The model has been meshed with tetrahedral elements (C3D4) with an average edge length of 20 km for the upper crust, the lower crust and the lithospheric mantle. The elements on the fault plane itself have an edge length of 2.5 km. This setup guarantees sufficient spatial resolution on the fault plane to investigate the slip evolution and the distribution of the slip rate on the fault, while the total number of elements in the model remains below 250000 to guarantee computational feasibility.

## 2.2 Setup of the strike-slip fault reference model

The strike-slip model is influenced by the rheology and tectonic settings of large strike-slip fault systems as the Dead Sea fault (Al-Zoubi and ten Brink, 2002). The model consists of a 20-km-thick elastic upper crust with a lateral extension of 500 km times 1000 km (Fig. 6). The elastic upper crust material is given a density of  $\rho = 2700 \text{ kg/m}^3$ , an elastic modulus of  $E = 0.5 \times 10^{11} \text{ Pa}$  and a Poisson ratio of  $\nu = 0.25$  (Twiss and Moores, 1992). In contrast to the normal fault and thrust fault model, the lower crust is simulated by springs and dashpots and not as a physical part due to the

inability of the ABAQUS code in modeling the brittle-ductile transition in a strike-slip model. The stiffness of the springs and the viscosity of the dashpots mimic a lower crust with a density of  $\rho = 2900 \text{ kg/m}^3$  and a viscosity of  $\eta = 1 \times 10^{22} \text{ Pa s}$ . Two vertical discrete fault planes are implemented in the model, cutting through the whole upper crust down to a depth of 20 km. The faults trace parallel to the 1000-km-long side of the model and meet in the center. They overlap 100 km with an offset of 30 km. The nodes at the bottom edge of the hanging wall and footwall surfaces on both implemented fault planes are tight together in vertical direction. This makes the lowest edge of the fault plane surface act like a rail, allowing the fault to slip in horizontal direction and to react to load with flexure forcing the bottom of the model to behave as one plane.

Two velocity boundary conditions applied to the long sides of the model, having an opposite sense of direction, model the tectonic background. The sides move in a dextral sense of

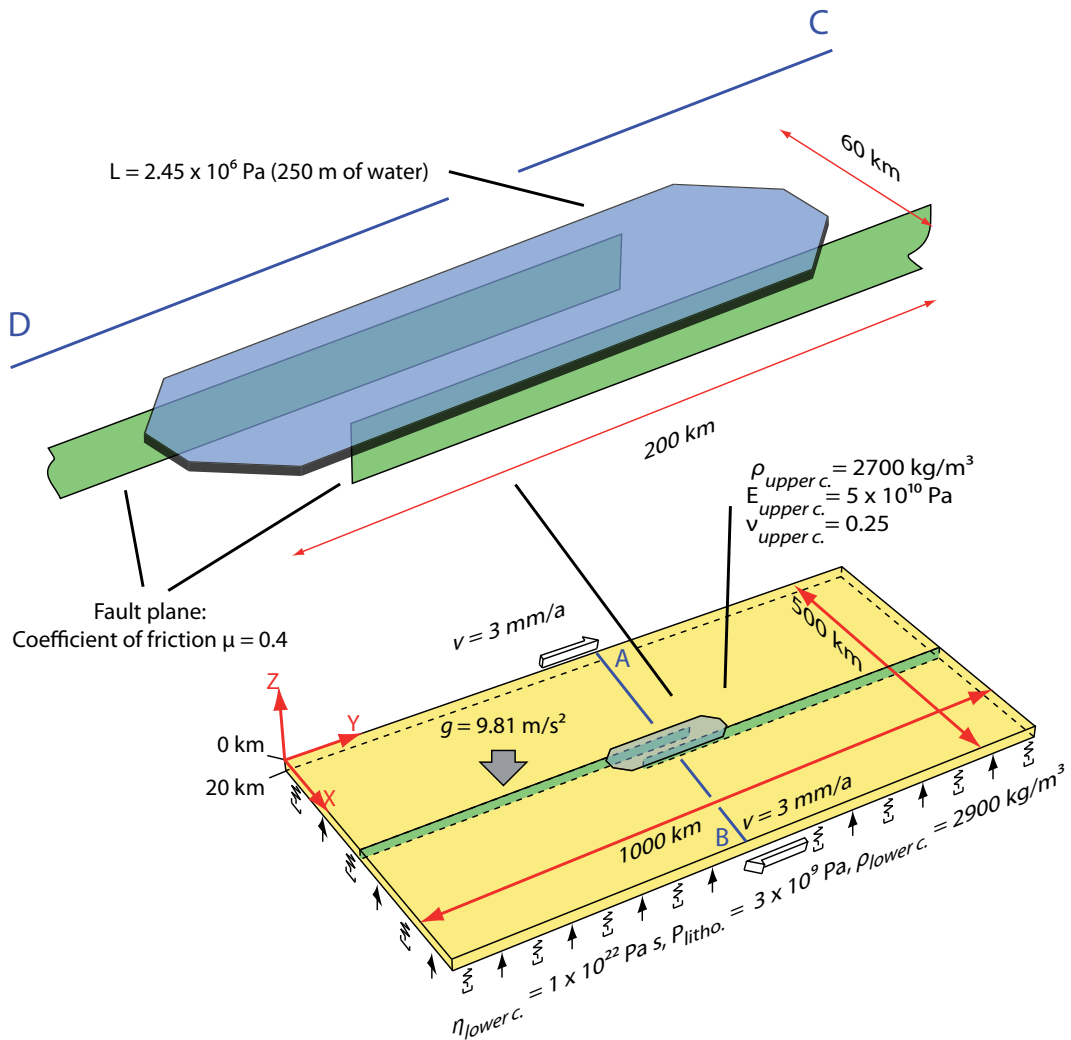


**Fig. 6:** Setup of the strike-slip fault model. The rheological parameters are density ( $\rho$ ), elastic modulus ( $E$ ), Poisson ratio ( $\nu$ ), viscosity ( $\eta$ ), acceleration due to gravity ( $g$ ), surface load ( $L$ ), velocity ( $v$ ) and lithostatic pressure ( $P_{\text{litho}}$ ). Isostasy is implemented by the boundary conditions at the bottom of the model, which is free to move in  $z$  direction. Two 550-km-long faults cut vertically through the whole upper crust, overlapping 100 km at a distance of 30 km. The sides parallel to the  $yz$ -plane are sheared in a dextral sense of motion. Slip on all faults is controlled by the Mohr-Coulomb failure criterion. Depending on the velocity boundary condition, the fault develops freely as a thrust fault, normal fault or strike-slip fault. The profiles A-B and C-D show the orientations of cuts through the model.

motion along the y-axis at a constant rate of  $v = 6 \text{ mm/a}$ . This leads to the development of a strike-slip stress regime with the maximum principal stress  $\sigma_1$  being horizontal directed in a  $45^\circ$  angle against the movement of the boundary conditions, the intermediate principal stress  $\sigma_2$  being vertical and the minimum principal stress  $\sigma_3$  being horizontal, directed in a  $45^\circ$  angle in direction of movement of the boundary conditions. The model surface contains one partition located in the center of the model, covering the area where the faults overlap. The partition is used to apply a pressure of  $L = 2.453 \times 10^6 \text{ Pa}$  to the surface, to simulate a load of 250 m of water. The load is controlled by the same 35-ka-lasting loading function as the glacial load on the thrust and normal fault reference model, imitating the last glacial period loading history until today.

### 3 Model results

For each of the three fault types, the thrust fault, normal fault and strike-slip fault, one model run has been calculated according to the parameters described in the reference model setup. The results of these reference models are followed by experiments made in order to determine the influence of parameters affecting the response of faults to glacial loading and postglacial unloading. A series of experiments has been made, changing the thickness and spatial distribution of the load and the rate of shortening, extension, or lateral shear velocity. For the thrust and normal fault models, a variety of different viscosities for the lower crust and the lithospheric mantle, the influence of the fault dip and the timing of unloading and deglaciation have been tested. All results of the parameter study will be presented, referring to the results of the reference models.

#### 3.1 Results of the reference models

The first set of results presented was obtained from the reference models. For each of the three fault types, the model run starts with the creation of isostatic equilibrium, followed by the initiation of the velocity boundary condition. After an initial phase of 1 Ma of shortening in case of the thrust fault model and 0.5 Ma of extension and dextral motion in case of the normal and strike-slip fault models, the faults slip in steady-state mode, meaning that the whole fault slips at constant slip rates.

##### 3.1.1 Results of the thrust fault reference model

During the initial phase of 1 Ma, the slip rate on the thrust fault reaches a steady-state value of 0.37 mm/a. This initial phase is followed by the application of the load to the model (Fig. 7a). With onset of glaciation the slip rate on the fault ceases. This phase lasts for about 17.5 ka, covering the interval of glacial growth, as also the interval of maximum glaciation with an invariant thickness of 500 m. At 0.5 ka after the beginning of deglaciation, which started at 17 ka model time, the thrust fault begins to slip again at a rate of 4.41 mm/a, 11.5 times faster than the initial slip rate prior to loading. This accelerated slip rate is maintained for 1.5 ka until the end of deglaciation at 19 ka model time, accumulating 6.5 m of slip and afterwards gradually decreases to the steady-state slip rate, accumulating another 0.5 m of slip before steady-state slip is reached. The whole phase of accelerated slip covers a time span of 3.5 ka during which the fault accumulates 7 m of slip. At 2 ka after the end of the removal of ice, the slip rate of the thrust fault in the reference model returns to its initial slip rate of 0.37 mm/a.

To investigate the slip distribution along the fault during glacial loading and postglacial unloading, the slip rate distribution for the fault plane has been plotted for different intervals (Fig. 7b-d). After the initial phase of the model run, the thrust fault slips at a steady-state slip rate of 0.37 mm/a, measured in the center of the fault. The slip rate decreases towards the bottom of the fault as well as towards the tips of the fault (Fig. 7b). During loading the slip on most of the fault plane

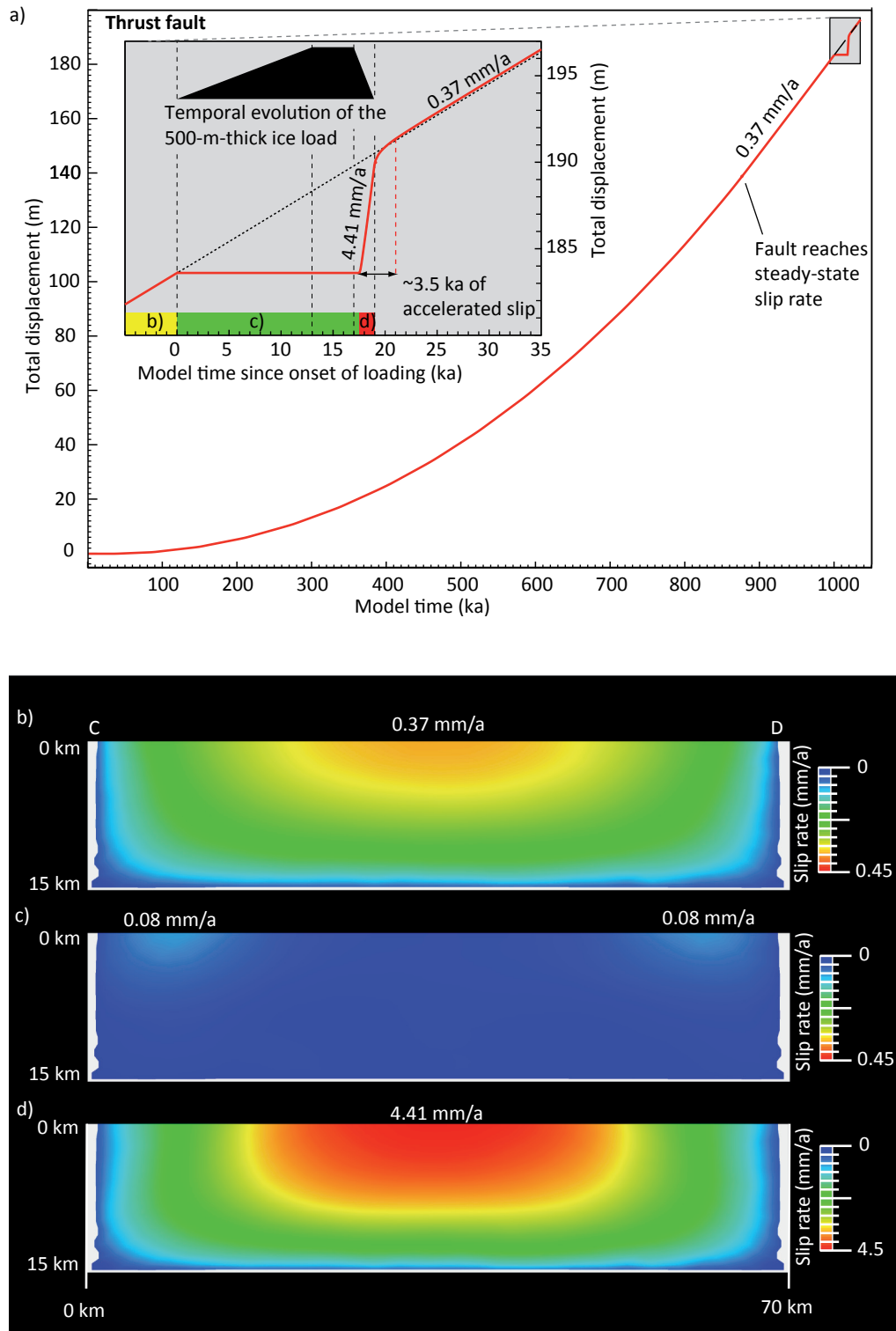


**Fig. 7:** Evolution of the fault slip history in the thrust fault reference model. Shortening of the model initiates reverse slip on the fault. A steady-state slip rate of 0.37 mm/a is reached during an initial phase of 1000 ka. The inset shows an enlarged crop of the slip history over the last 35 ka, reflecting the time phase of glacial loading and postglacial unloading of 500 m of ice. The temporal evolution of the load is schematically shown as a black polygon inlay. Note that the fault slip ceases during loading and dramatically increases shortly after the phase of unloading starts. b) – d) Contour plot of the slip rate distribution on the hanging wall of the thrust fault reference model for distinct intervals as indicated in a) as colored bars for b) the steady-state slip rate, c) loading, and d) unloading of 500 m of ice. Note that the slip rate is distributed symmetrically around the center of the fault trace. The location of the profile is shown in Figure 5.

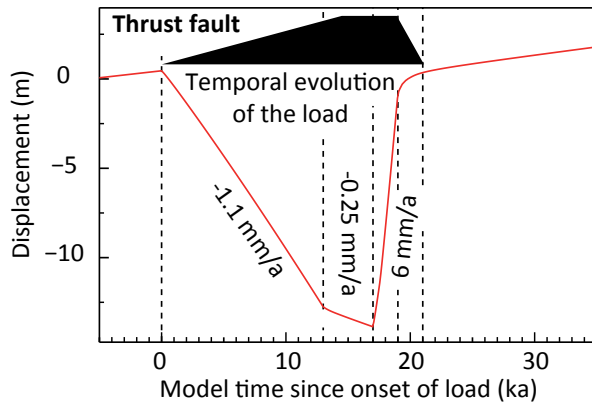


**Fig. 8:** Vertical movement at the point of maximum subsidence in the center of the thrust fault model. The temporal evolution of the load is schematically shown as a black polygon inlay. The displacement is given relative to the onset of loading at 1000 ka.

ceases. Only near the tips, the fault slips at a low rate of 0.08 mm/a (Fig. 7c). Regarding the slip rate distribution for the interval of unloading and accelerated faulting (Fig. 7d) the highest slip rate occurs at the center of the fault. Here the slip rate of 4.41 mm/a is one magnitude higher than the steady-state rate of 0.37 mm/a.

The vertical movement of the reference model during a glacial-interglacial cycle is shown by plotting the subsidence for the center of the model in Figure 8 and the vertical displacement field caused by surface loading and unloading in Figure 9a-j. The application of 500 m of ice leads to subsidence at a rate of  $-1.1$  mm/a (Fig. 9f) during the 13 ka of loading, continues at a lower rate of  $-0.25$  mm/a after the full load is applied and kept steady over 4 ka (Fig. 9g), and reaches a maximum flexure of up to  $-15$  m (Fig. 9a) prior to unloading. Isostatic rebound begins simultaneously with the

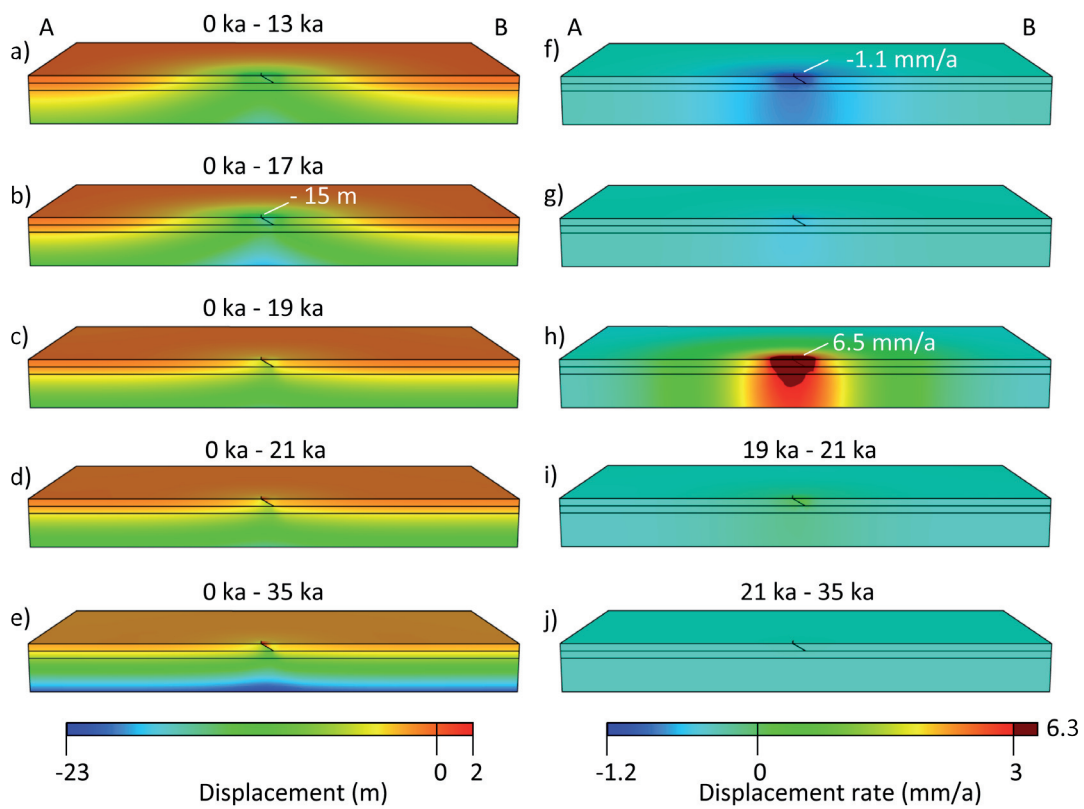


**Fig. 9:** Contour plots of the vertical movement during glacial loading and postglacial unloading. a) – e) show the displacement relative to the onset of load. f) – j) show the displacement rate for different intervals. The location of the profile is shown in Figure 5.

removal of load at 17 ka after the beginning of the glaciation-deglaciation cycle and continues until the end of the model run at 35 ka model time (Fig. 9h). Between 17 ka and 19 ka the surface uplift rate in the middle of the depression reaches values of up to 6 mm/a. This peak in the uplift rate coincides with the interval of unloading. Regarding the following 2 ka after the completion of unloading, uplift still reaches rates of 0.1 mm/a (Fig. 9i).

The horizontal movement in the reference model has been investigated by plotting the horizontal displacement rates in the model (Fig. 10a-j) along the axis of shortening, showing changes in the displacement rates during glacial loading and postglacial unloading. Regarding the center of the thrust fault reference model, an increase in the displacement rates at the surface of the model lithosphere can be seen, while the displacement rates at the bottom of the model lithosphere (Fig. 10a) decrease. In contrast, unloading leads to increased displacement rates at the bottom of the model lithosphere (Fig. 10c) and decreased displacement rates at the surface. In the 2 ka interval after the end of unloading, the horizontal displacement rates in the upper crust are higher than the ones vertically below. Towards the end of the model run, the distribution of the horizontal displacement rates returns the distribution prior to loading (Fig. 10a-e). Figure 10f-j show the

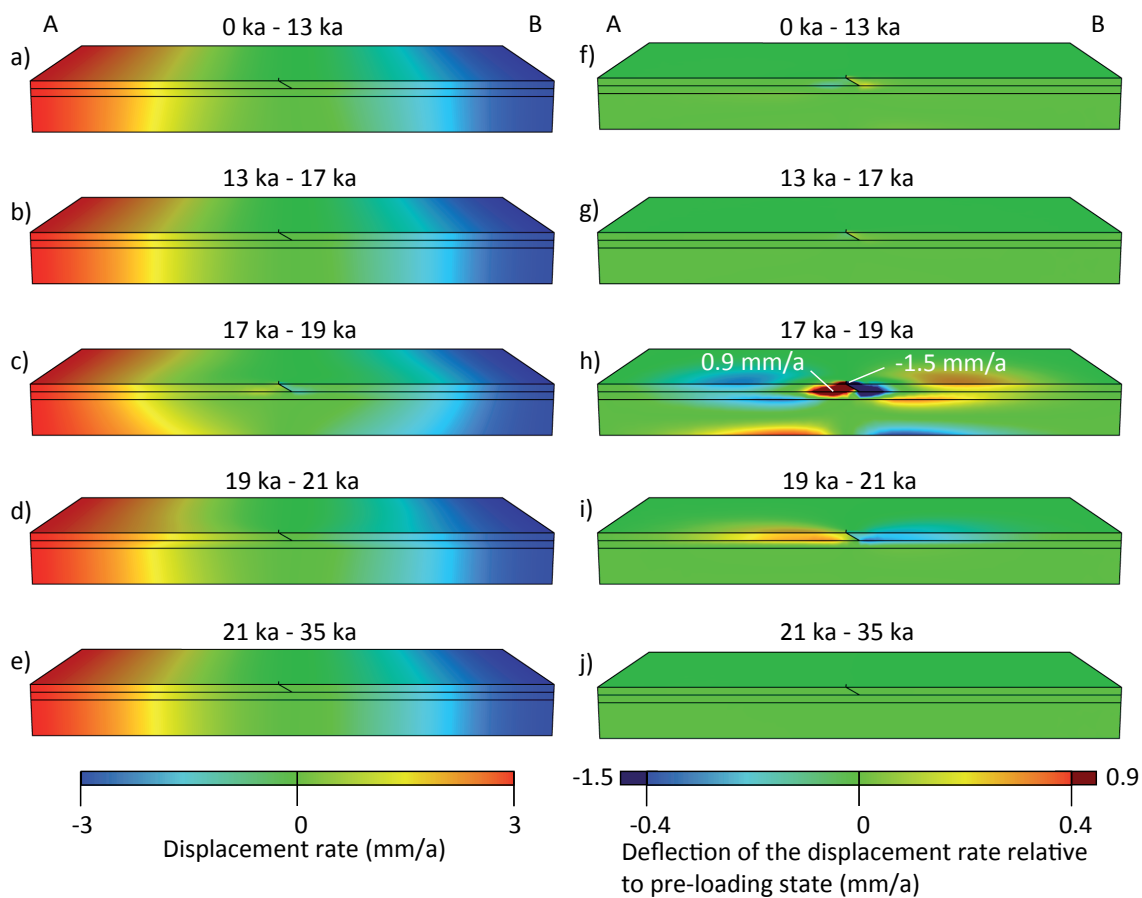


**Fig. 10:** Contour plots of the horizontal movement in direction of shortening during glacial loading and postglacial unloading. a) – e) show the displacement rate for different intervals. f) – j) show the deflection of the displacement rate relative to pre-loading state for different intervals. The location of the profile is shown in Figure 5.



deflection of the horizontal displacement rates relative to the pre-loading state. Unloading the model surface leads to an increase of the displacement rates near the fault and at the bottom of the lithospheric mantle, while at the surface and the at boundary between the lower crust and the lithospheric mantle and in the surroundings of the fault, the horizontal displacement rates decrease compared to pre-loading state (Fig. 10h). The slip rates increase up to an absolute value of 1.5 mm/a. In the 2 ka after the completion of unloading, the displacement rates in the upper crust and in the surroundings of the fault increase compared to pre-loading state (Fig. 10i). Afterwards the steady-state displacement field is recovered (Fig. 10j).

### 3.1.2 Results of the normal fault reference model

The normal fault slips with a steady-state slip rate of 0.33 mm/a in the center of the fault (Fig. 11a) prior to loading. Loading the surface of the normal fault reference model with 250 m of water decreases the slip rate to 0.22 mm/a. This phase of decelerated slip ends with the completion of loading. While the load on the surface of the lithosphere is constant, meaning no lake level changes, the slip rate of the fault approaches the steady-state rate prior to loading. Between 13 ka and 17 ka model time the fault slips at a constant rate of 0.3 mm/a. During the removal of 250 m of water, the fault slips at 1.06 mm/a in the center. This phase of maximum accelerated slip lasts for nearly 3 ka, starting from 17 ka model time and lasting until 20 ka of model time, or in other words 20 ka after the beginning of the loading-unloading cycle.

The distribution of the slip rate along the normal fault during loading due to lake level rise and unloading due to a falling lake level is shown in Figure 11b-e. The fault slips at a steady-state slip rate of 0.33 mm/a in the center of the fault, prior to loading. The slip rate distribution is equal to the distribution in the thrust fault reference model. Maximum slip occurs in the center of the fault at the surface. Loading of the model lithosphere does not affect the slip rate distribution pattern. The value of the maximum slip rate is affected, decreasing to 0.22 mm/a in the center of the normal fault. During unloading the slip rate jumps to a value of 1.06 mm/a, but the slip rate distribution stays still unaffected.

Unlike the load in the thrust fault reference model, the load used in the normal fault reference model is representative for 250 m of water as mentioned in the model setup and thus is smaller than the 500 m of ice used in the thrust fault model. Under the increasing load of the lake, the model lithosphere begins to subside (Fig. 12, Fig. 13a-j), reaching a rate of  $-1.6$  mm/a during the phase of loading between 0 ka and 13 ka (Fig. 13f). During the phase of constant load between 13 ka and 17 ka, the subsidence rate decreases to  $-0.6$  m/a. Maximum flexure of about  $-22$  m is reached right before the onset of unloading. The retreat of the lake between 17 ka and 19 ka leads to isostatic rebound with a maximum uplift rate of 7.8 mm/a (Fig. 13h). After unloading, the vertical uplift lasts on for about 2 ka between 19 ka and 21 ka at a rate of 1.3 mm/a (Fig. 13i), until the uplift rate returns to zero for the rest of the model time (Fig. 13j).

The influence of the flexure of the model lithosphere on the horizontal displacement rates is shown in Figure 14a. Loading leads to a decrease of the displacement rate in the upper crust

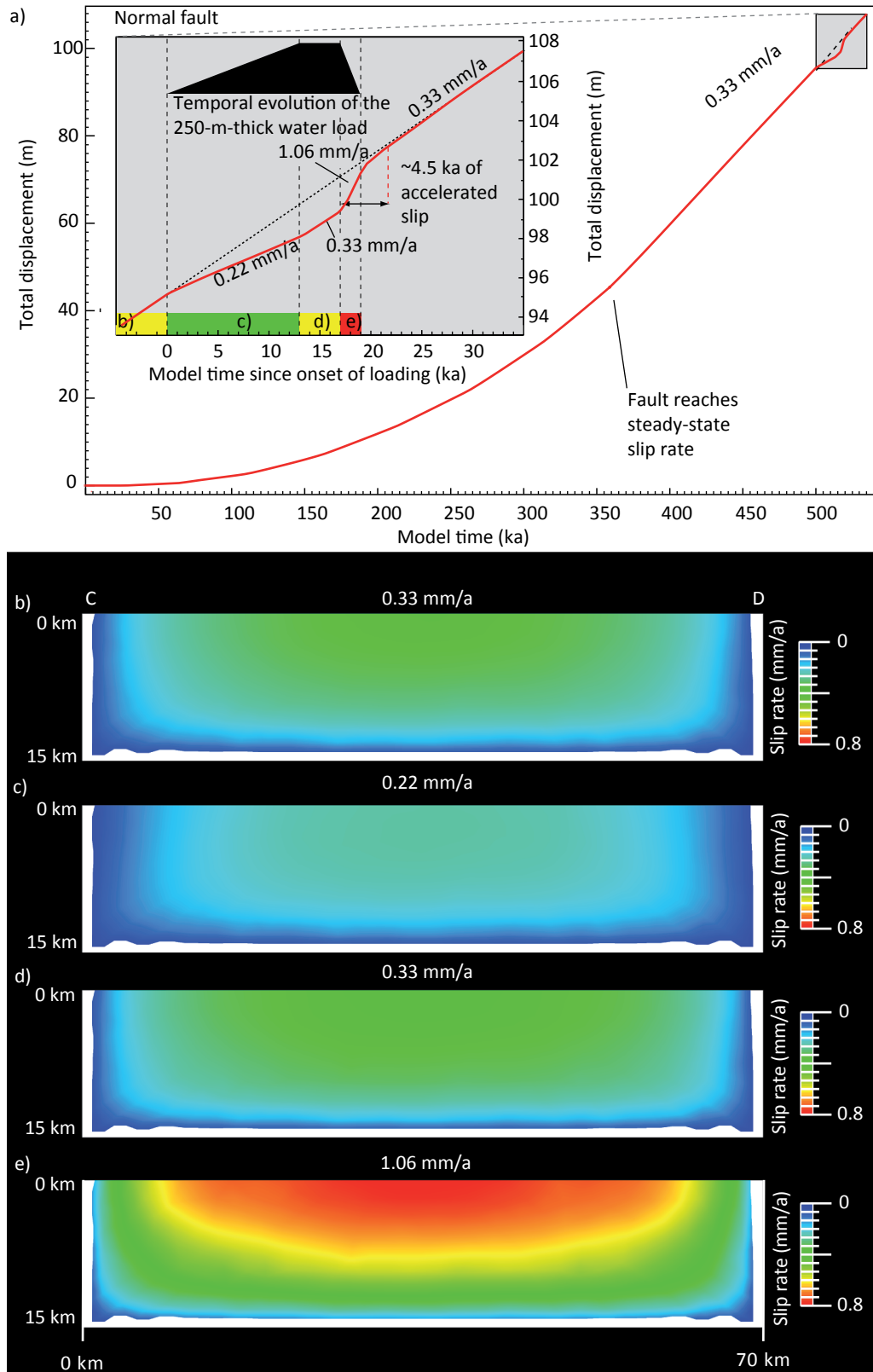


**Fig. 11:** Evolution of the fault slip history in the normal fault reference model. Extension of the model initiates normal slip on the fault. A steady-state slip rate of 0.33 mm/a is being reached during an initial phase of 500 ka. The inset shows an enlarged crop of the slip history over the last 35 ka, reflecting the time phase of glacial loading and postglacial unloading of 250 m of water. The temporal evolution of the load is schematically shown as a black polygon inlay. Note that the fault slip decreases during loading and increases during unloading. b) – e) contour plot of the slip rate distribution on the hanging wall of the normal fault reference model for distinct intervals as indicated in a) as colored bars for b) the steady-state slip rate, c) loading, d) constant load, and e) unloading of 250 m of water. Note that the slip rate is distributed symmetrically around the center of the fault trace. The location of the profile is shown in Figure 5.

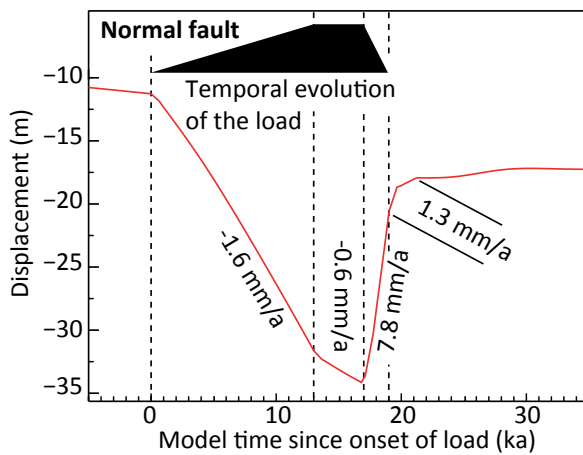


**Fig. 12:** Vertical movement at the point of maximum subsidence in the center of the normal fault model. The temporal evolution of the load is schematically shown as a black polygon inlay. The displacement is given relative to the onset of loading at 500 ka.

between 0 ka and 13 ka, while leading to an increase at the bottom of the lithospheric mantle. In contrast, unloading leads to an increase of the displacement rates in the upper crust (Fig. 14c) and a decrease in the lithospheric mantle. The effect of the growth and shrinkage of the lake on the horizontal displacement rates of the normal fault reference model becomes clearer, regarding the deflection of the horizontal displacement rates compared to the pre-loading state (Fig. 14f-j). In the loading interval from 0 ka to 13 ka (Fig. 14f) a lower displacement rate compared to the pre-loading state can be observed in the upper crust near the fault,

whereas a higher one is seen in the lower crust. During unloading this pattern turns to the opposite with an increase of the displacement rate by up to 1 mm/a in the upper crust, and a decrease in the lower crust and lithospheric mantle (Fig. 14h).

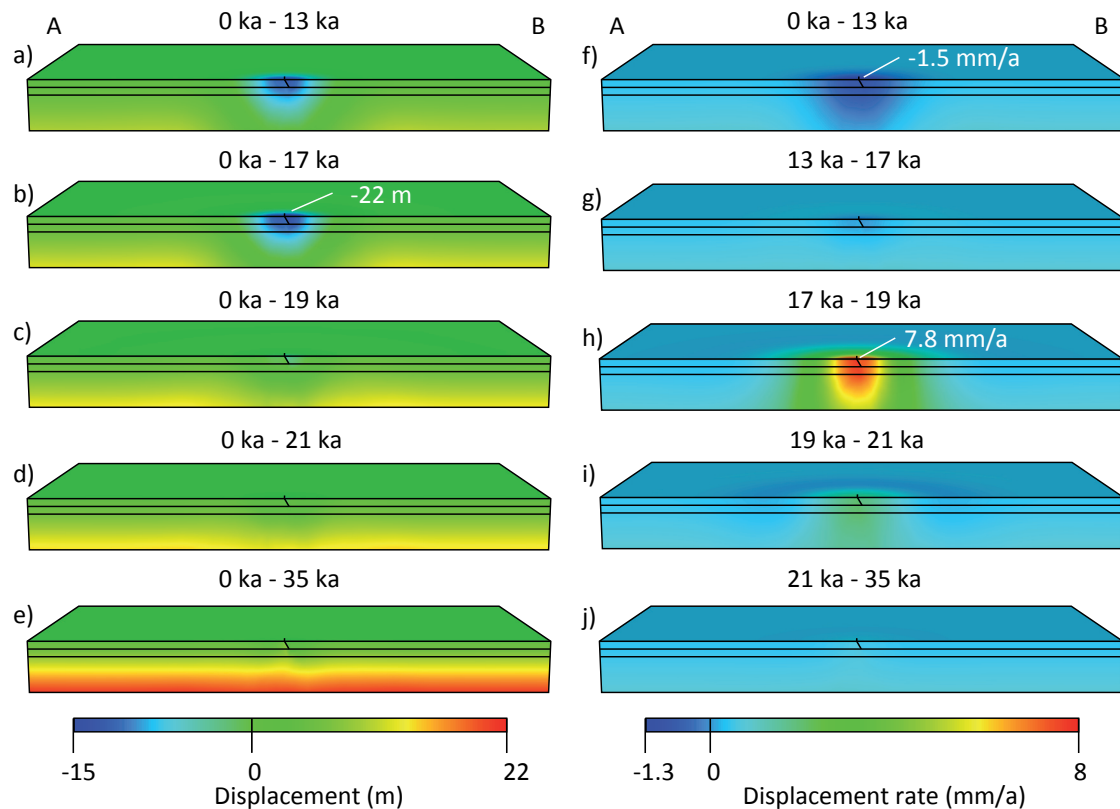


**Fig. 13:** Contour plots of the vertical movement in the normal fault model during glacial loading and postglacial unloading. a) – e) show the displacement relative to the onset of load. f) – j) show the displacement rate for different intervals. The location of the profile is shown in Figure 5.

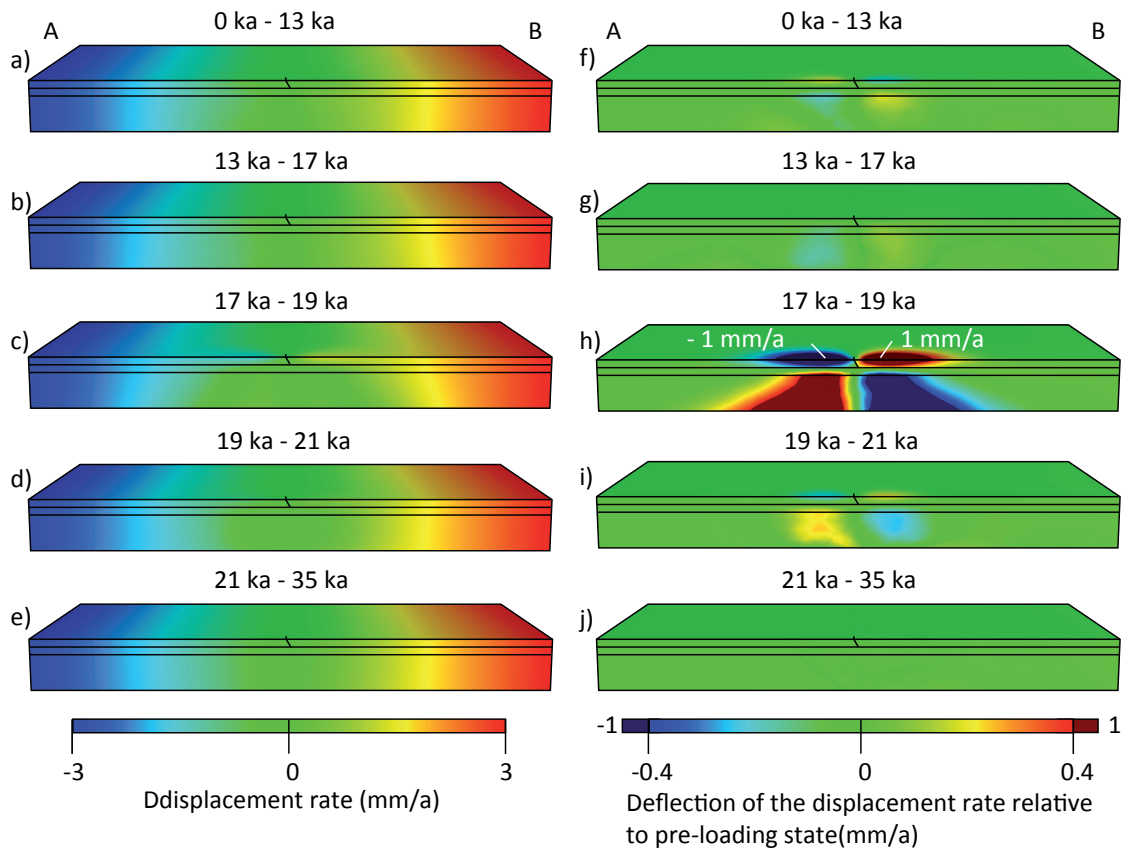


**Fig. 14:** Contour plots of the horizontal movement in direction of extension during glacial loading postglacial unloading. a) – e) show the displacement rate for different intervals. f) – j) show the deflection of the displacement rate relative to pre-loading state for different intervals. The location of the profile is shown in Figure 5.

### 3.1.3 Results of the strike-slip fault reference model

Like in the normal fault reference model, the load used in the strike-slip fault reference model is representative for 250 m of water. The reference curves for the slip rate are measured at four points, two (P1, P4) located at the intersection of the fault trace with the boundary of the surface partition representing the spatial distribution of the load, and two points (P2, P3) located in the center of the load as sketched in the inset in Figure 15. The strike-slip fault reaches steady-state slip at about 0.36 Ma and 0.37 Ma after the onset of dextral motion at the points chosen for this analysis. In the reference model the fault slips at a steady-state rate of 2.21 mm/a in the center of the model (P2, P3) and at 3.69 mm/a at the points on the edge of the surface partition (P1, P4). With the onset of loading, filling the 250 m deep lake on the surface of the lithosphere, the slip rate on the faults decreases from 2.21 mm/a prior to loading to 1.72 mm/a for the slip histories of P2 and P3, and from 3.69 mm/a to 3.20 mm/a at P1 and P4. These slip rates are valid until the end of the loading phase at 13 ka model time when the lake level reaches 250 m. This phase is followed by a 4-ka-lasting interval of constant load in which the fault slips at 2.18 mm/a (P2, P3 (Fig. 15)) and 3.64 mm/a (P1, P4 (Fig. 15)). These slip rate values are relatively close to the steady-state slip rate values of 2.21 mm/a (P2, P3 (Fig. 15)) and 3.69 mm/a (P1, P4 (Fig. 15)) prior to loading. Unloading the model leads to an immediate increase of the slip rate. The accelerated slip rate at P2

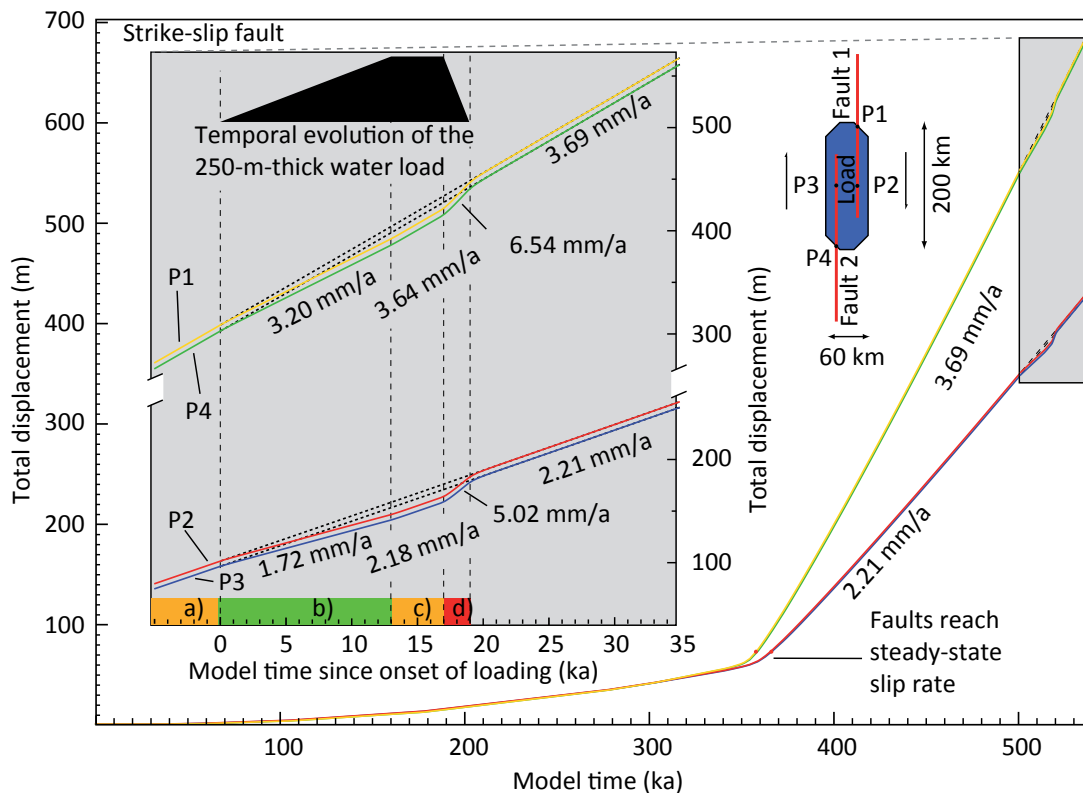


**Fig. 15:** Evolution of the fault slip history in the strike-slip fault reference model. Dextral motion of the model sides initiates strike-slip on the two faults and a steady-state slip rate of 2.21 mm/a at P1 and P4, and 3.69 mm/a at P2 and P3 is reached during an initial phase of 500 ka. The inset shows an enlarged crop of the slip history over the last 35 ka, reflecting the time phase of glacial loading and postglacial unloading of 250 m of water. The temporal evolution of the load is shown as a black polygon inlay. Note that the faults slip decelerates during loading and increases during unloading.

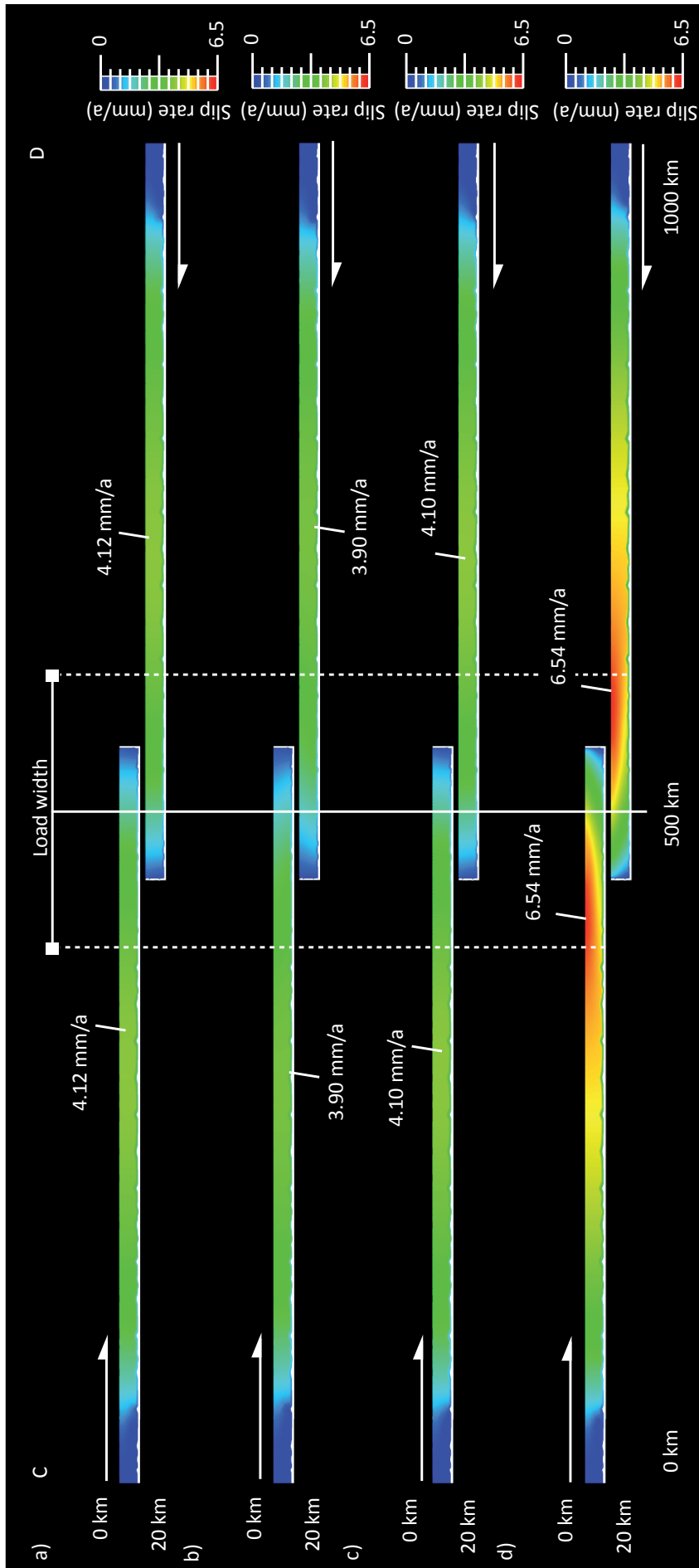


**Fig. 16:** Contour plot of the slip rate distribution on the hanging wall of the strike-slip fault reference model for distinct intervals as indicated in Figure 15 as colored bars for a) the steady-state slip rate, b) loading, c) constant load, and d) unloading of 250 m of water. Note that the slip rate is distributed symmetrically around the center of the model. The location of the profile is shown in Figure 6.

and P3 is 5.02 mm/a, and at P1 and P4 6.54 mm/a. At 0.5 ka after the removal of the load, the phase of accelerated slip ends and the slip rate of both faults returns to the steady-state values of the pre-loading state.

Fig. 16a-d shows the slip rate along both faults for distinct intervals, indicated by colored bars in Figure 15. The maximum steady-state slip rate occurs at the top of the fault, reaching rates of 4.12 mm/a (Fig. 16b). During lake level rise (Fig. 16c) the point of maximum slip rate shifts from the top to the bottom of the fault, decelerating to a value of 3.9 mm/a. In the phase of the lake highstand with invariant lake level, the slip rate distribution returns to the pattern of the steady-state slip rate with the fault slipping at 4.1 mm/a (Fig. 16d). During lake level fall, the slip rate increases to 6.54 mm/a (Fig. 16e).

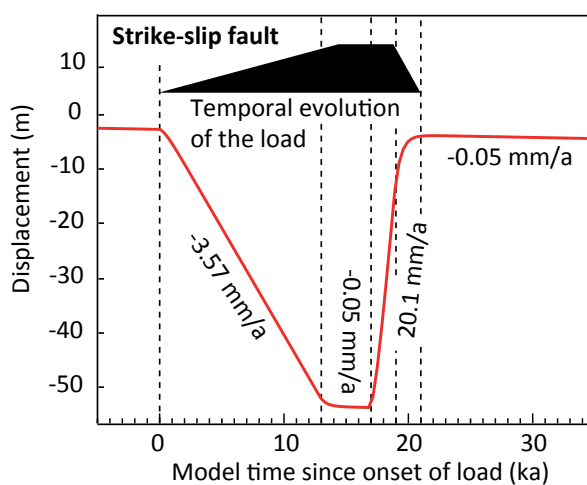


**Fig. 17:** Vertical movement at the point of maximum subsidence in the center of the strike-slip fault model. The temporal evolution of the load is schematically shown as a black polygon inlay. The displacement is given relative to the onset of loading at 500 ka.

Regarding the point of maximum subsidence, the application of 250 m of water leads to subsidence of up to -50 m (Fig. 17). With the beginning of lake level rise, the center of the model begins to move downwards at a rate of -3.57 mm/a, slowing down to -0.05 m/a during lake highstand, lasting until the onset of lake level fall. The interval of maximum subsidence rate coincides with the interval of lake regression on the surface of the model lithosphere (Fig. 18, Figure 18a-j), causing isostatic rebound at a maximum uplift rate of 20.1 mm/a, measured between 17 ka and

19 ka (Fig. 17, Fig. 18h). The horizontal displacement rates in direction of the dextral strike-slip motion show a slight decrease during lake level rise (Fig. 19a-e). A falling lake level leads to a remarkable increase of the horizontal displacement rate, seen as the red area near the fault (Fig. 19h), and to a still slightly higher displacement rate in the 2 ka interval after lake regression between 19 ka and 21 ka, seen as the yellow area near the fault. The residual horizontal displacement rate (Fig. 19f-j) shows a decrease in horizontal displacement during the phase of lake level rise and an increase of up to 3.29 mm/a over the pre-loading displacement rate during lake regression.

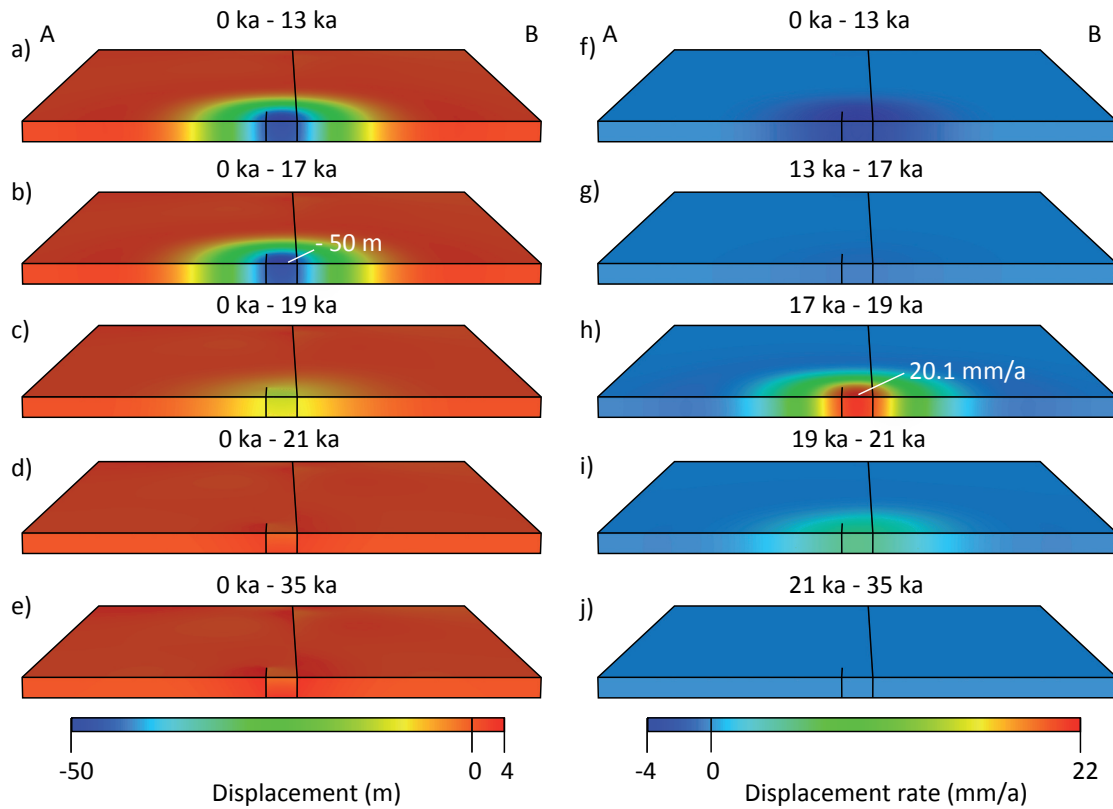


**Fig. 18:** Contour plots of the vertical movement in the strike-slip fault model during glacial loading and postglacial unloading. a) – e) show the displacement relative to the onset of load. f) – j) show the displacement rate for different intervals. The location of the profile is shown in Figure 6.

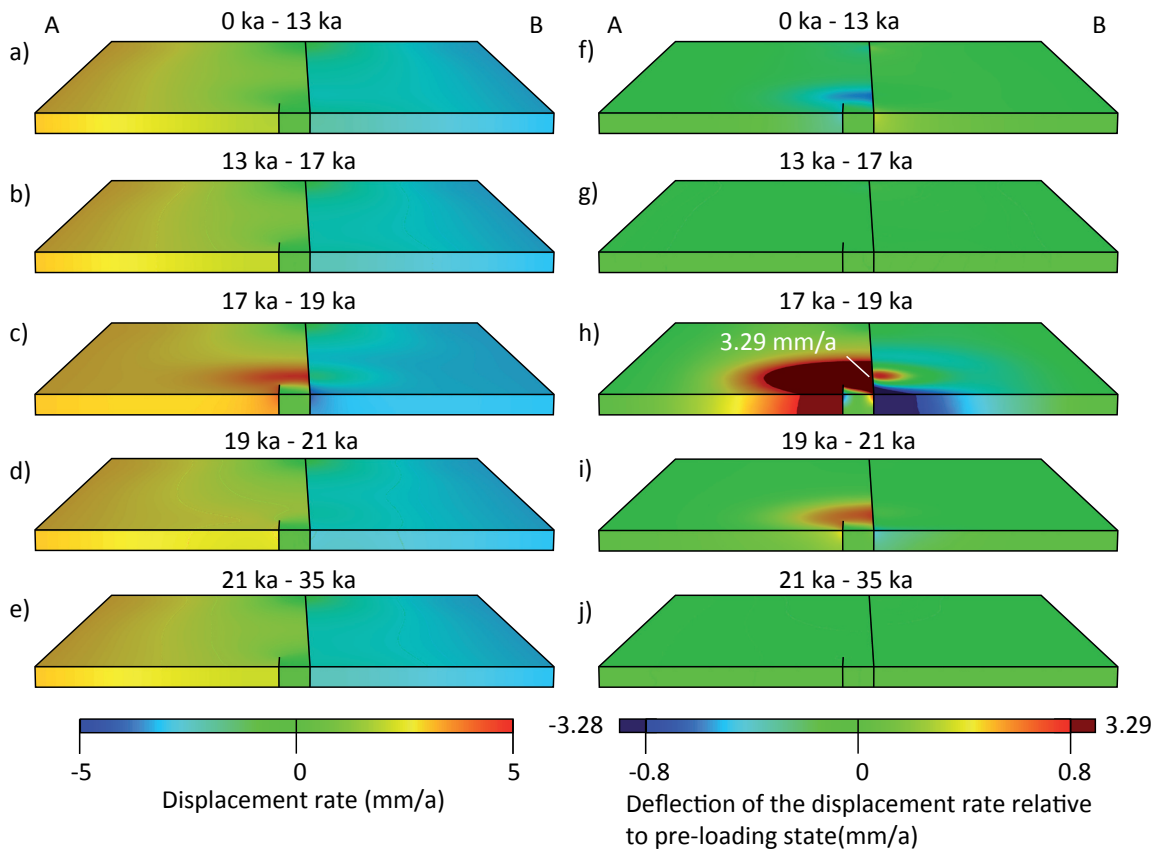


**Fig. 19:** Contour plots of the horizontal movement in direction of dextral movement of the strike-slip fault during glacial loading and postglacial unloading. a) – e) show the displacement rate for different intervals. f) – j) show the deflection of the displacement rate relative to pre-loading state for different intervals. The location of the profile is shown in Figure 6.



## 3.2 Parameter study

After presenting the results of the three reference models, each of the parameters tested in the following experiments will be presented for the different fault types, starting with the influence of the thickness, spatial distribution, and the timing of the load, followed by the influence of the rheology, the influence of the velocity boundary condition, and the fault dip on the slip rate variation of each fault. Apart from the experiments made to investigate the influence of the timing of the load, all experiments use the same 35-ka-lasting loading function as the reference models do.

### 3.2.1 Influence of the load thickness on the slip rate variations

The influence of the load on the slip rate variations has first been tested on the thrust fault model, by varying the ice thickness between 100 m and 2000 m, representing the average thickness of a glaciated mountain range up to an area covered by a large ice sheet. In all thrust fault experiments the slip rate of the fault decreases during glaciation whereas deglaciation leads to a remarkable increase of the slip rate (Fig. 20). In the experiments with ice loads of 500 m and thicker, the fault slip ceases with the onset of glaciation until deglaciation starts, covering the 4-ka-long phase of maximum ice thickness. First the fault of the reference model starts to slip at 0.5 ka after the onset of deglaciation, at 0-7 ka the fault in the experiment with 1000 m of ice follows. At 1.5 ka after the onset of deglaciation the fault in the experiment with 2000 m of ice starts to slip again. In the experiments with 250-m-thick ice and less, the slip rate of the fault decreases during the glaciation. In the experiment with 100-m-thick ice, the slip rate decreases to 0.23 mm/a during glaciation and returns to the steady-state value of the slip rate of 0.36 mm/a while the glacial load is kept constant for 4 ka. The 250-m-thick ice load decelerates the slip on the fault to a slip rate of 0.02 mm/a during loading. Here the slip on the fault nearly returns to the steady-state slip rate with 0.36 mm/a during the 4-ka-long phase of maximum ice thickness. With the onset of deglaciation at 17 ka, both experiments (100 m and 250 m of ice) show an immediate increase in the slip rate (Fig. 20), returning to steady-state slip at 20 ka of model time, 1 ka after deglaciation has been completed. The slip rate increase in the experiment with 100 m of ice during unloading is the smallest value observed in the set of all experiments for the thrust fault model varying the thickness of the glacial load. The deglaciation of 100 m of ice over 2 ka leads to a slip rate of 1.20 mm/a, which is 3.2-fold higher than the steady-state slip rate of 0.37 mm/a. Unloading of 2000 m of ice gives the highest slip rate increase with 14.25 mm/a, 38.5-fold higher than the steady-state slip rate. The phase of accelerated slip lasts 2.5 ka in the experiments with 100 m and 250 m of ice and up to 3.5 ka in the experiment with 2000 m of ice. The comparison of all experiments reveals that the phase of maximum slip rate gets shorter with increasing maximum ice thickness, while simultaneously the value of the maximum slip rate during this phase increases drastically. The accumulated slip during the phase of accelerated slip ranges from 2.28 m in the experiment with an ice load of 100 m to 8.63 m in the experiment with an ice load of 2000 m.

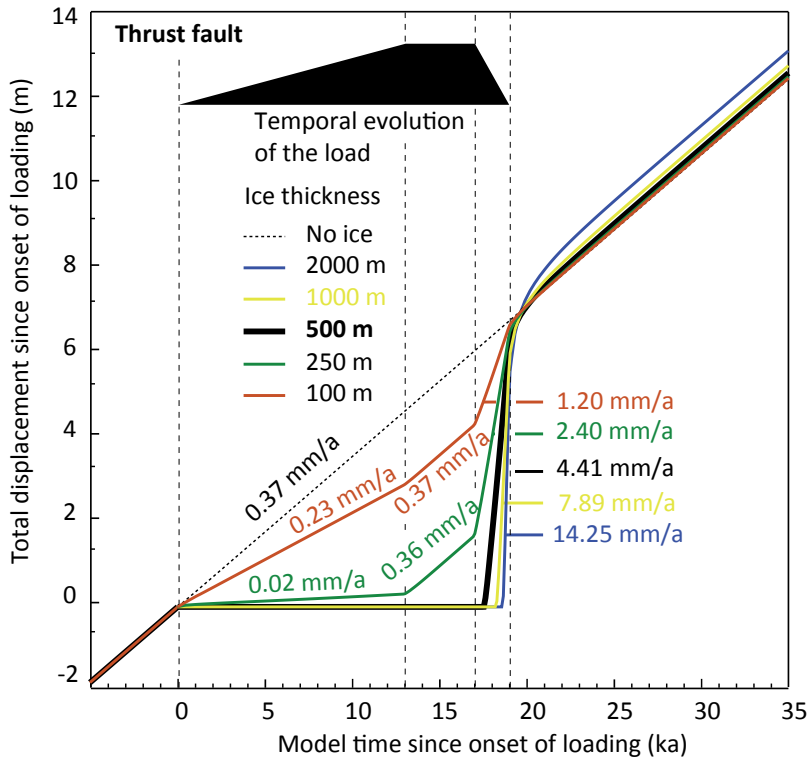


**Fig. 20:** Slip history plot of the thrust fault experiments with varying thickness of the ice load. Note the different slip rates during loading and the phase of constant load especially for the ice loads thinner than 500 m. The temporal evolution of the load is indicated by the black polygon inset. The slip history of the reference model is indicated by the thick black curve.

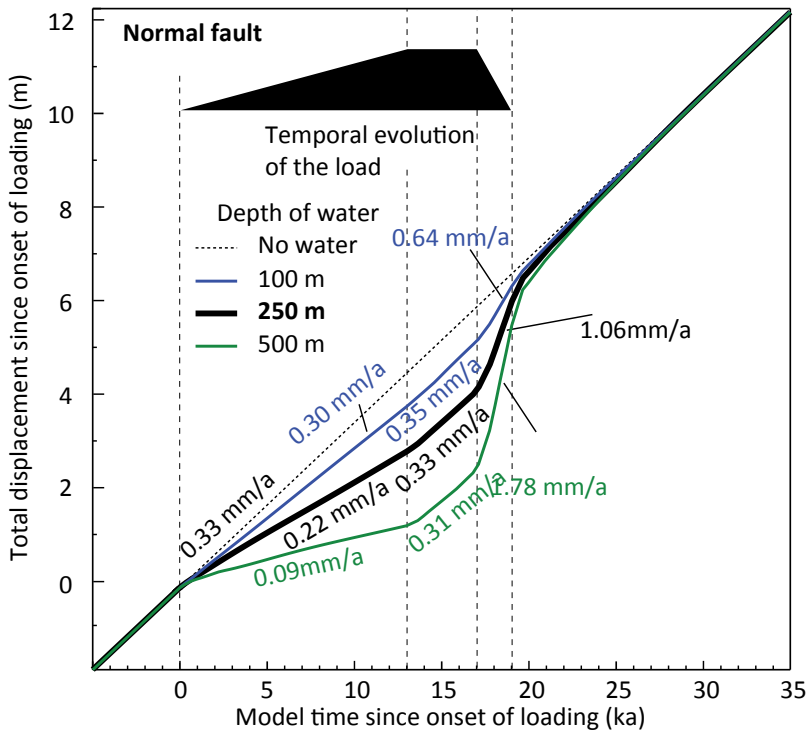


**Fig. 21:** Slip history plot of the normal fault experiments with varying lake levels. The temporal evolution of the load is indicated by the black polygon inset. The slip history of the reference model is indicated by the thick black curve.

In the set of experiments with varying water bodies calculated for the normal fault model, a similar influence of the load size on the slip rate behavior of the fault, as in the set of experiments made for the thrust fault model, can be observed. In contrast to these thrust fault experiments, changing the magnitude of the water load, does not affect the timing of the normal fault slip history (Fig. 21). Two experiments have been made testing the fault slip behavior for a 100-m-deep and a 500-m-deep lake. Both experiments show a slip rate close to the steady-state slip rate during lake highstand. The slip on the fault of the reference model with a load of 250 m of water decelerates to 0.22 mm/a during lake level rise and accelerates to 0.81 mm/a during lake regression. The application of a 100-m-deep water body to the surface of the model leads to a decelerated slip rate of 0.30 mm/a during lake level rise and an increased slip rate of 0.64 mm/a during regression of the lake (Fig. 21). In contrast, a load representing 500 m of water leads to a decreased slip rate of 0.09 mm/a in the phase of lake level rise and an increased slip rate of 1.78 mm/a in the phase of lake regression. In both experiments the phase of maximum accelerated slip lasts for 3 ka, 1 ka longer than the removal of the lake until 20 ka model time. In the experiment calculated for a 100-m-deep lake the slip rate returns to the steady-state value of 0.37 mm/a, 1.5 ka after the lake disappears. In the experiment solved for the 500-m-deep lake, the phase of accelerated slip ends 4 ka after the complete removal of the lake and thus last 2 ka longer than the lake regression.

The strike-slip model has been tested for the same water-depth of 100 m and 500 m of water, as used in experiments for the normal fault model. To investigate the slip rate behavior of the strike-slip fault, the slip rate has been measured at two points P1 and P2 on the faults as shown in the sketch in Figure. 15. As the slip rates at P3 and P4 behave similar to the ones measured at P1 and P2 they have been excluded from the following plots. Again, changing the maximum depth of the water load applied to the surface has no effect on the timing of the slip rate changes of the strike-slip fault (Fig. 22). The slip on the fault of the reference model with a water load of 250 m depth decelerates to 3.2 mm/a at P1 and to 1.72 mm/a at P2 during lake level rise. During regression of the lake, the slip accelerates to 6.54 mm/a (P1) and 5.02 mm/a (P2). The application of a 100-m-deep lake to the surface of the model leads to a decelerated slip rate of 3.48 mm/a (P1) and 1.72 mm/a (P2) during lake level rise and an increased slip rate of 4.75 mm/a (P1) and 3.22 mm/a (P2) during lake regression (Fig. 22). The 500-m-deep lake affects the slip rate of the normal fault by decreasing the slip rate to 2.70 mm/a (P1) and 1.24 mm/a (P2) in the phase of rising lake level and increasing the slip on the fault to a rate of 9.44 mm/a (P1) and 7.89 mm/a (P2) in the phase of lake regression. Both experiments show a slip rate close to the steady-state slip rate during the lake highstand. The phase of maximum accelerated slip lasts for 2 ka in both experiments, concerning the experiment with a 100-m-deep and a 500-m-deep lake. This phase ends with the end of the lake regression at 19 ka model time.

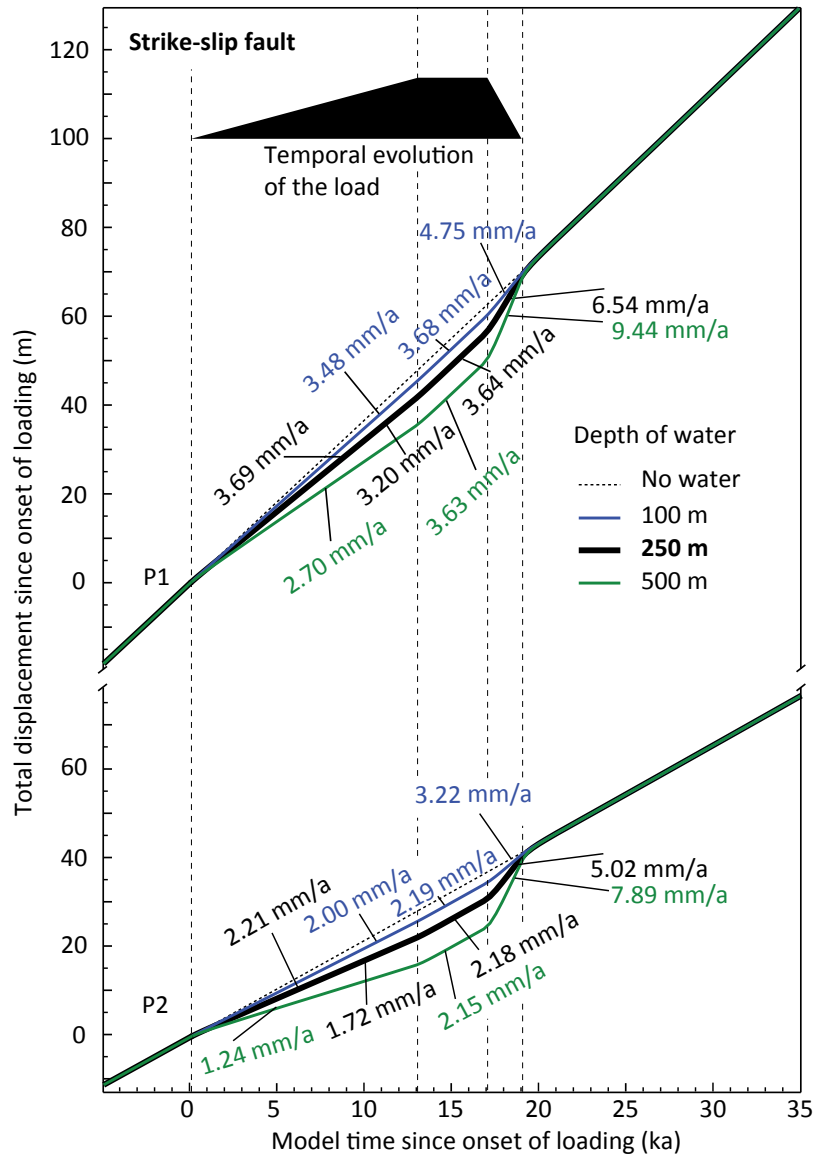


**Fig. 22:** Slip history plot of the strike-slip fault experiments with varying lake levels. The temporal evolution of the load is indicated by the black polygon inset. The slip history of the reference model is indicated by the thick black curve.

### 3.2.2 Influence of the spatial distribution of the load on the slip rate variations

In the second set of experiments, the distribution of the load is varied between load on the footwall, on the hanging wall, and load along-strike of the fault opposite to fault tip. These three constellations of load distribution have been tested for the thrust fault and the normal fault model. In case of the thrust fault model these three load settings have been tested for 500 m of ice, according to the load used in the reference model and also for 2000 m of ice (Fig. 23). In the experiments with glacial load on the hanging wall, the fault ceases to slip. The slip history matches exactly the curve of the reference model for the experiment with 500 m of ice (Fig. 23a). Regarding the slip history for the model run in which the hanging wall is loaded with 2000 m of ice (Fig. 23b), the same effect as in the first set of experiments with varying load thickness can be seen. The thicker the ice, the longer is the gap between the onset of deglaciation and reactivation of slip on

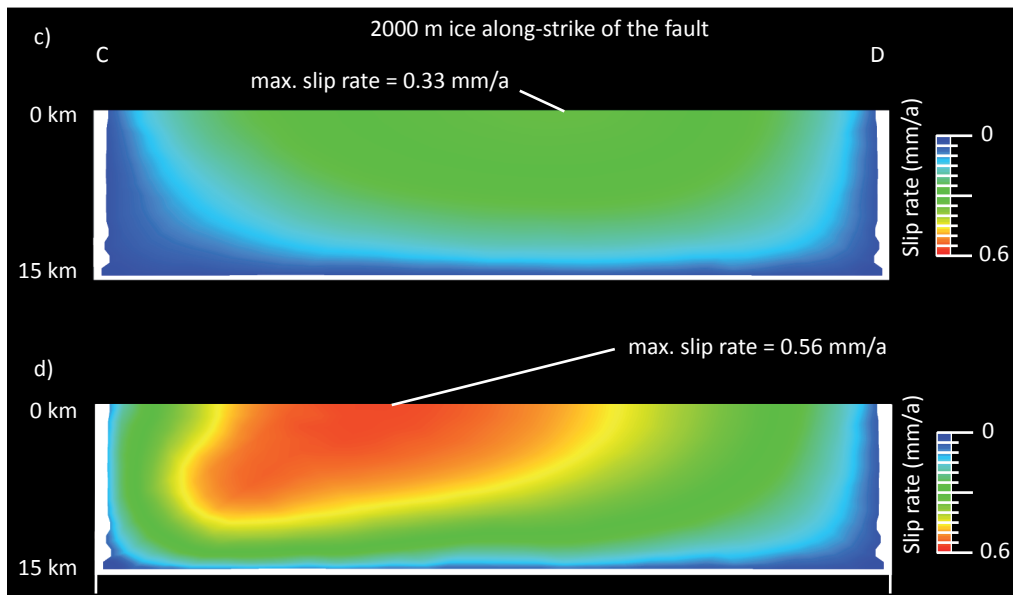
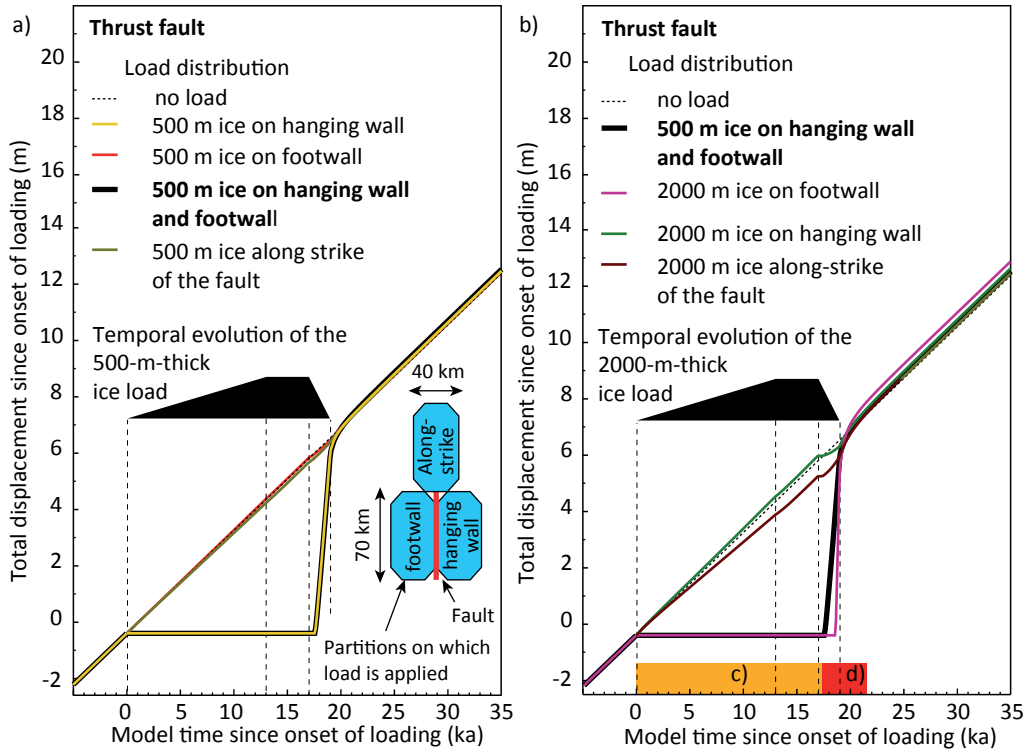


**Fig. 23:** Slip history plot of the thrust fault experiments with varying distribution of the ice load for a) 500 m and b) 2000 m of ice. The location of the surface partitions to which the load is applied is sketched by the blue octagons. The temporal evolution of the load is indicated by the black polygon inset. The slip history of the reference model is indicated by the thick black curve. c), d) Slip rate distribution on the hanging wall for the loading and unloading phase of 2000 m of ice to along-strike of the fault. The intervals are indicated in b) by colored bars. Note the asymmetric slip rate distribution in c) and d). The location of the profile is shown in Figure 5.

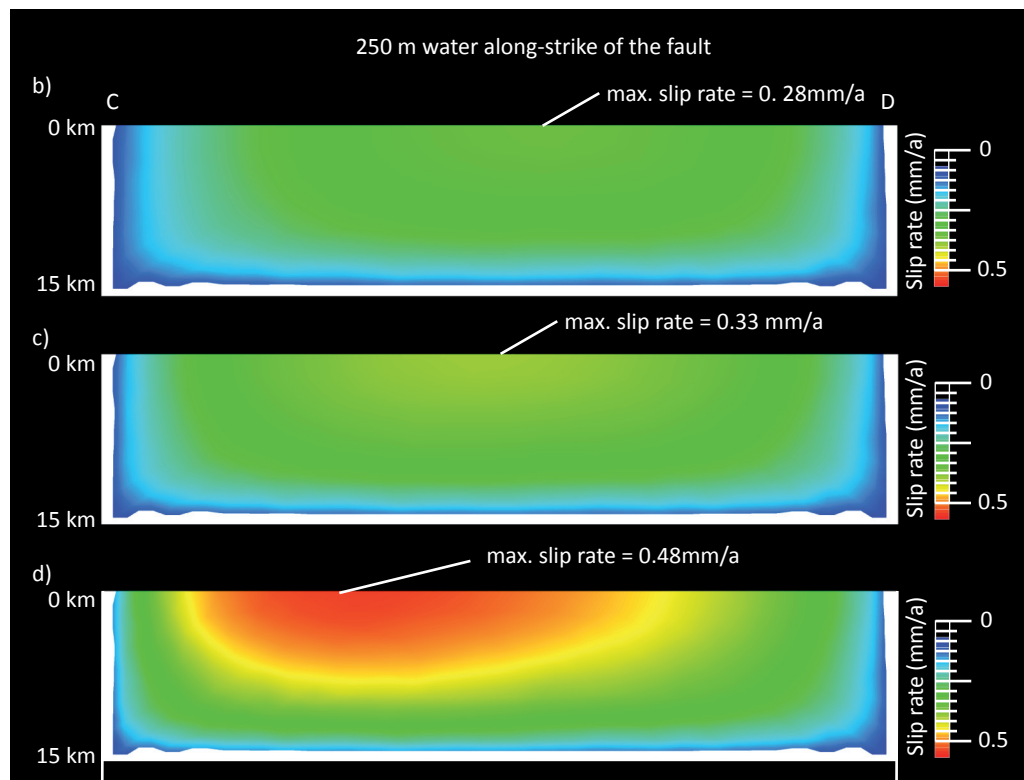
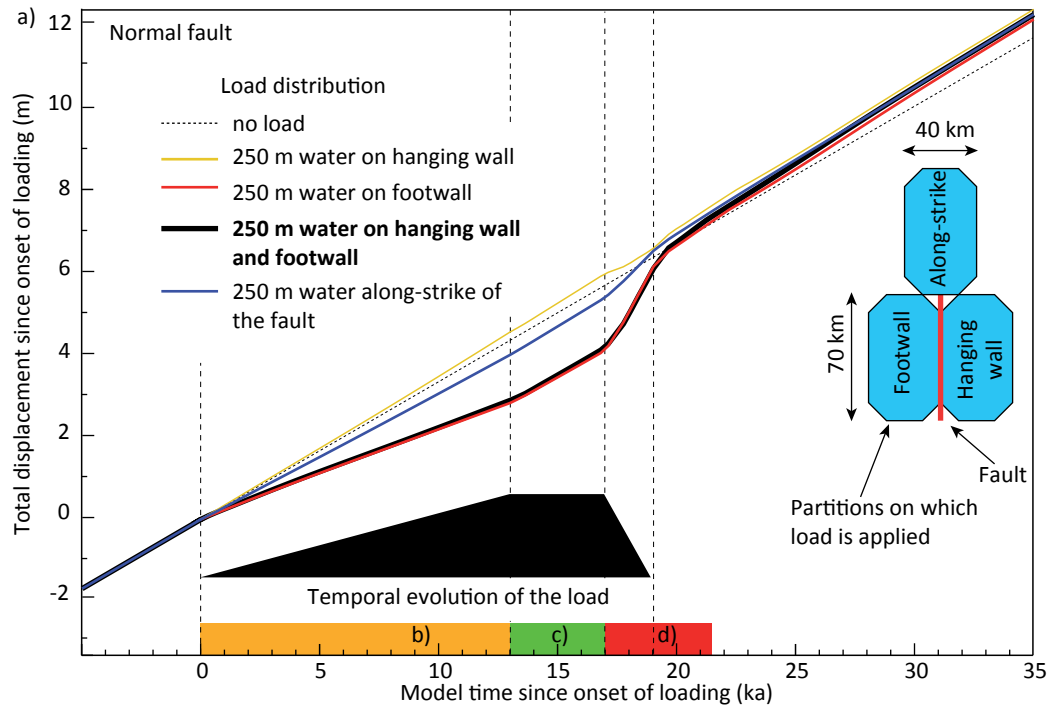


**Fig. 24:** Slip history plot of the normal fault experiments with varying distribution of a 250-m-deep lake. The location of the surface partitions to which the load is applied is sketched by the blue octagons. The temporal evolution of the load is indicated by the black polygon inset. The slip history of the reference model is indicated by the thick black curve. b) - d) Slip rate distribution on the hanging wall for loading, phase of constant load and unloading of 250 m of water along-strike of the fault. The intervals are indicated in a) by colored bars. Note the asymmetric slip rate distribution in c) and d). The location of the profile is shown in Figure 5.

the fault. With 2000 m of ice loaded on the hanging wall, the fault begins to slip 1.6 ka after the onset of deglaciation, 1.1 ka later than the thrust fault in the reference model. The fault reaches an accelerated slip rate of up to 16 mm/a. In contrast, nearly no effect can be seen for the experiments with 500 m of ice on the footwall and along-strike of the fault. In case of the 500-m-thick ice load on the footwall, the slip rate on the fault stays nearly unaffected during glaciation and keeps on slipping at a rate close to the steady-state slip rate. With onset of deglaciation the slip rate of the thrust fault decelerates slightly until the end of the deglaciation phase. This interval of decreased slip rate is followed by 1 ka of slightly increased slip on the fault until at about 20 ka model time the steady-state slip rate is resumed. A 2000-m-thick load on the footwall additionally leads to slight acceleration of the slip rate during glaciation. The glacial load of 500 m of ice applied along-strike of the fault leads to a slightly decelerated slip rate during glaciation and a slightly accelerated slip rate during deglaciation (Fig. 23a) concerning. Regarding the model in which 2000 m of ice are applied along-strike of the fault, the timing of the changes in the slip rate is similar to the experiment with 500 m of ice along-strike of the fault, but the slip rate decrease during glaciation is higher and the magnitude of the accelerated slip rate during deglaciation increases (Fig. 23b). The contour plot in Figure 23c, showing the slip history of the fault for the experiment with 2000 m of ice loaded along-strike of the fault, reveals an asymmetric slip rate distribution during the glacial-interglacial cycle. During glaciation, the area of maximum slip on the fault shifts away from the center of the fault and away from the location of the ice load and the area of maximum subsidence (Fig. 23c), reaching a peak value of 0.33 mm/a. This picture changes after the onset of deglaciation. Now the area of maximum slip rate shifts in the opposite direction crossing the center of the fault, moving towards the location of the former ice load and the area of maximum isostatic rebound, reaching a peak value of 0.56 mm/a (Fig. 23d).

Regarding the experiments made for the normal fault model, the spatial variation of the surface load leads to diverging results. The timing of changes in the slip rate caused by a 250 m deep lake on the footwall and along-strike of the fault is similar to the timing of slip rate changes in the reference model. This means: deceleration of the slip rate during lake level rise and acceleration of the slip rate during lake regression. The slip history of the fault for a 250 m deep lake on the hanging wall is different (Fig. 24a). Loading the hanging wall of the fault with a load representing 250 m of water, leads to an increased slip rate. The phase of lake highstand is characterized by a slip rate close to the steady-state slip rate. With the onset of lake regression, fault slip decreases and the fault nearly ceases to slip. After the removal of the lake, the fault again experiences a 1 ka interval of accelerated slip before fault activity returns to the steady-state slip rate close to 0.33 m/a. Such an asymmetric loading of the model, by locating a lake along-strike of the normal fault, leads again to an asymmetric distribution of slip on the fault plane (Fig. 24b-d) as seen before in the experiments made for the thrust fault model. As a consequence, the point of maximum slip shifts towards the tip of the fault located opposite to the lake (Fig. 20b). During lake highstand, the slip rate shows a distribution similar to the symmetrically loaded reference model with load on the hanging wall and footwall simultaneously. The point of maximum slip is located in the center of

the fault and the fault slips at the steady-state rate of 0.33 mm/a (Fig. 24c). The regression of the asymmetric lake load leads to increased slip on the fault. In this phase the point of maximum slip rate shifts towards the tip of the fault close to the location of the former lake, reaching a maximum slip rate of 0.48 mm/a (Fig. 24d).

To investigate the effect of spatial distribution of the load on the slip rate behavior of the strike-slip faults, two experiments have been made, varying the location of a 250- m-deep lake relative to the faults without changing the size and shape of the load. In the first experiment the long axis of the load is orientated perpendicular to the strike of the faults, giving a short but wide lake (Fig. 25). Such a load leads to an increased slip rate during unloading of 4.37 mm/a for P1 and 3.74 m/a for P2. Both values are lower than the accelerated slip rates of the reference model. In the second

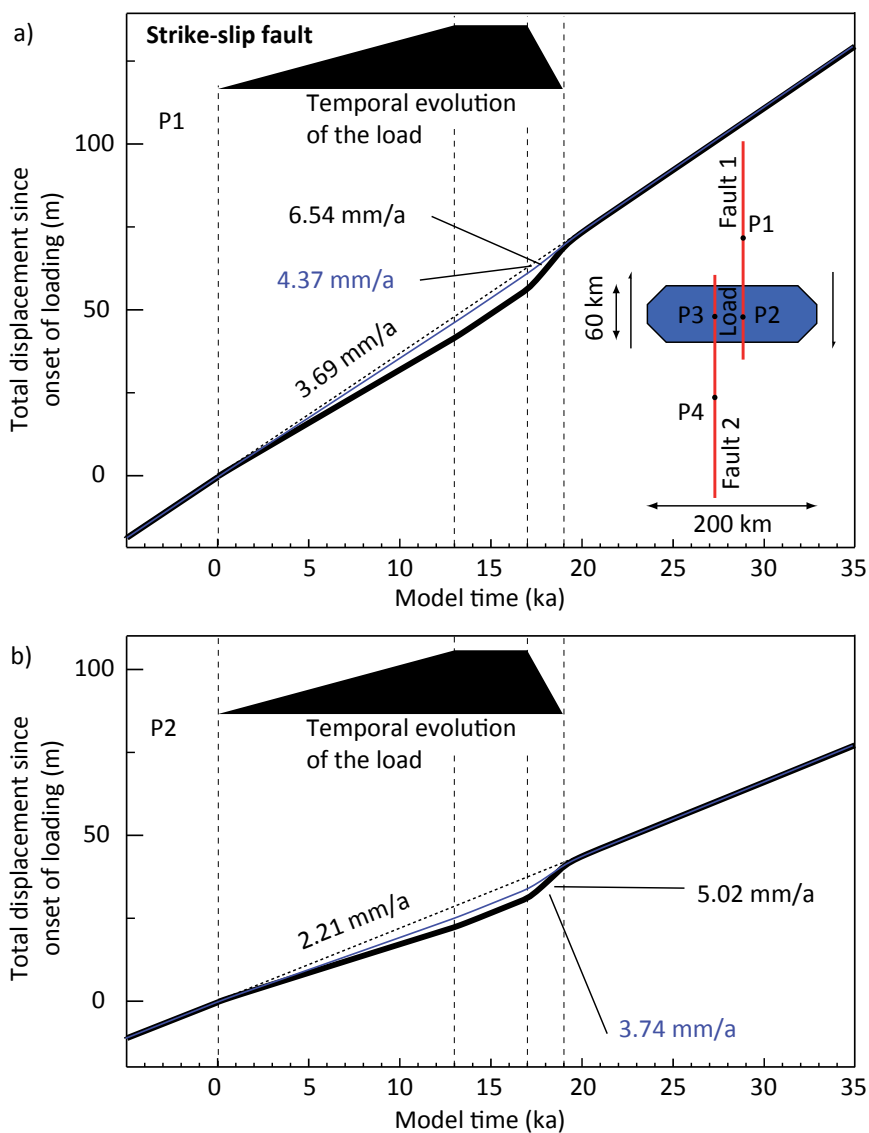


**Fig. 25:** Slip history plot of the strike-slip fault experiments with varying distribution of a 250-m-deep lake. The location of the surface partition, to which the load, is applied is marked by the blue octagon. The temporal evolution of the load is indicated by the black polygon inset. The slip history of the reference model is indicated by the thick black curve. a) shows the slip evolution at P1, and b) at P2.



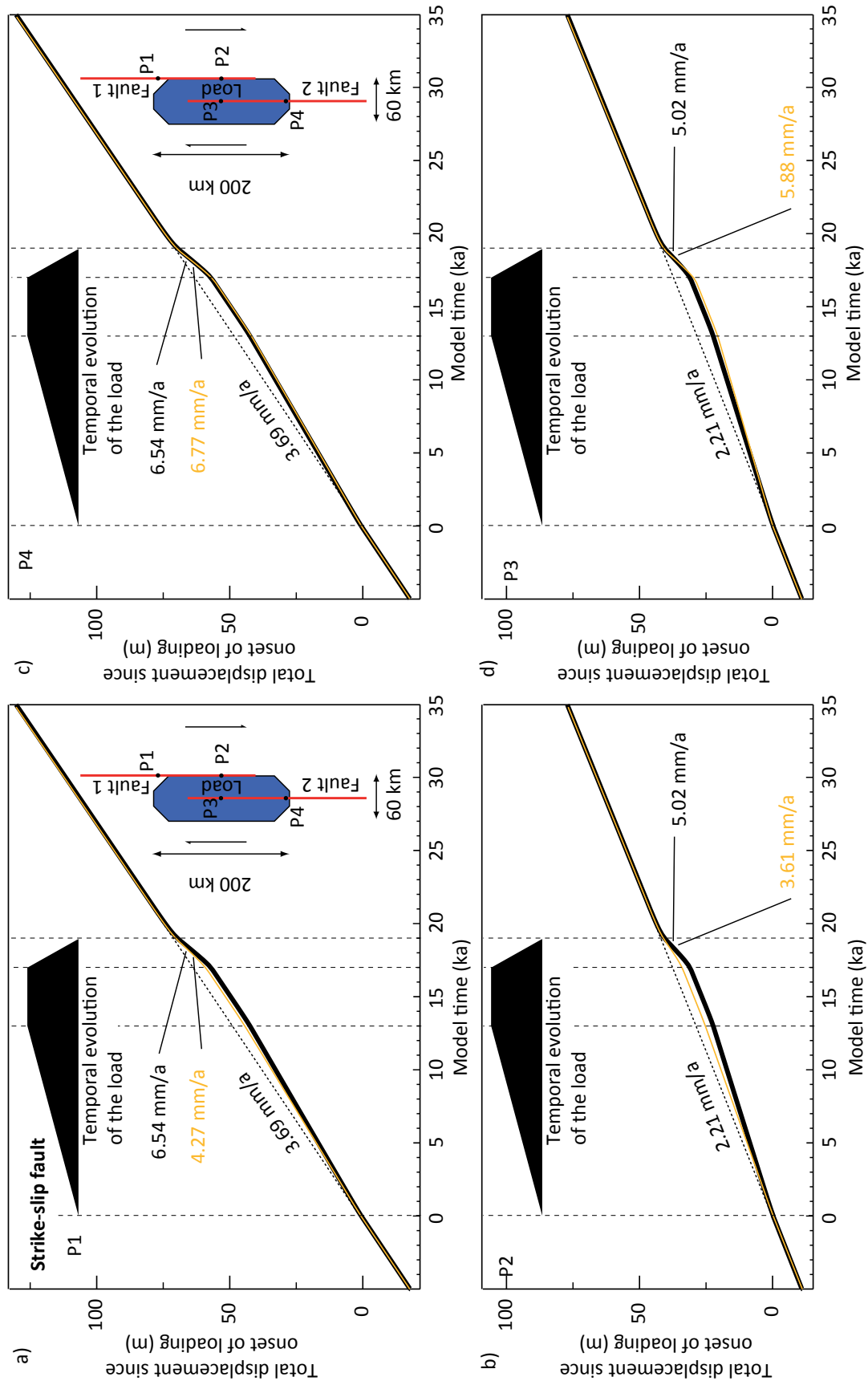


**Fig. 26:** Slip history plot of the strike-slip fault experiments with varying distribution of a 250-m-deep lake. The location of the surface partition, to which the load is applied, is marked by the blue octagon. The temporal evolution of the load is indicated by the black polygon inset. The slip history of the reference model is indicated by the thick black curve. a) shows the slip evolution at P1, b) at P2, c) at P3, and d) at P4.

set of experiments, the long axis of the lake is orientated parallel to the fault strike, centered over fault 2 (Fig. 26). This gives an asymmetric load on top of the fault system. In the reference model and in the previous experiment, the geometry and location of the faults in the model was point symmetric around the center of the lake in the center of the model, leading to similar slip rates at P1 and P4 as well as at P2 and P3. In this experiment the asymmetric load leads to differing slip rates at P1 and P4 and at P2 and P3. Unloading the surface of the model leads to accelerated slip rates of 4.27 mm/a at P1 and 3.61 mm/a at P2 on the fault at the border of the load. Both slip rates are lower than the ones measured in the reference model with 6.54 mm/a at P1 and 5.02 mm/a at P2. Regarding the fault symmetrically covered by the lake, the accelerated slip rates during unloading are 6.77 mm/a at P3 and 5.88 mm/a at P4, both higher than in the reference model.

### 3.2.3 Influence of the duration of unloading on the slip rate variations

In this set of experiments, the 35-ka-lasting loading function has been modified to test the influence of the duration of unloading on the slip rate variation of the thrust fault and the normal fault. The duration of the interval of unloading in the loading function of the reference model is 2 ka. This time has been expanded to 4 ka and 8 ka of unloading in this set of experiments. While slip on the fault in the thrust fault reference model starts at 0.5 ka after the onset of deglaciation, it takes 1 ka and ~ 1.8 ka for the fault to slip again if deglaciation lasts for 4 ka and 8 ka respectively (Fig. 27). The total value of the accelerated slip rate of the thrust fault decreases with

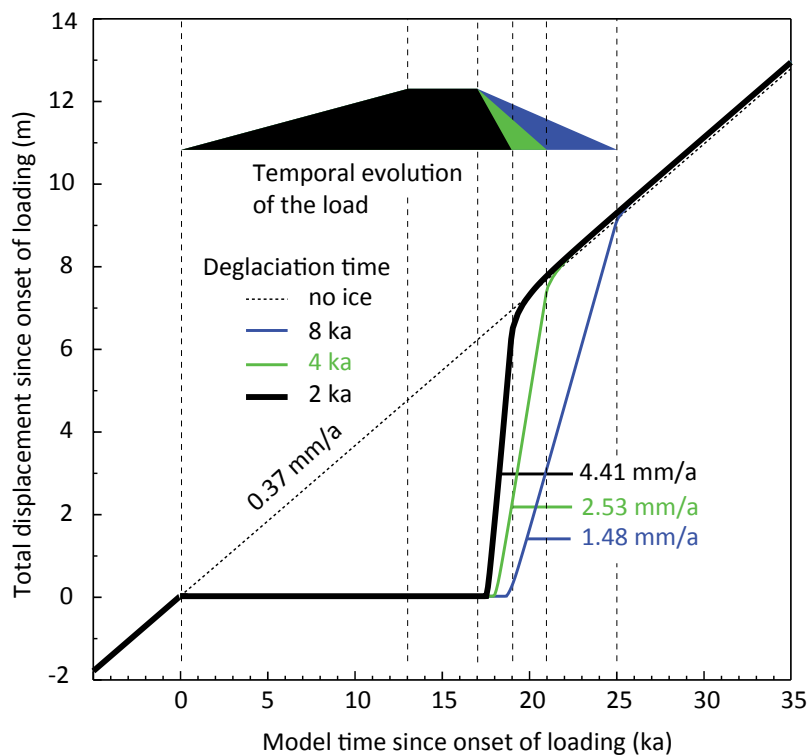


**Fig. 27:** Slip history plot of the thrust fault experiments with varying deglaciation times. The temporal evolution of the load is indicated by the black polygon inset. The slip history of the reference model is indicated by the thick black curve.

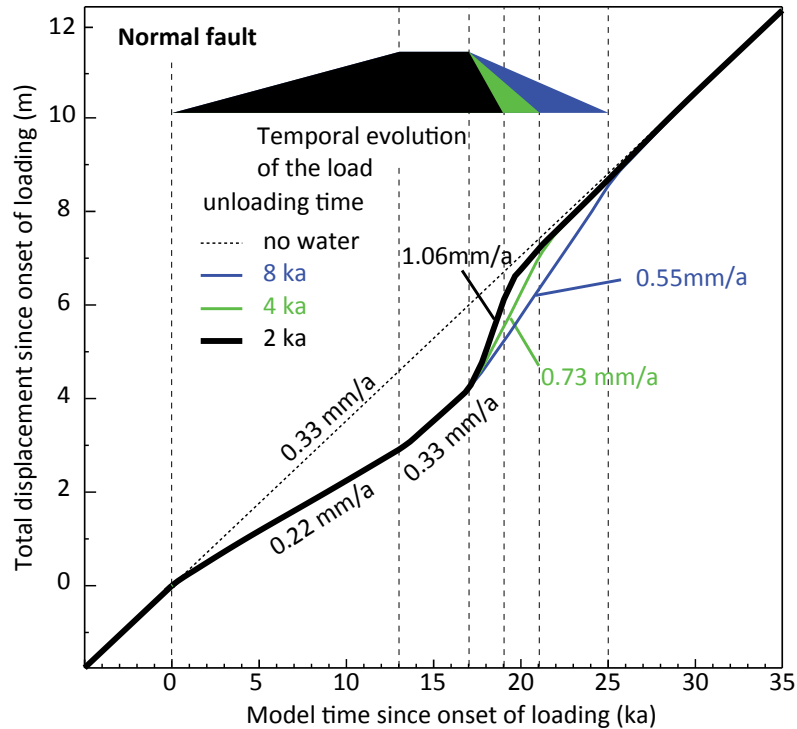


**Fig. 28:** Slip history plot of the normal fault experiments with varying unloading times. The temporal evolution of the load is indicated by the black polygon inset. The slip history of the reference model is indicated by the thick black curve.

longer unloading intervals. The maximum slip rate of the fault during deglaciation over a period of 4 ka is 2.53 mm/a. This slip rate is lower than in the reference model where accelerated slip during unloading reaches a value of 4.41 mm/a. Unloading over a time span of 8 ka leads to an accelerated slip rate of 1.48 mm/a. The same experiments have been made for the normal fault model. Here the timing of the initiation of accelerated slip on the fault during lake regression stays unaffected (Fig. 28). While the accelerated slip of the fault in the normal fault reference model reaches 1.06 mm/a during 2 ka of unloading, 4 ka of unloading lead to a slip rate of 0.73 mm/a and 8 ka of unloading to 0.55 mm/a.

### 3.2.4 Influence of the rheology on the slip rate variations

In this series of experiments three sets with different rheological settings have been tested for the thrust fault, the normal fault and the strike-slip fault models. The first set experiments have been made concerning the thrust fault model. First the viscosity of the lower crust is either set to  $\eta_{\text{lower c.}} = 1 \times 10^{21}$  Pa s or to  $\eta_{\text{lower c.}} = 1 \times 10^{19}$  Pa s and is compared to the reference model with a lower crust viscosity of  $1 \times 10^{20}$  Pa s. The viscosity of the lower crust is always kept lower than the viscosity of the lithospheric mantle as suggested for compressional tectonic regimes (e.g. Burov and Watts, 2006). In both experiments deglaciation causes a pronounced increase in the fault slip rate (Fig. 29). The temporal evolution of the slip rate of the two experiments and the reference model is similar until the beginning of deglaciation. While in the experiment with the stronger lower crust with a viscosity of  $1 \times 10^{21}$  Pa s the phase of accelerated slip lasts for 10 ka,

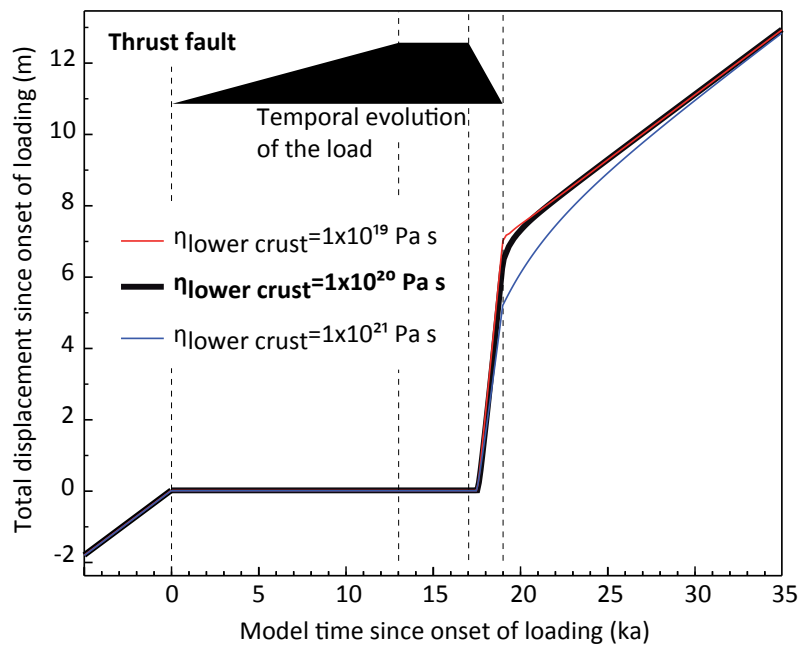


**Fig. 29:** Slip history plot of the thrust fault experiments with varying viscosity of the lower crust and the lithospheric mantle. The temporal evolution of the load is indicated by the black polygon inset. The slip history of the reference model is indicated by the thick black curve.

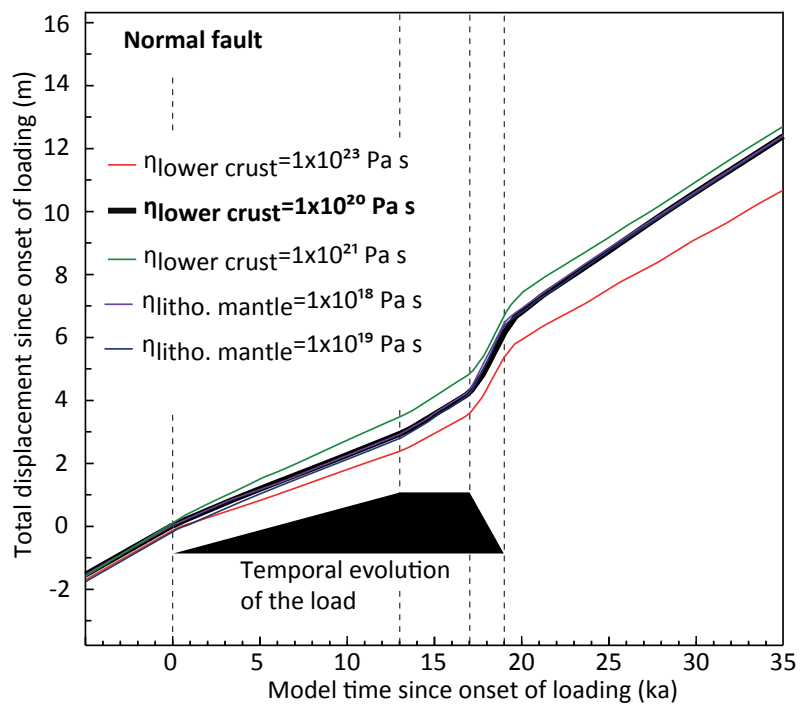


**Fig. 30:** Slip history plot of the normal fault experiments with varying viscosity of the lower crust and the lithospheric mantle. The temporal evolution of the load is indicated by the black polygon inset. The slip history of the reference model is indicated by the thick black curve.

in the experiment for a weak lower crust with a viscosity of  $1 \times 10^{19}$  Pa s the phase of accelerated slip ends with the end of unloading.

For the normal fault, different rheological settings reflecting the spectrum of viscosity profiles through the lithosphere, as proposed for the extensional regimes (Nakiboglu and Lambeck, 1983; Bills and May, 1987; Bills et al., 1994; Bills et al., 2007, Kaufmann and Amelung, 2000) have been tested. Similar to the reference model the four experiments use a rheological setup that reflects a decreasing lithospheric viscosity with depth. The slip history of all four experiments resembles the one of the normal fault reference model, with respect to the timing and magnitude of the slip rate variations (Fig. 30). The steady-state slip rate of the models prior to loading differs, depending on the lower crust viscosity. A lower crust with a viscosity of  $1 \times 10^{23}$  Pa s leads to a lower steady-state slip rate than the one tested with  $\eta_{\text{lower c.}} = 1 \times 10^{21}$  Pa s. In the experiments using a lithospheric mantle viscosity of  $1 \times 10^{19}$  Pa s and lower, the phase of accelerated slip ends with the end of the load removal. The slip history of the experiments with a lithospheric mantle viscosity of  $1 \times 10^{20}$  Pa s shows a phase of accelerated slip that lasts for 4 ka, resulting in 2 ka of accelerated slip after the total removal of the load.

The last set of experiments was calculated for the strike-slip fault model. The rheological settings reflect the spectrum of viscosity profiles through the lithosphere as proposed for strike-slip regimes (Al-Zoubi and ten Brink, 2002). As a consequence of the simplified model setup, the experiments

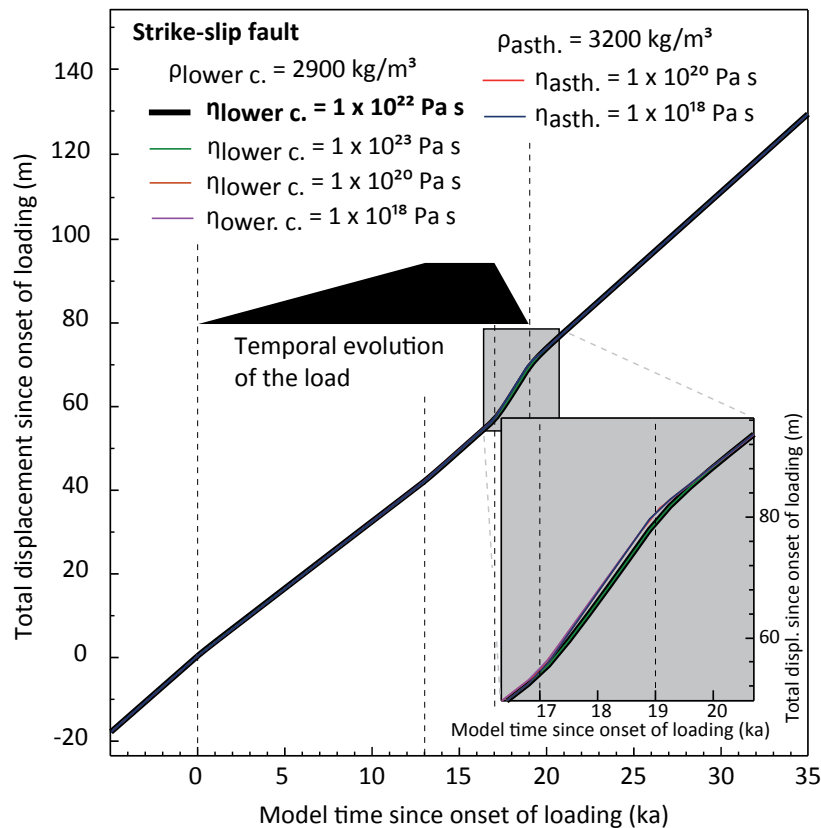


**Fig. 31:** Slip history plot of the strike-slip fault experiments with varying rheology. The temporal evolution of the load is indicated by the black polygon inset. The slip history of the reference model is indicated by the thick black curve.

calculated include whether a visco-elastic lower crust or a visco-elastic asthenosphere, both simulated by the springs and dashpot elements at the bottom of the model. The slip history of all four experiments resembles the one of the normal fault reference model, concerning timing and magnitude of the slip rate (Fig. 31). In the experiments in which the springs and dashpots simulate a lower crust with a density of  $\rho_{\text{lower c.}} = 2900 \text{ kg/m}^3$ , the accelerated slip during unloading starts later than in the experiments in which the springs and dashpot elements simulate the asthenosphere with a density of  $\rho_{\text{asth.}} = 3200 \text{ kg/m}^3$ . The experiments simulating a lower crust, have a 0.8 ka-lasting phase of accelerated slip after the end of unloading while in the models where an asthenosphere is simulated, this phase only lasts for 0.2 ka.

### 3.2.5 Influence of the shortening rate, the extension rate, the lateral shear velocity, and the fault dip on the slip rate variations

By varying the velocity of the boundary condition in all three models, the influence of the shortening rate on the slip behavior of the thrust fault, the extension rate on the slip behavior of the normal fault model, and the rate of lateral shear velocity on the slip behavior of the strike-slip fault during a loading and unloading cycle has been examined. In these experiments, rates for the velocity boundary condition of 4 mm/a and 8 mm/a have been tested and compared to the results of the reference models using a velocity boundary condition of 6 mm/a. The experiments made for the thrust fault reference model show a nearly similar timing of the slip rate changes during glaciation and deglaciation. An increasing shortening rate leads to a higher steady-state slip rate and to a shorter phase of ceased slip on the fault during glaciation and maximum ice load (Fig. 32). The accumulated slip during the phase of accelerated slip increases with a higher shortening rate. In case of the experiments made for the normal fault model, the results show exactly the same timing of the slip rate changes during lake level rise and lake regression (Fig. 33). A higher extension rate leads to a higher steady-state slip rate. In the phase of lake level rise, faulting decreases but the higher the extension rate, the higher the decelerated slip rate. During loading, the normal fault of the reference model slips at a rate of 0.22 mm/a. In the experiment with 8 mm/a extension rate, the fault slips at 0.29 mm/a while the experiment with an extension rate of 4 mm/a leads to a decelerated slip rate of 0.08 mm/a. Regarding the phase of lake regression, the slip rate of the reference model between 17 ka and 19 ka slips with 1.06 mm/a (Fig. 33). An extension rate of 4 mm/a leads to an increased slip rate of 0.98 mm/a and to 2.1 m of accumulated slip during unloading. An extension rate of 8 mm/a leads to an increased slip rate of 1.2 mm/a by which the fault accumulates 2.8 m of slip.

In this set of experiments the shear velocity of the strike-slip fault model is varied. As

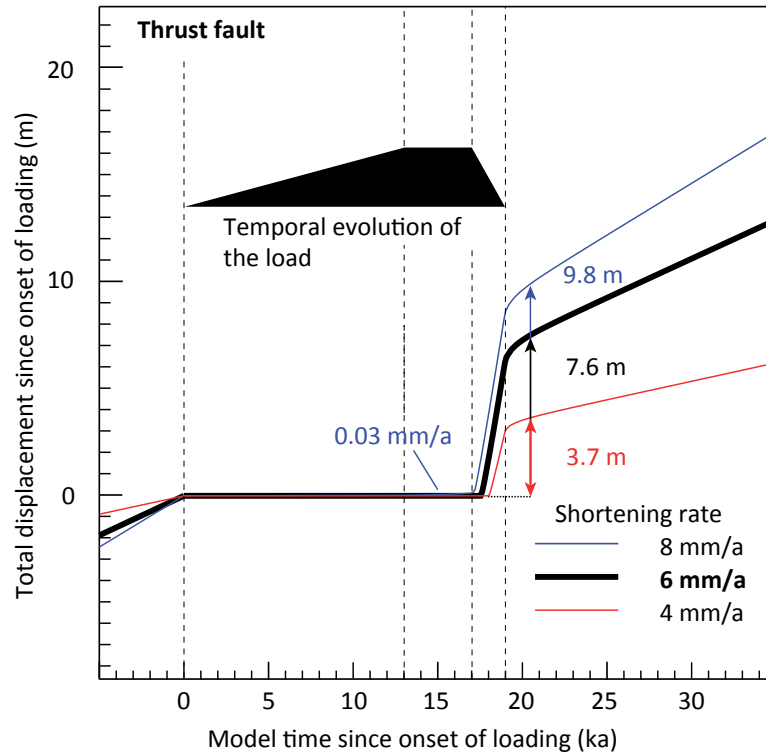


Fig. 32: Slip history plots of the thrust fault experiments with variable shortening rate. The temporal evolution of the load is indicated by the black polygon inset. The slip history of the reference model is indicated by the thick black curve.

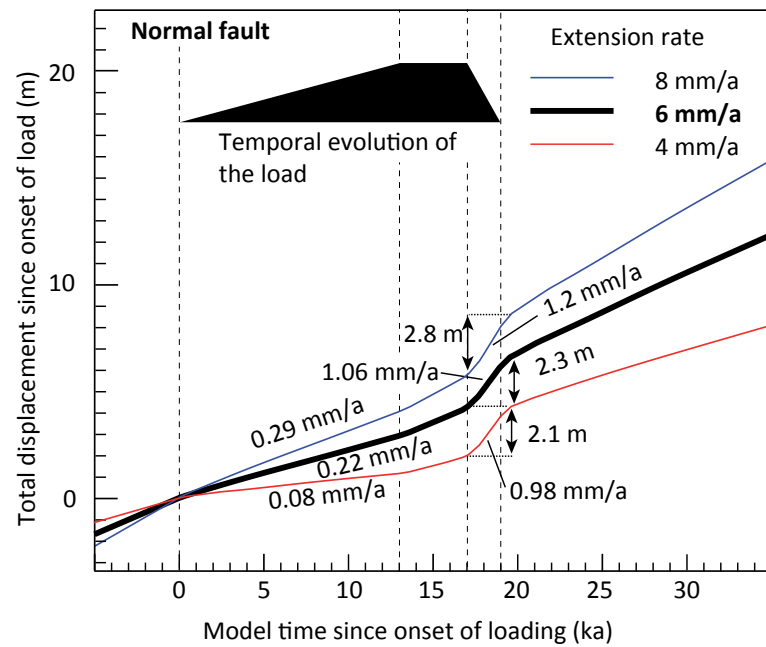
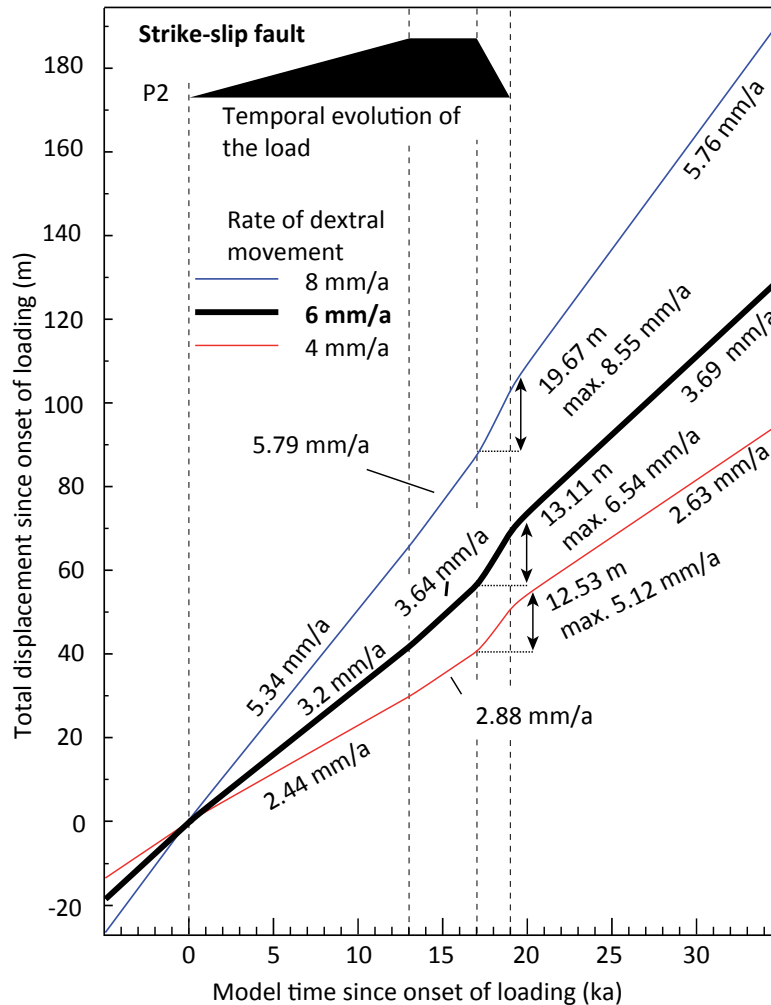


Fig. 33: Slip history plots of the normal fault experiments with variable extension rate. The temporal evolution of the load is indicated by the black polygon inset. The slip history of the reference model is indicated by the thick black curve.

in the normal fault experiments before, all experiments show exactly the same timing of the slip rate changes during lake level rise and lake regression as in the reference model (Fig. 34). Lateral shearing at higher rates leads to a higher steady-state slip rate. In the phase of lake level rise, the slip rate decreases. To investigate the slip rate changes, only the slip rate at point P1 is considered. During loading, the fault of the reference model slips at a rate of 3.2 mm/a. In the experiment with 8 mm/a lateral shearing velocity, the fault slips at 5.34 mm/a while in the experiment with 4 mm/a,



**Fig. 34:** Slip history plots of the strike-slip fault experiments with variable rate of dextral motion. The temporal evolution of the load is indicated by the black polygon inset. The slip history of the reference model is indicated by the thick black curve.

loading leads to a decelerated slip rate of 2.44 mm/a. Regarding the phase of lake regression, the slip rate acceleration increases with a higher lateral shear velocity. During unloading, the fault of the reference model slips at a rate of 13.11 mm/a. In the experiment with 8 mm/a of lateral shear velocity, the fault slips at 19.67 mm/a while in the experiment with 4 mm/a, loading leads to a decelerated slip rate of 12.53 mm/a.

In addition, the thrust and normal fault model have been tested using different angles of fault dip. A variation of the fault dip to  $60^\circ$  in case of the thrust fault model, leads to a lower steady-



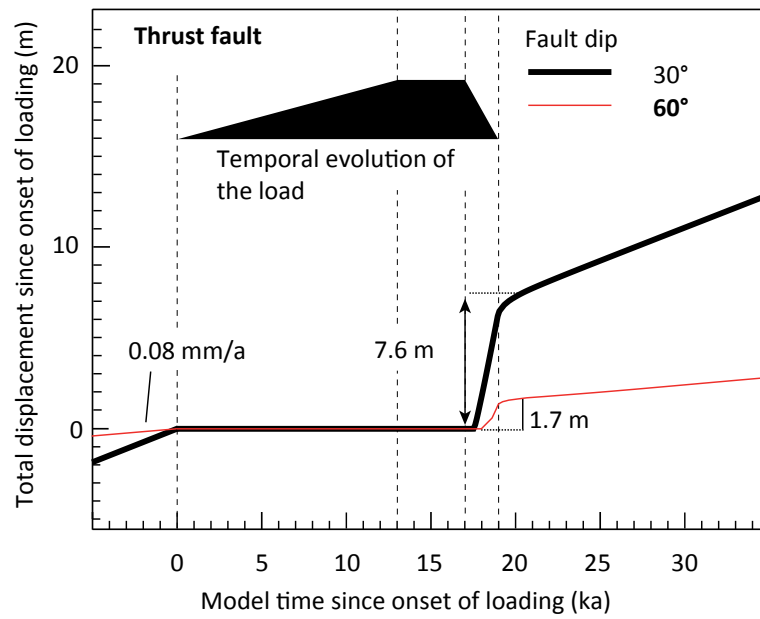


**Fig. 35:** Slip history plots of the thrust fault experiments with variable fault dip. The temporal evolution of the load is indicated by the black polygon inset. The slip history of the reference model is indicated by the thick black curve.

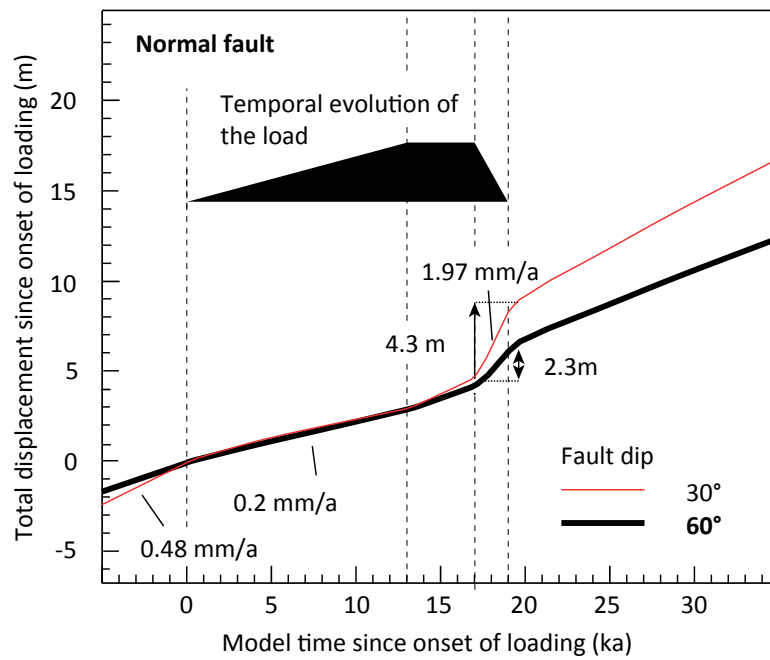


**Fig. 36:** Slip history plots of the normal fault experiments with variable fault dip. The temporal evolution of the load is indicated by the black polygon inset. The slip history of the reference model is indicated by the thick black curve.

state slip rate of 0.03 mm/a. Loading ceases faulting until 1.2 ka after onset of unloading. After 1.7 ka of accelerated slip, the 60°-dipping-thrust-fault returns to the steady-state slip rate (Fig. 35). The accumulated slip during the interval of accelerated slip rate is 1.7 m. A fault dip of 30° in case of the normal fault model leads to a higher steady-state slip rate of 0.48 mm/a on the fault. While loading, the 30° normal fault slips at a rate of 0.2 mm/a and accelerates to 1.97 mm/a with the onset of unloading. During the phase of unloading, the fault accumulates 4.3 m of slip (Fig. 36).

## 4 Discussion

### 4.1 Discussion of the results

The results of the numerical experiments show, that glacial loading and postglacial unloading as well as lake level fluctuations strongly affect the slip behavior of thrust, normal, and strike-slip faults. A higher slip rate means more displacement in a certain time interval and vice versa. This phenomenon corresponds to an increase in seismicity in nature. Similarly a low slip rate corresponds to less displacement and a decrease in seismicity.

The major response of a fault to changes in the surface load can be summarized by a decelerated slip rate due to an increasing load and an accelerated slip rate due to a decreasing load. This basic pattern is valid for nearly all experiments. The amplitude of the slip rate decrease during loading and the increase during unloading highly depends on the magnitude of the applied load as seen in the experiments made for a varying load thickness. For all three fault types, a larger load leads to lower slip rates during loading and to higher slip rates during unloading. In case of the thrust fault, glacial loading of 500 m of ice and more leads to stagnation of slip until the onset of unloading. On the other hand, ice thicknesses of less than 250 m lead to decelerated slip during loading and a return to the steady-state slip rate during the interval of constant load. This behavior shows, that the magnitude of the load also affects the timing of slip rate changes. A spatial variation of the load affects the amplitude of the slip rate decrease during loading and the increase during unloading. It also affects the timing of the changes in the slip rate and the distribution of slip along the fault plane. Changing the timing of the loading function directly affects the timing of the slip rate variation as the slip rate changes of the normal and strike-slip models are almost in phase with the temporal evolution of the loading function. In case of the thrust fault, the response of the slip rate to changes in the loading history can be delayed by up to 2 ka depending the duration on the unloading interval.

The rheology of the lithosphere plays a minor role for the fault slip behavior. In the normal and strike-slip fault experiments, neither the timing of the slip history nor the amplitude of the slip rate changes are significantly affected according to the results of the parameter study. The influence of changes in the rheology on the slip behavior of thrust faults becomes obvious by the time lag the fault needs to return to the pre-loading slip rate after the end of unloading. The rheologies used in the parameter study represent a weak lower crust in combination with a strong lithospheric mantle in the thrust fault experiments and a strong lower crust overlying a weak lithospheric mantle in the normal fault experiments. In addition to these experiments, one thrust fault experiment has been calculated using the rheology of the normal fault reference model and vice versa, although such rheologies are not in agreement with the tectonic stress regime (Brace and Kohlstedt, 1980; Chen and Molnar, 1983; Burov and Watts, 2006; Nakiboglu and Lambeck, 1983; Bills and May, 1987; Bills et al., 1994). The results of these experiments show a slip

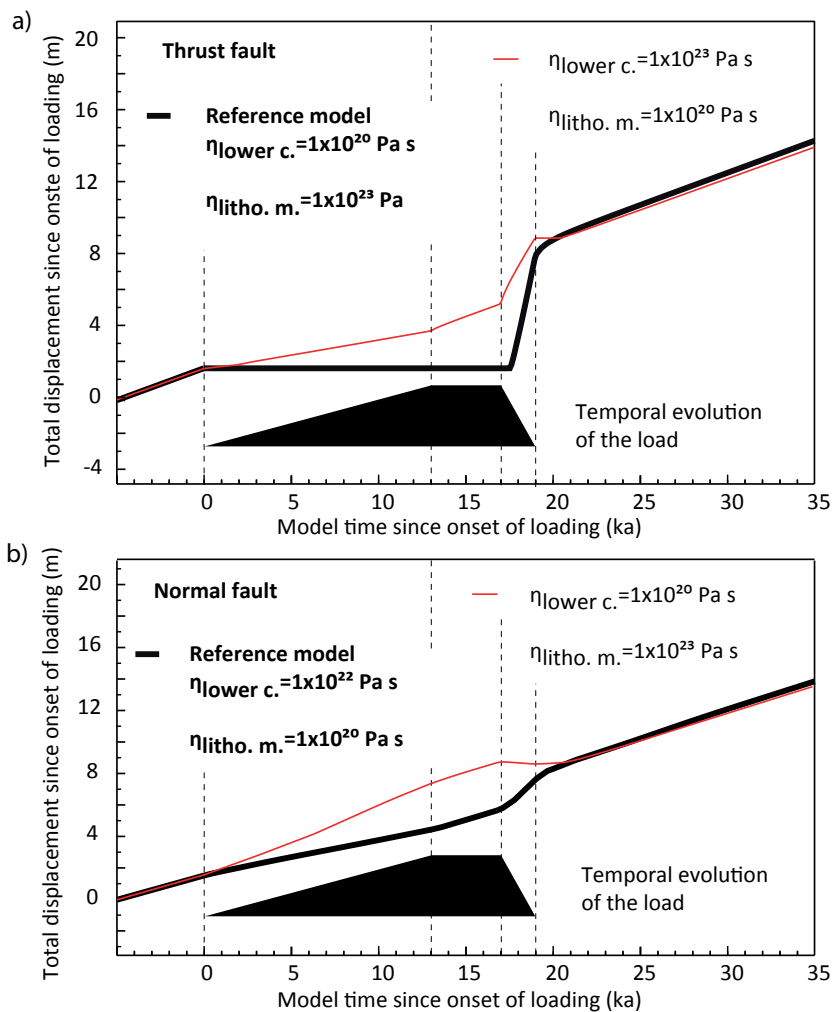


**Fig. 37:** Slip history of a) the thrust fault experiment with a strong lower crust viscosity of  $\eta_{\text{lower c.}} = 1 \times 10^{23} \text{ Pa s}$ , a weak lithospheric mantle viscosity of  $\eta_{\text{litho. m.}} = 1 \times 10^{20} \text{ Pa s}$ , and a viscosity of the asthenosphere of  $\eta_{\text{asth.}} = 1 \times 10^{19} \text{ Pa s}$  and b) the normal fault experiment with a weak lower crust viscosity of  $\eta_{\text{lower c.}} = 1 \times 10^{20} \text{ Pa s}$ , a strong lithospheric mantle viscosity of  $\eta_{\text{litho. m.}} = 1 \times 10^{23} \text{ Pa s}$ , and a viscosity of the asthenosphere of  $\eta_{\text{asth.}} = 1 \times 10^{19} \text{ Pa s}$ .

behavior that is inconsistent with the previous experiments. The behavior of the thrust fault in the model with a lower crust viscosity of  $\eta_{\text{lower c.}} = 1 \times 10^{23} \text{ Pa s}$  and a lithospheric mantle viscosity of  $\eta_{\text{litho. m.}} = 1 \times 10^{20} \text{ Pa s}$  (Fig. 37) mainly affects the timing of the slip rate changes caused by glacial loading and postglacial unloading. In this experiment, slip on the fault does not cease as it does in the reference model. Loading leads to a decelerated slip rate. Furthermore, the slip rate returns to steady-state during the phase of constant load. In the experiment performed with the normal fault, using a lower crust viscosity of  $\eta_{\text{lower c.}} = 1 \times 10^{20} \text{ Pa s}$  in combination with a lithospheric mantle viscosity of  $\eta_{\text{litho. m.}} = 1 \times 10^{23} \text{ Pa s}$ , the slip history of the normal fault strongly deviates from all previous experiments (Fig. 37). Loading leads to an accelerated slip rate followed by a return to the steady-state slip rate during the phase of constant load and a decelerated slip rate during unloading, with a switch to reverse faulting. With the end of unloading, the fault returns to normal faulting at the steady-state slip rate.

The change of the velocity of the extension or shortening rate and the dip of the fault only

changes the average slip accumulated over time and thus affects the amplitude of the changes in the slip rate over time. After summarizing the influence of all parameters on the slip rate evolution of all three fault types, the pattern of decelerated slip during loading and accelerated slip during unloading does not seem to fit to all experiments made. The results of the parameter study pose the question of the mechanism causing these changes in the slip rates of faults during glacial loading and postglacial unloading.

## 4.2 Cause of the slip rate variations

The changes in the slip behavior of the faults are caused by changes in the crustal stress field around the fault. An increase in the maximum principal stress  $\sigma_1$  without changing the minimum principal stress  $\sigma_3$  leads to an increase of the differential stress  $\sigma_1 - \sigma_3$  promoting slip on the fault, while a decreasing  $\sigma_1$  leads to a decrease of  $\sigma_1 - \sigma_3$ , preventing slip on the fault. On the other hand, an increase in  $\sigma_3$  without changing  $\sigma_1$  leads to a decrease of  $\sigma_1 - \sigma_3$  and vice versa. The slip behavior of the thrust, the normal, and the strike-slip fault reference model is controlled by the Mohr Coulomb failure criterion. Changes observed in the slip behavior of each model fault are caused by transient changes in the crustal stress field related to the growth and shrinkage of the surface load (Hampel and Hetzel, 2006; Turpeinen et al., 2008). This mechanism will be examined in the following. The evolution of  $\sigma_1$ ,  $\sigma_3$  and  $\sigma_1 - \sigma_3$  during glacial loading and postglacial unloading of all three reference models is shown in Figures 38 to 40. Loading the model lithosphere leads to an increase of  $\sigma_1$  and  $\sigma_3$ . This picture is consistent for all three reference models (Figs. 38 - 40). The principal stresses are measured at a point near the center of the fault in a depth of 7.5 km in the hanging wall. In case of the strike-slip fault reference model, this point is located in a depth of 10 km, close to P2 (inlet in Fig. 15).

The principal stress evolution of the thrust fault reference model shows an increase in  $\sigma_1$  of 5 MPa and in  $\sigma_3$  of 3.5 MPa during glaciation (Fig. 38). During the phase of constant load, the increase in  $\sigma_3$  stops, while the increase in  $\sigma_1$  is still ongoing until the onset of unloading. The glacial ice applied to the surface of the lithosphere, leads to flexure and downward motion of the surface in the center of the load. After loading the lithosphere, the load is kept constant but the downward motion of the lithosphere in the center of the load continues, sinking at a lower rate of subsidence. In phase with the subsidence in the center of the load, the maximum principal stress increases due to additional crustal shortening caused by the flexure of the lithosphere as shown in Figure 10. With the beginning of deglaciation,  $\sigma_3$  linearly decreases between 17 ka and 19 ka, returning to the steady-state stress field with the completion of deglaciation. Looking at the evolution of  $\sigma_1$  in the thrust fault model during deglaciation, a clear decrease is visible, but in contrast to the evolution of  $\sigma_3$ , this decrease is marked by two different angles in slope. During the

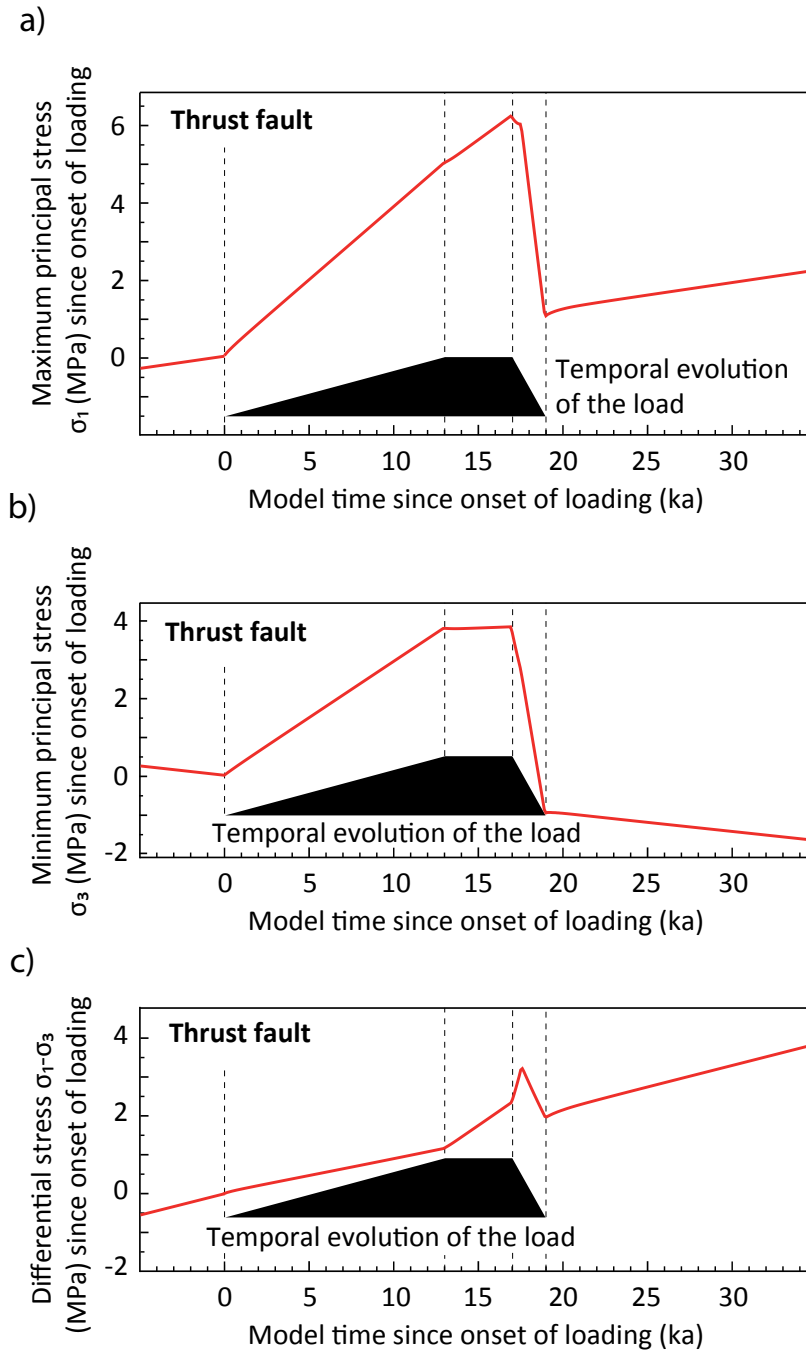


**Fig. 38:** Temporal evolution, relative to the onset of loading, of the a) maximum principal stress  $\sigma_1$ , b) minimum principal stress  $\sigma_3$ , and c) differential stress  $\sigma_1 - \sigma_3$  in the thrust fault reference model measured in the center of the hanging wall in 7.5 km depth. The black inset represents the temporal evolution of the load.

first 0.5 ka of unloading,  $\sigma_1$  decreases much slower than in the following 1.5 ka. This change in slope angle of the stress drop falls together with the reactivation of slip on the fault (Fig. 38). At 0.5 ka after the onset of deglaciation, the local crustal shortening, induced by the flexure of the lithosphere is rapidly compensated by slip on the thrust fault (Fig. 7, Fig. 10). This leads to a pronounced decrease of  $\sigma_1$  and in consequence to a decrease of  $\sigma_1 - \sigma_3$  until 19 ka of model time (Fig. 38). The evolution of  $\sigma_1 - \sigma_3$  shows a slight decrease during glaciation, followed by an increase during the phase of maximum ice load. During the first 0.5 ka of deglaciation,  $\sigma_1 - \sigma_3$  drastically increases and then drops towards steady-state at the end of deglaciation.

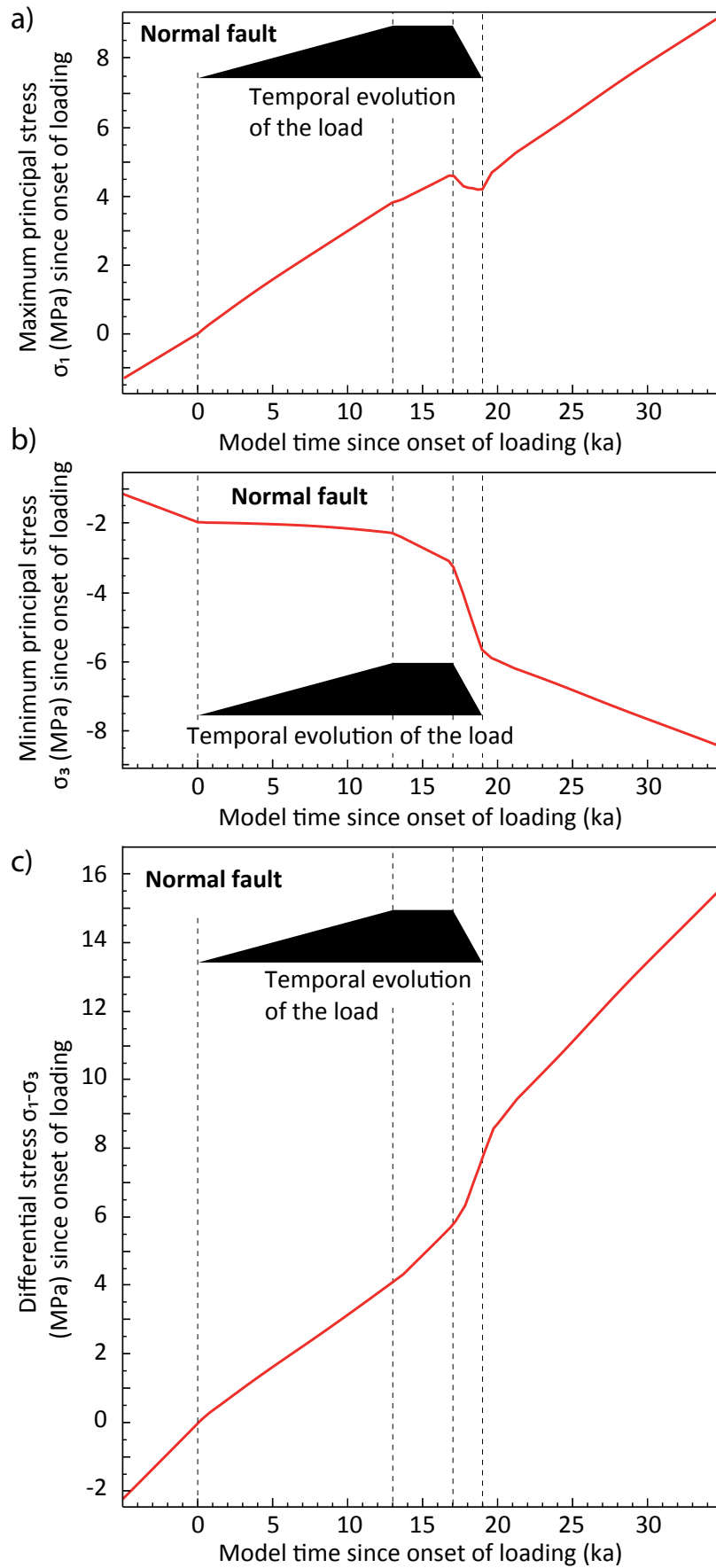


**Fig. 39:** Temporal evolution relative to the onset of loading, of the a) maximum principal stress  $\sigma_1$ , b) minimum principal stress  $\sigma_3$ , and c) differential stress  $\sigma_1 - \sigma_3$  in the normal fault reference model measured in the center of the hanging wall in 7.5 km depth. The black inset represents the temporal evolution of the load.

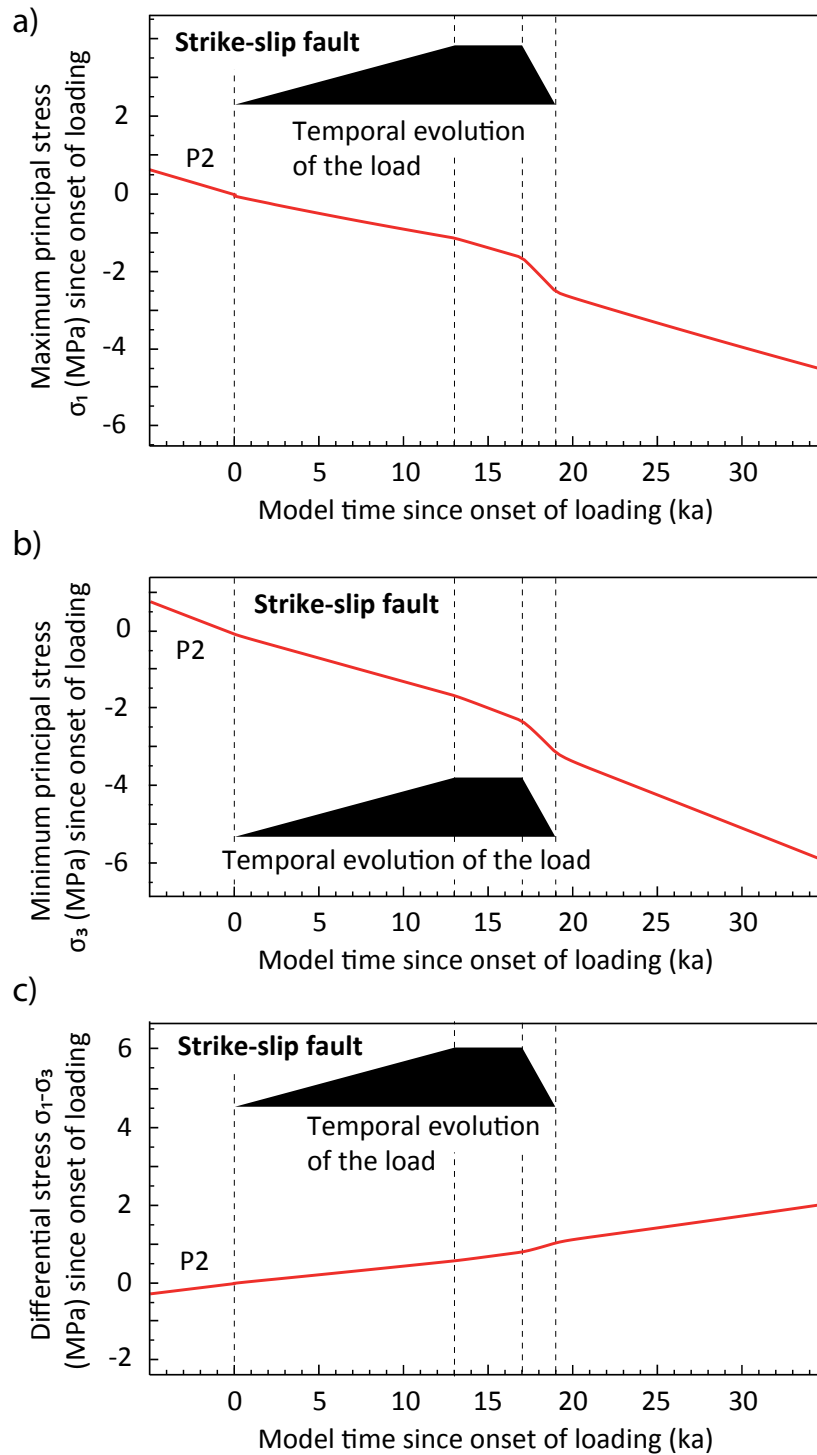


**Fig. 40:** Temporal evolution relative to the onset of loading of the a) maximum principal stress  $\sigma_1$ , b) minimum principal stress  $\sigma_3$ , and c) differential stress  $\sigma_1 - \sigma_3$  in the strike-slip fault reference model measured at point P2 in 10 km depth. The black inset represents the temporal evolution of the load.

The stress evolution in the normal fault reference model is similar to the one of the thrust fault model (Fig. 39). Lake level rise leads to an increase of  $\sigma_1$  and  $\sigma_3$ , while lake regression leads to a decrease (Fig. 39). The evolution of  $\sigma_1 - \sigma_3$  of the normal fault reference model shows a clear decrease during lake level rise and an increase during lake regression. The evolution of  $\sigma_1$  reveals a break in slope during the phase of lake regression. With the onset of unloading  $\sigma_1$  decreases.



During the first 0.5 ka the decrease of  $\sigma_1$  is faster than in the following 1.5 ka. At the end of unloading,  $\sigma_1$  increases again until 20 ka of model time and then returns to the steady-state stress field. Regarding the  $\sigma_1$ - $\sigma_3$  evolution, the break in slope of  $\sigma_1$  at 19.5 ka model time leads to an ongoing increase of  $\sigma_1$ - $\sigma_3$  during the first 0.5 ka after the end of the unloading phase, promoting faster slip on the fault until 20 ka of model time.

The principal stresses of the strike-slip fault reference model show the same basic stress evolution pattern as both models mentioned before. Lake level rise leads to an increase of  $\sigma_1$  and  $\sigma_3$ , and lake regression to a decrease (Fig. 40). This principal stress evolution leads to a decrease of  $\sigma_1$ - $\sigma_3$  of the strike-slip fault model during loading, followed by an increase during unloading, but compared to the other reference models this change in  $\sigma_1$ - $\sigma_3$  is less prominent (Fig. 40).

Although the orientation of the principal stresses during crustal shortening is totally different from the one of an extensional or a strike-slip regime, the effect of glacial loading and postglacial unloading on the slip behavior of the fault is similar in the majority of experiments made. The understanding of the effect of a load applied to the surface of the lithosphere on the crustal stress evolution is eminent when discussing the slip behavior of the thrust fault, normal fault and strike-slip fault models. The principal stress fields of a lithospheric block during crustal shortening, extension, or lateral shearing are shown in Figure 41 and Figure 42. In a lithospheric block undergoing crustal shortening, the maximum principal stress  $\sigma_1$  is horizontal, orientated in direction of maximum shortening, while the minimum principal stress  $\sigma_3$  is vertical (Fig. 41a). The application of a glacial load on the surface of the lithosphere leads to flexure of the lithosphere (Fig. 41b) and to a pronounced increase of  $\sigma_1$  and  $\sigma_3$ . While the increase in  $\sigma_3$ , which is orientated vertically in the lithosphere, is a direct consequence of the application of glacial load, the increase in  $\sigma_1$  is caused by the flexure of the lithosphere. This flexure leads to local shortening of the crust in the center of the flexure (Fig. 10, Fig. 15). The increase in the principal stresses  $\sigma_1$  and  $\sigma_3$  leads to a shift of the Mohr circle away from the line of the Mohr Coulomb failure criterion. This is the reason for the stagnation of slip on the thrust fault during loading. In contrast, the removal of the load leads to a decrease of  $\sigma_1$  and  $\sigma_3$  (Fig. 41c). The Mohr circle shifts back again and touches the Mohr Coulomb failure criterion, leading to reactivation and accelerated slip on the fault. After the end of the glaciation-deglaciation cycle, the crustal stress field returns to steady-state, and so does the slip rate of the fault (Fig. 41d).

A similar picture can be seen, regarding the principal stress fields for the normal fault. In a lithospheric block undergoing crustal extension, the maximum principal stress is vertical and the minimum principal stress is horizontal (Fig. 41e), leading to normal faulting. Loading the lithosphere leads to a direct increase of  $\sigma_1$  while the flexure caused by the load increases  $\sigma_3$  (Fig. 41f) leading to decelerated slip, and in turn, unloading leads to a decrease of  $\sigma_1$  and  $\sigma_3$  (Fig. 41g) and to accelerated slip on the fault. In analogy to the thrust fault case,  $\sigma_1$  and  $\sigma_3$  return to steady-state after the removal of the surface load (Fig. 41h).

Lateral shearing of a lithospheric block in case of the strike-slip fault leads to a horizontal orientation of  $\sigma_1$  and  $\sigma_3$  (Fig. 42a). In this case, both  $\sigma_1$  and  $\sigma_3$  increase during loading as a direct

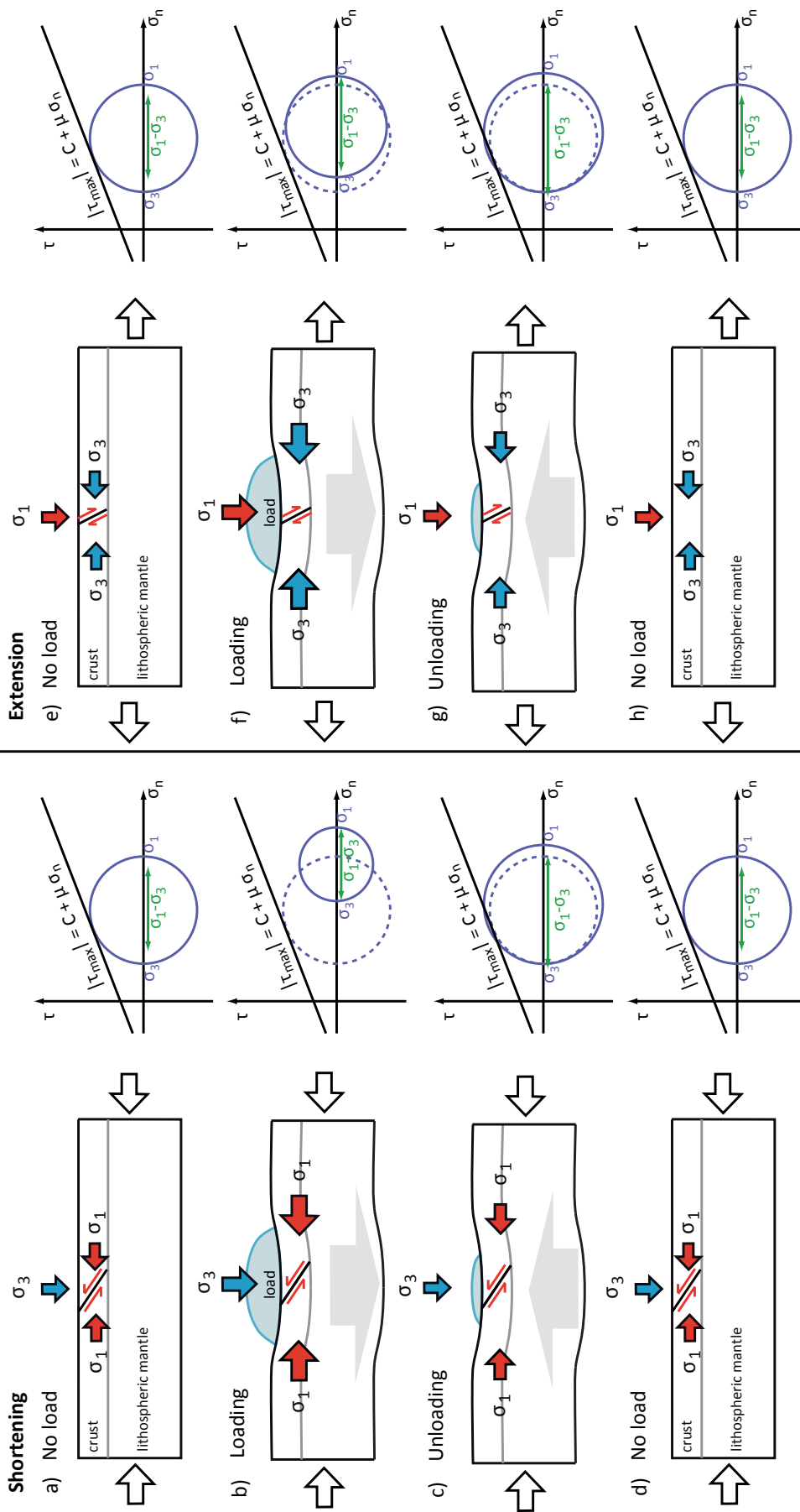


**Fig. 41:** Schematic sketch of the principal stress orientation in the model lithosphere prior to loading, during loading, during unloading, and after completion of the loading-unloading cycle for a)-c) the thrust fault, e)-h) the normal fault. For each fault, the Mohr's circle for stress is plotted, in reference to the stress state prior to loading (dashed circle) and under maximum load. Note that the size of the arrows marking the principal stress orientation represents the relative stress change. For each loading state, a schematic evolution of the Mohr's circle for stress is plotted where  $\sigma_n$  is the normal stress,  $\tau$  the shear stress,  $c$  the cohesion,  $\mu$  the coefficient of friction and  $\tau_{max}$  the maximum shear stress.

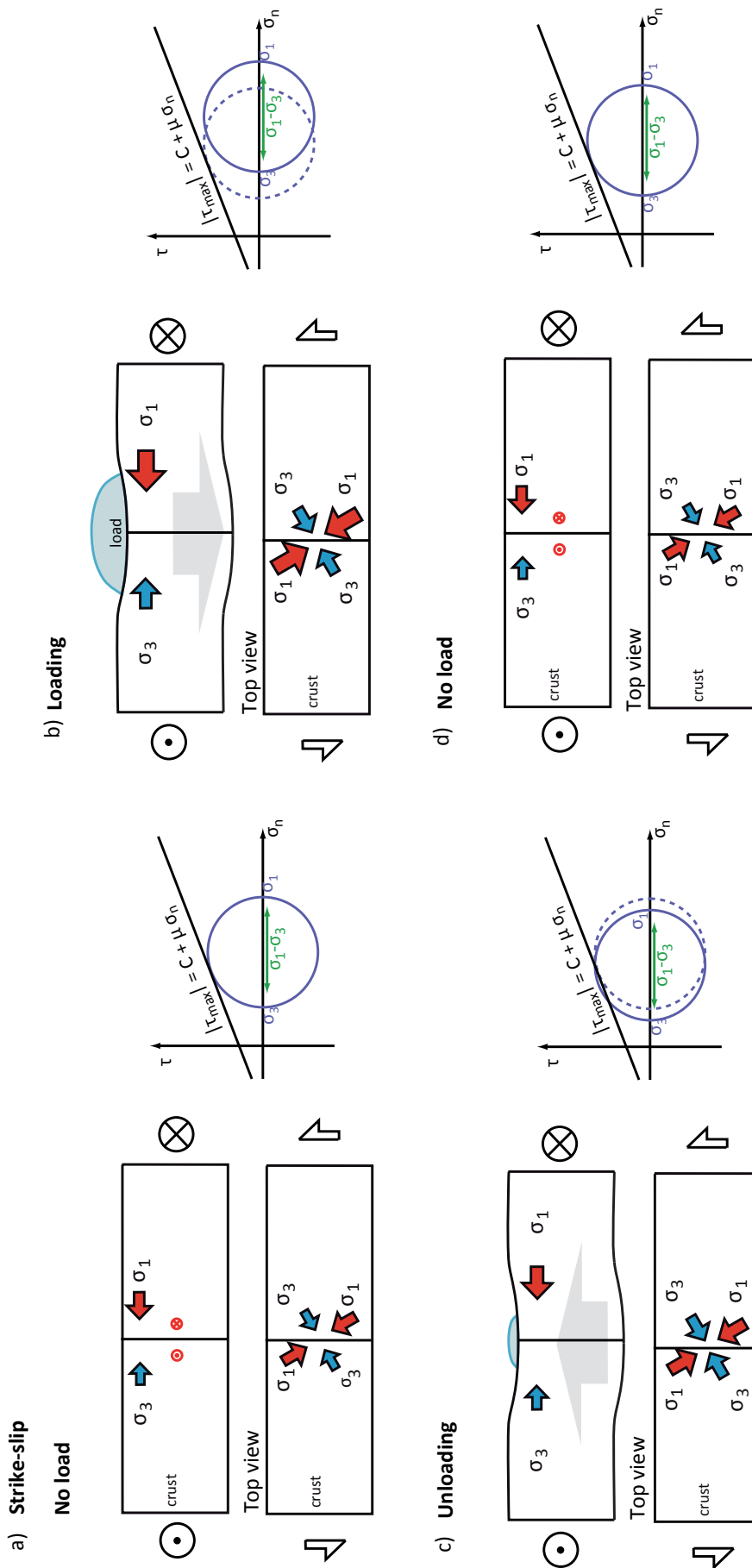


**Fig. 42:** Schematic sketch of the principal stress orientation in the strike-slip model lithosphere a) prior to loading, b) during loading, c) during unloading, and d) after completion of the loading and unloading cycle. The Mohr's circle for stress is plotted, in reference to the stress state prior to loading (dashed circle) and under maximum load. Note that the size of the arrows marking the principal stress orientation represents the relative stress change. For each loading state, a schematic evolution of the Mohr's circle for stress is plotted where  $\sigma_n$  is the normal stress,  $\tau$  the shear stress,  $c$  the cohesion,  $\mu$  the coefficient of friction and  $\tau_{max}$  the maximum shear stress.

consequence of the flexure caused by the load, leading again to decelerated slip on the fault as the Mohr's circle shifts away from the line of the failure criterion (Fig. 42b). Unloading leads to a decrease of  $\sigma_1$  and  $\sigma_3$  and thus to a shift of the Mohr's circle towards the failure envelope resulting in accelerated slip (Fig. 42c). Steady-state  $\sigma_1$  and  $\sigma_3$  is reached again after the removal of the load (Fig. 42d). In all models, the general temporal evolution of the Mohr circle is similar. Loading leads to a shift of the Mohr circle away from the line of the Mohr Coulomb failure criterion while, with the onset of unloading, the Mohr circle shifts back touching the failure envelope. During a phase of constant load, the Mohr circle returns to its steady-state position.

### 4.3 The principal stress evolution of selected experiments from the parameter study

As shown in chapter 2.2, the reference models have been tested by varying parameters in the model, like the load thickness, the rheology of the lithosphere or the fault dip. All these parameters have a major or minor influence on the slip rate evolution of the faults. In the following, the evolution of the principal stresses of selected experiments will be discussed to explain the effect of these parameters on the stress evolution in the model lithosphere.

Varying the ice thickness in the thrust fault experiments shows a higher increase in the principal stresses with increasing load. The timing of the changes in the principal stresses for the experiments with glaciers thicker than 500 m is similar to the ones of the reference model. Here the same changes in slope angle of decreasing  $\sigma_1$  during the interval of unloading can be seen (Fig. 43a). As in the reference model, these changes in slope angle of the stress curve correspond to the reactivation of slip on the fault. The point of slope angle change of the curve shifts closer to the end of the unloading phase with increasing load thickness. The experiments with glaciers of 250 m and 100 m of ice show a different pattern in the evolution of  $\sigma_1$ . Here the change in slope during the interval of unloading is missing, caused by the fact that faulting does not stop. Slip on the fault decelerates during loading (Fig. 43a). Looking at the evolution of  $\sigma_1$ - $\sigma_3$  for the experiments with varying glacial load, the differential stress plots for the experiments with 1000 m and 2000 m of glacial ice load show the same peak during the phase of unloading as the differential stress plot of the reference model. Increasing ice thickness throughout the experiments leads to a shift of the break in slope of the differential stress curve, closer to the end of unloading (Fig. 43c). A variation in load thickness on the surface of the thrust fault model mainly affects  $\sigma_3$ . The higher the load, the deeper the flexure and thus the larger the increase in  $\sigma_3$  induced by the flexure (Fig. 43b). A thicker load leads to a higher increase in  $\sigma_1$ - $\sigma_3$  and a thinner load to a smaller increase, compared to the reference model (Fig. 43c).

As in the thrust fault models with varying load thickness, the principal stresses in the normal fault model also show a higher increase in  $\sigma_1$  and  $\sigma_3$  with increasing load thickness (Fig. 43d,e). In contrast to the evolution of  $\sigma_1$  in the thrust and strike-slip fault model,  $\sigma_1$  in the normal fault model shows nearly no response to the increasing load thickness during loading (Fig. 43d). Remarkably, the main difference in the evolution of  $\sigma_1$  in the normal fault experiments compared to the thrust

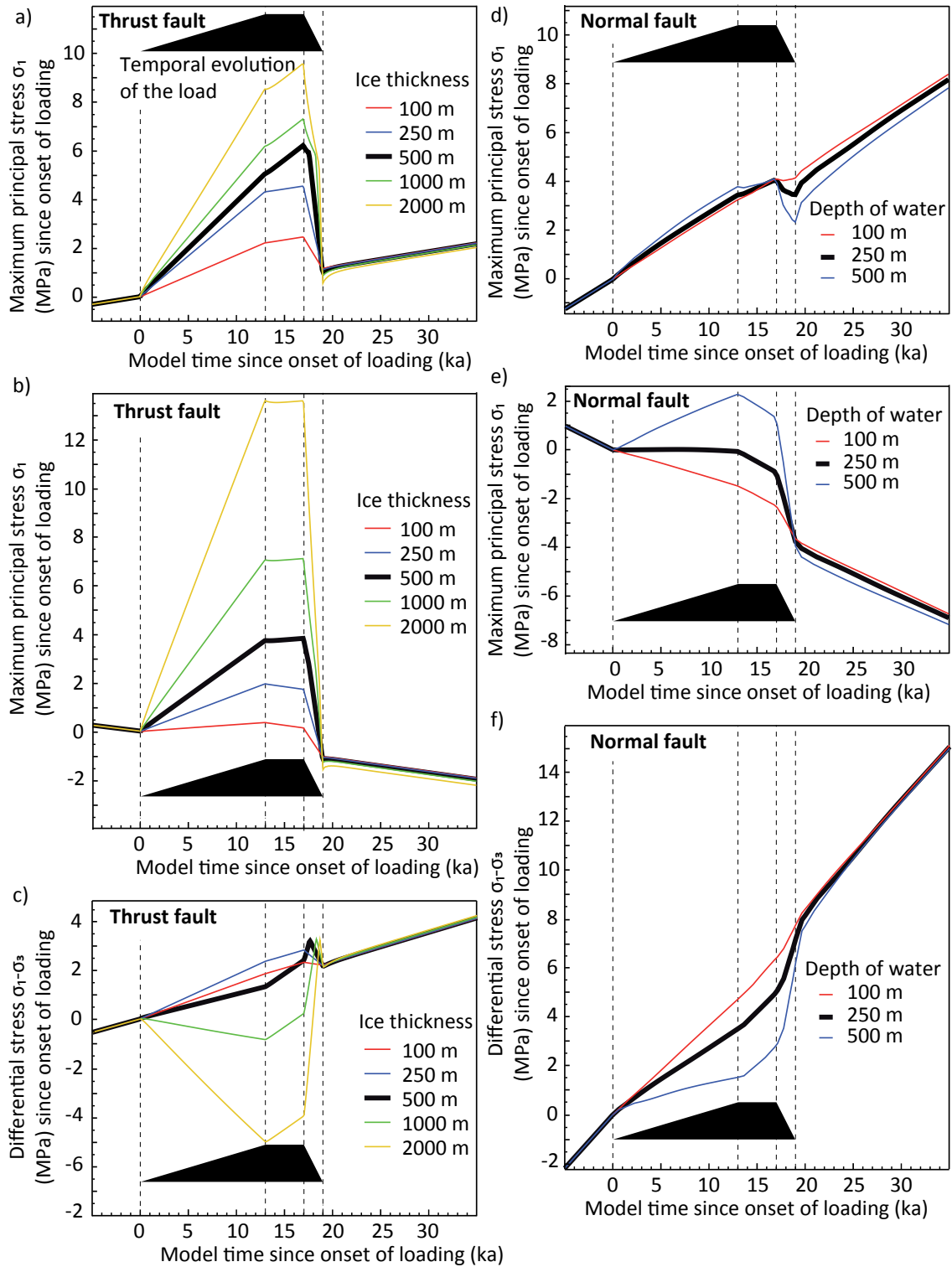


**Fig. 43:** Temporal evolution relative to the onset of loading of a) the maximum principal stress  $\sigma_1$ , b) the minimum principal stress  $\sigma_3$ , and c) the differential stress  $\sigma_1 - \sigma_3$  in the thrust fault experiments for a variable ice load and d) the maximum principal stress  $\sigma_1$ , e) the minimum principal stress  $\sigma_3$ , and f) the differential stress  $\sigma_1 - \sigma_3$  in the normal fault experiments for a variable water depth, measured in the center of the hanging wall in 7.5 km depth. The results of the reference models are marked by the thick black curves. The black inset represents the temporal evolution of the load.

fault experiments occurs during unloading, where the stress drop and the stress increase in the first 0.5 ka after the completion of unloading gets larger with thicker loads (Fig. 43d).

Changing the rheology of the thrust fault model mainly affects the evolution of  $\sigma_1$ , as a variation of the lower crust viscosity and the viscosity of the lithospheric mantle changes the overall viscosity of the model lithosphere and thus has a direct influence on the depth of the flexure that is induced by the surface load over time. Still loading of the model lithosphere leads to a shift of the Mohr circle away from the Mohr coulomb failure criterion. Changing the lower crust viscosity from  $1 \times 10^{19}$  Pa s to  $1 \times 10^{21}$  Pa s and thus increasing the overall viscosity, leads to a higher increase in  $\sigma_1$  during the glacial interglacial loading cycle (Fig. 44a). The experiment simulating a lithosphere with a strong lower crust compared to the lithospheric mantle, calculated with a lower crust viscosity of  $1 \times 10^{23}$  Pa s and a lithospheric mantle viscosity of  $1 \times 10^{20}$  Pa s shows a deeper flexure. This rheology was tested in analogy to the rheology used in the normal fault reference model and it leads to the highest increase of  $\sigma_1$  of all experiments made regarding a variable rheology (Fig. 44a). The result is an increase of  $\sigma_1 - \sigma_3$  during loading and a decrease during unloading. As  $\sigma_3$  stays nearly unaffected throughout all experiments with varying rheology, the development of the differential stress is mainly dependent on the maximum principal stress. Although the differential stress evolution predicts a slip rate increase during loading and a decrease during unloading, the slip evolution of this experiment follows a principal slip pattern as seen in the parameter study in chapter 3.2.4. The increase in  $\sigma_1 - \sigma_3$  is smaller than the increase in  $\sigma_3$  during loading which still leads to promoted slip on the fault.

All experiments tested on the effect of the rheology on the slip behavior of normal faults during glaciation and deglaciation were made modeling a lithosphere with a strong lower crust and a weak lithospheric mantle. As described in the results, the slip history of all these experiments is characterized by a slip rate decrease during loading and an increase during unloading. In analogy to the rheology tested for the thrust fault models, one experiment has been calculated for a lithosphere, consisting of a weak lower crust underlain by a strong lithospheric mantle. The slip history of this experiment differs totally from all other normal fault experiments, as an increase in the slip rate of the fault can be seen during loading, while the phase of unloading leads to a decrease in the slip rate (Fig. 37b). The maximum principal stress  $\sigma_1$  for most of the normal fault experiments with variable rheology (Fig. 44d) shows a smaller increase during loading than the increase in  $\sigma_3$  (Fig. 44e). In the experiment, in which a lower crust viscosity of  $1 \times 10^{21}$  Pa s is tested,  $\sigma_1$  even decreases during loading. Such a stress behavior can be explained by looking at the slip distribution on the fault itself. The difference between slip on the surface of the fault and slip accumulated in 7.5 km depth for a vertical profile in the center of the fault has been calculated and plotted against model time (Fig. 45). In the experiment with a lower crust viscosity of  $1 \times 10^{21}$  Pa s, the slip on the fault first decelerates at the surface and later on in 7.5 km depth, leading to a vertical elongation of the hanging wall and thus to a decrease in  $\sigma_1$  during loading (Fig. 45). All other experiments, apart from the experiment with a lower crust viscosity of  $1 \times 10^{23}$  Pa s, show a similar behavior regarding the differential slip history in Figure 45, leading to a damping effect on the increase in  $\sigma_1$

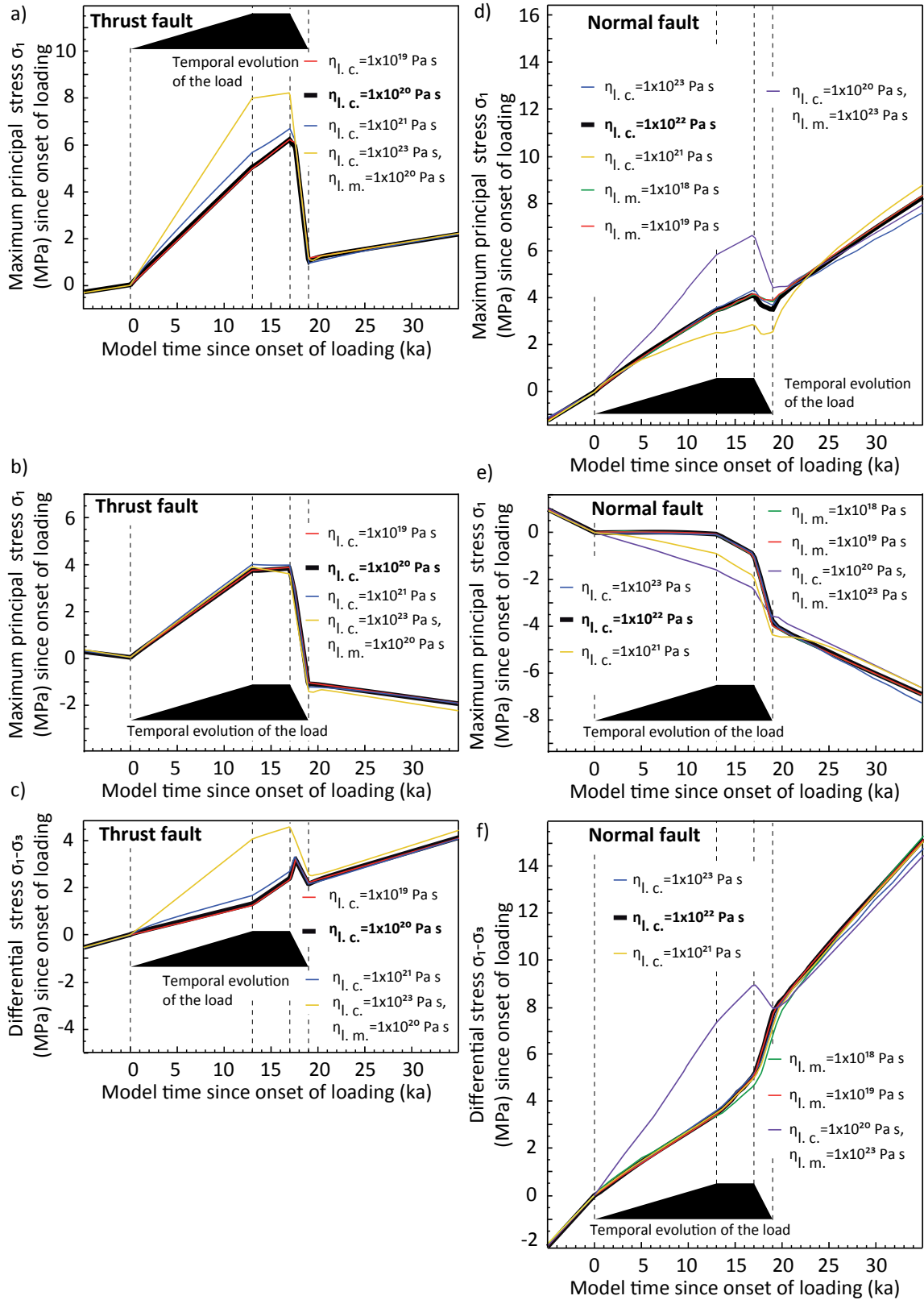


**Fig. 44:** Temporal evolution relative to the onset of loading of a) the maximum principal stress  $\sigma_1$ , b) the minimum principal stress  $\sigma_3$ , and c) the differential stress  $\sigma_1 - \sigma_3$  in the thrust fault experiments and d) the maximum principal stress  $\sigma_1$ , e) the minimum principal stress  $\sigma_3$ , and f) the differential stress  $\sigma_1 - \sigma_3$  in the normal fault experiments with varying rheology, measured in the center of the hanging wall in 7.5 km depth. The results of the reference models are marked by the thick black curves. The black inset represents the temporal evolution of the load.

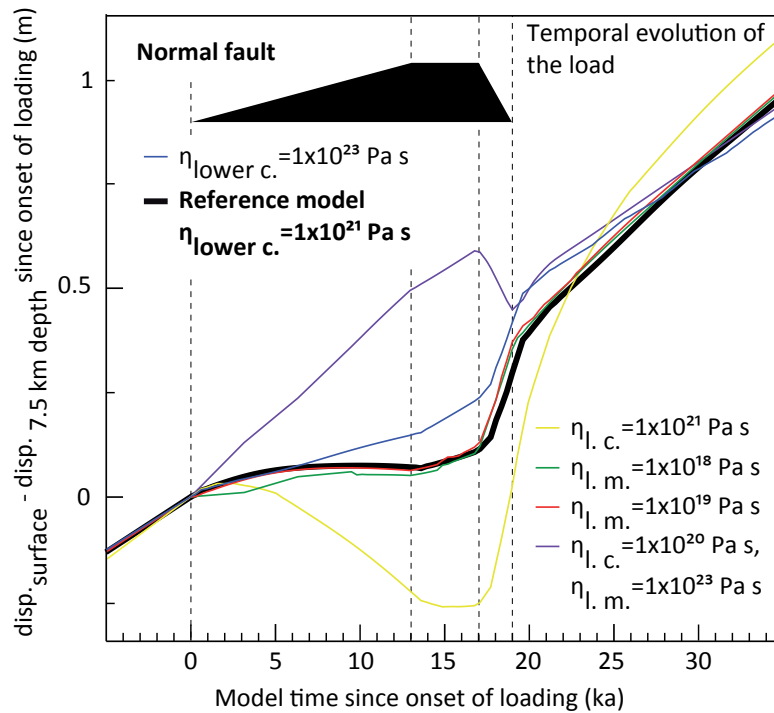


**Fig. 45:** Differential slip history for the normal fault experiments with varying rheology between a point at the surface and in 7.5 km depth, measured in the center of the normal fault with varying rheology.

during loading. In the experiment in which the lithospheric mantle with a viscosity of  $1 \times 10^{23} \text{ Pa s}$  is stronger than the lower crust with a viscosity of  $1 \times 10^{20} \text{ Pa s}$ , as used in the thrust fault reference model, the increase of  $\sigma_1$  by far exceeds the increase in  $\sigma_3$  during loading. As a result,  $\sigma_1 - \sigma_3$  in this normal fault experiment increases during loading, while  $\sigma_1 - \sigma_3$  in all other normal fault experiments shows a decrease (Fig. 44f). The increase of  $\sigma_1 - \sigma_3$  during loading leads to a growth of the Mohr's circle that consequently touches the failure envelope. This leads to promoted slip on the fault during loading and to a decreased slip rate on the fault during unloading.

Changing the dip of the thrust fault mainly affects the evolution of the maximum principal stress which is orientated horizontally in the model (Fig. 46a-c). Regarding  $\sigma_1 - \sigma_3$  of the reference model and the experiment using a  $60^\circ$  dipping thrust fault, the steeper dipping fault shows a much clearer decrease during loading and increase during unloading than the differential stress evolution of the reference model. Changing the dip of the normal fault model from  $60^\circ$  in the reference model to  $30^\circ$  leaves the basic timing of the  $\sigma_1$ ,  $\sigma_3$  and thus the evolution of  $\sigma_1 - \sigma_3$  nearly unaffected (Fig. 46d-f).

Comparing the evolution of the principal stresses in the thrust fault, normal fault, and the strike-slip model, reveals whether  $\sigma_1$ ,  $\sigma_3$ , or both  $\sigma_1$  and  $\sigma_3$  modulate the slip behavior of the faults investigated. In the thrust fault model the increase of  $\sigma_1$  during loading and the decrease during unloading is by one third higher than the increase of  $\sigma_3$  (Fig. 38). Thus it is mainly the maximum principal stress, which is orientated horizontally in the model, that controls the slip on the fault. In the normal fault model the increase in  $\sigma_3$  during loading and the decrease during unloading is much higher than the change in  $\sigma_1$  (Fig. 39). Here  $\sigma_3$ , also being orientated horizontally in the



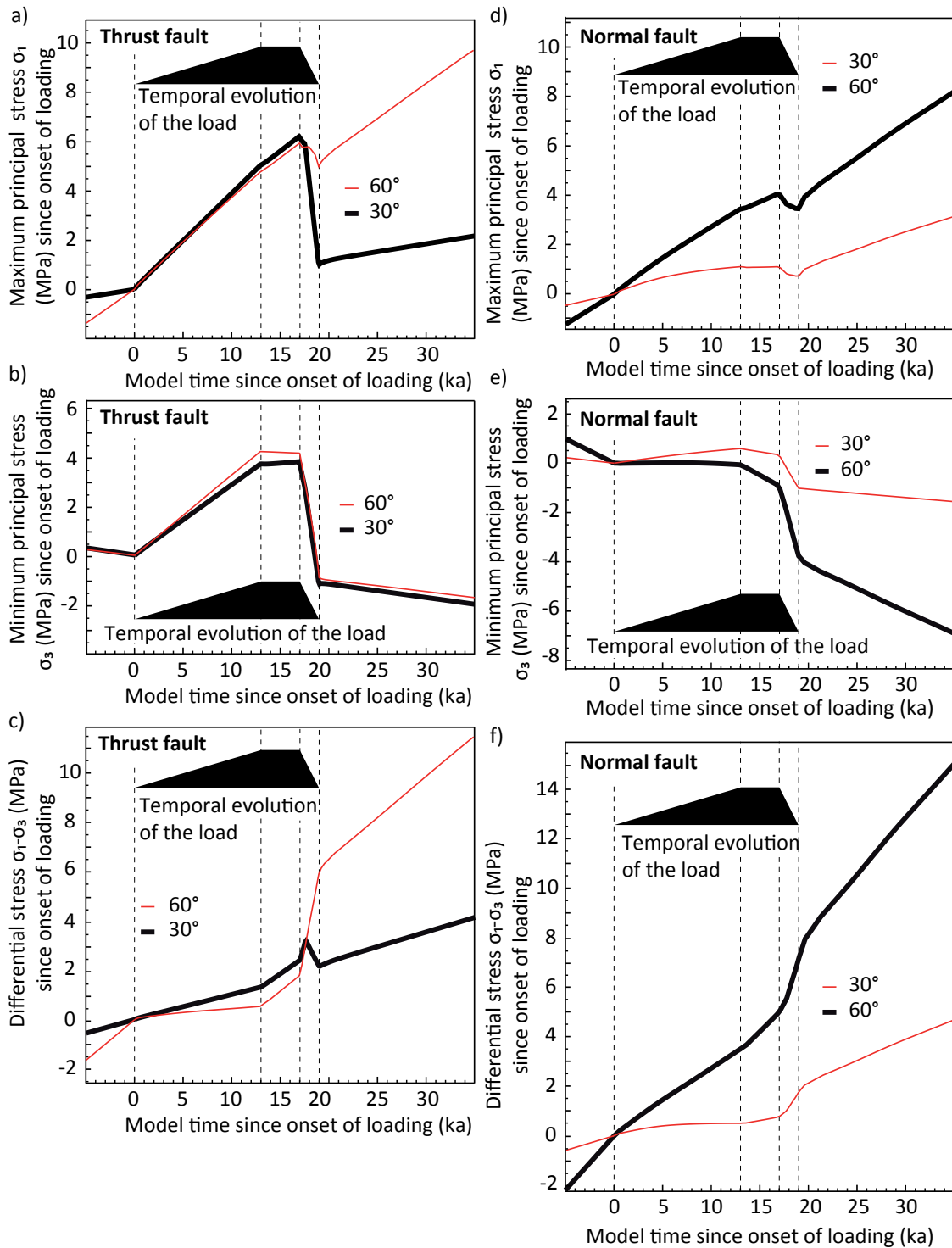


**Fig. 46:** Temporal evolution relative to the onset of loading of a) the maximum principal stress  $\sigma_1$ , b) the minimum principal stress  $\sigma_3$ , and c) the differential stress  $\sigma_1 - \sigma_3$  in the thrust fault experiments and d) the maximum principal stress  $\sigma_1$ , e) the minimum principal stress  $\sigma_3$ , and f) the differential stress  $\sigma_1 - \sigma_3$  in the normal fault experiments varying fault dip, measured in the center of the hanging wall in 7.5 km depth. The results of the reference models are marked by the thick black curves. The black inset represents the temporal evolution of the load.

model, controls the slip on the fault. As the evolution of  $\sigma_1$  and  $\sigma_3$  in the strike-slip fault model is the same (Fig. 40) and both stresses are orientated horizontally in the model, slip on the strike-slip fault is equally controlled by both stresses, the maximum ( $\sigma_1$ ) and the minimum principal stress ( $\sigma_3$ ). In summary, the differential stress plots of all three reference models and the experiments made during the parameter study show that the changes in the slip rate on the faults, affected by changes in the surface load are mainly controlled by the horizontal stresses in the lithosphere. In contrast to the assumptions made by Johnston (1987), that large continental ice sheets in general suppress seismic activities, the model results show that the seismicity is mainly affected by a change in the load. A static load leads to the readjustment of the steady-state stress field over long time spans and consequently to a seismicity similar to the pre-loading state.

## 4.4 Application to natural faults

### 4.4.1 Normal faults

The normal fault models have been applied to the Basin and Range Province, a region of ongoing east-west extension with rates of 6-7 mm/a relative to the Colorado Plateau determined by the Basin and Range Geodetic Network (BARGEN) (Wernicke et al., 2000). During the Last Glacial Maximum, this area was covered by two large pluvial lakes (Fig. 47), Lake Bonneville, covering 52000 km<sup>2</sup> (Bills et al., 1994) of the eastern part of the Basin and Range, and Lake Lahontan that was located in the western part of the Basin and Range Province covering about 22500 km<sup>2</sup> (Bills et al., 2007). Both

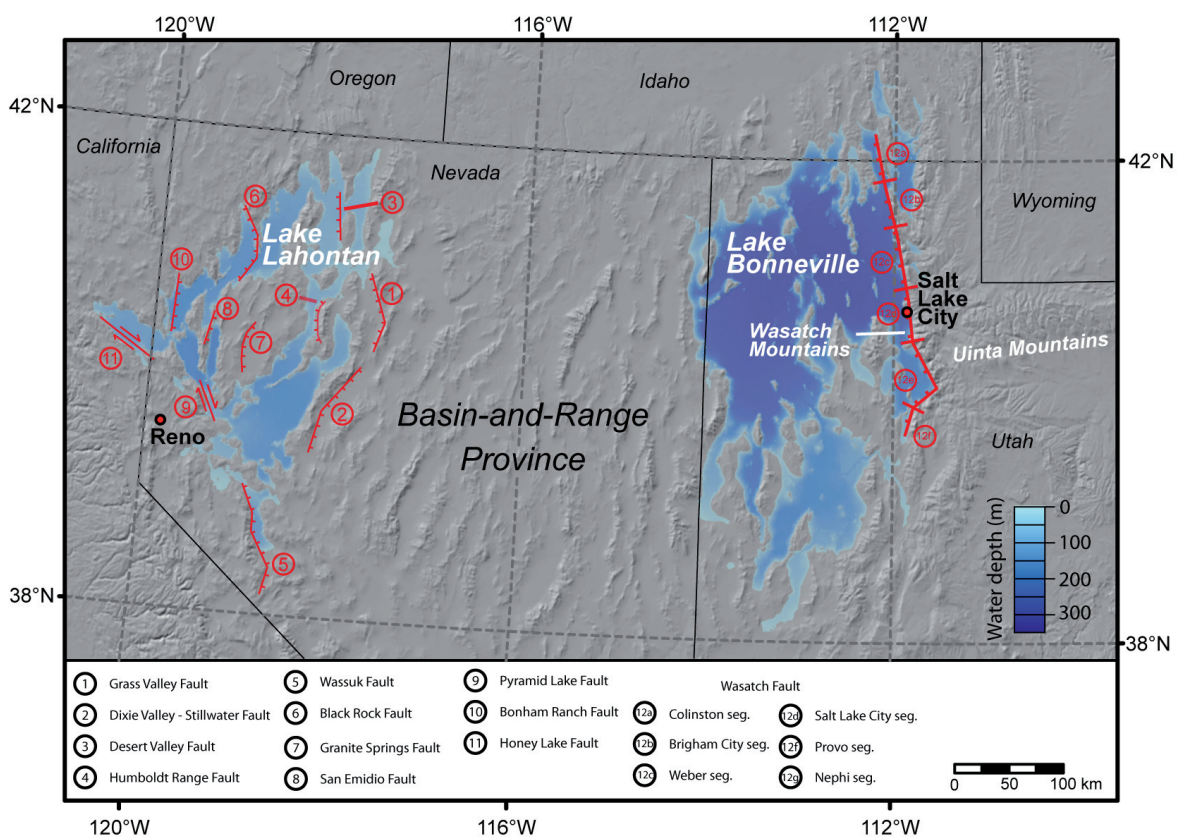
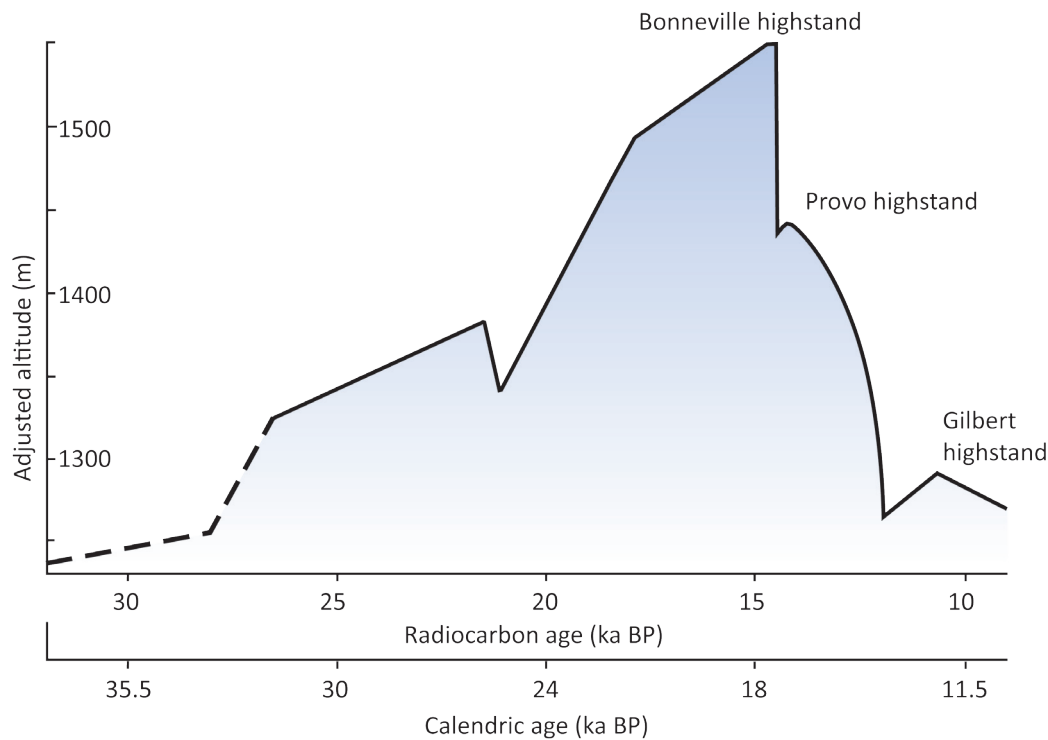


Fig. 47: Map of the Basin and Range Province with the location of Lake Bonneville and the Wasatch Fault, and Lake Lahontan with major faults (Adams et al., 1999).

of these lakes experienced a tremendous loss of water volume after the Last Glacial Maximum leading to isostatic rebound of the lithosphere (Watts, 2001).

The lake level history of Lake Bonneville is well constrained by radiocarbon ages of samples taken along the shorelines and sequence stratigraphy (Fig. 48) (Oviatt et al., 1992). For Lake Bonneville, three major highstands and their lateral extents have been reconstructed, the first one being the Bonneville at 17.5 ka, the second the Provo at 16.7 ka, and the third one the Gilbert highstand at 10.2 ka before present (Currey, 1982; Burr and Currey, 1988; Bills et al., 1994). The present remnant of Lake Bonneville is the Great Salt Lake. The most prominent drop of the Lake



**Fig. 48:** Reconstructed lake level curve of Lake Bonneville highstand since 36 ka after Oviatt et al. (1992).

Bonneville lake level of nearly 100 m in just 100 years (Oviatt et al., 1992) has been dated between 16.5 ka to 17.4 ka BP. The eastern coastline of Lake Bonneville during the Bonneville highstand was formed in the hanging wall of the 370-km-long north-south-striking west-dipping Wasatch Fault that builds up the Wasatch Mountains. The Wasatch Mountains as also the Uinta Mountains located east of the Wasatch Range, were covered by glaciers during the Last Glacial Maximum (Laabs and Carson, 2005; Munroe, 2005). The subsurface geometry of the Wasatch Fault has been constrained by using structural, borehole, gravity and seismic reflection data giving near surface dip angles between 30°-70° but having an average dip of 20°-30° (Friedrich et al., 2003 and references therein). The metropolitan area of Salt Lake City is located directly on the fault trace in the center of the Wasatch Fault. Thus the paleoseismological record due to seismic hazard assessments of the Wasatch Fault is very good. The Wasatch Fault can be subdivided into at least 10 segments on the basis of geomorphic, topographic, geophysical, geodetic, and paleoseismological data (Swan et al., 1980; Schwartz and Coppersmith, 1984; Machette et al., 1991; McCalpin and Nishenko, 1996). From North to South the fault consists of the Malad City, Clarkston Mountain, Collinston, Brigham City, Weber, Salt Lake City, Provo, Nephi, Levan, and Fayette segment. Regarding the long-term slip behavior, the segmentation disappears, and the fault can be interpreted as one big fault (Armstrong et al., 2004). The long-term slip rate of the Wasatch Fault has been estimated to be 0.3 mm/a (Friedrich et al., 2003).

In contrast to Lake Bonneville, Lake Lahontan consists of a ring shaped waterbody (Fig. 47). The lake level history has been compiled by Bills et al. (2007) dating the highstand of Lake Lahontan at about 15 ka BP, followed by a lake level drop of 200 m over 6 ka (Bills et al. 2007). While the area of former Lake Bonneville is dominated by one big fault, the area around and below ancient

Lake Lahontan is characterized by an array of north-south striking normal faults, dipping to the West as also to the East and northwest-southeast striking strike-slip faults further to the West. All these faults have an average length of 30-40 km building up a fault array with an average spacing of about 30-50 km.

### ***Estimation of the volume of the Lake Bonneville and Lake Lahontan water body***

The extent of the glaciers on the Wasatch and Uinta Mountains is well constrained by mapping of trimlines and terminal moraines (Laabs and Carson, 2005; Munroe, 2005; Roth, 2006; Bartsch, 2006). The ice mass is estimated to be 426 km<sup>3</sup> for the Uinta Mountains (Roth 2006) and 46 km<sup>3</sup> for the Wasatch Mountains (Bartsch, 2006). To investigate the effect of the Lake Bonneville lake level history on the slip behavior of the Wasatch Fault and the effect of Lake Lahontan on the bounding faults it is essential to determine the volume of Lake Bonneville and Lake Lahontan and their evolution through time. The first work investigating ancient Lake Bonneville was published by Gilbert (1890) in the course of a reconnaissance survey of shoreline deposits of the Bonneville

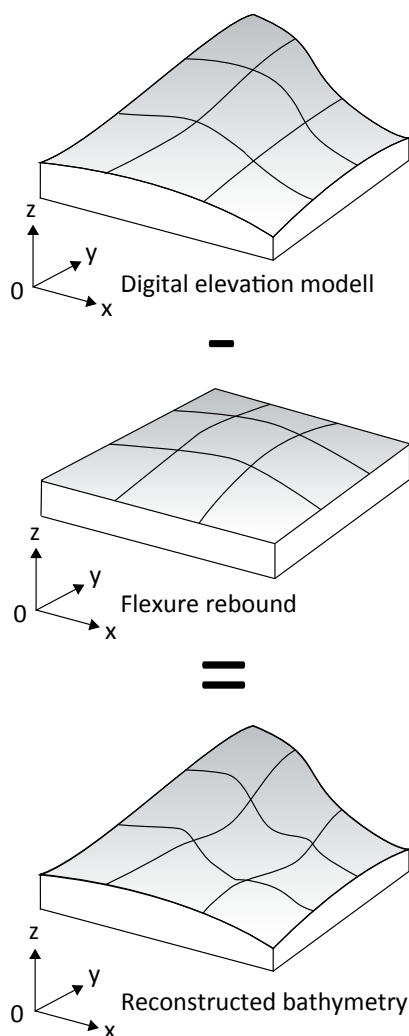


**Fig. 49:** Schematic sketch off the method used for the bathymetric reconstruction, based on digital raster elevation data.

basin. Gilbert discovered that the paleo-shorelines in the center of the basin were elevated by tens of meters over their counterparts on the basins margin. He came to the conclusion that the load of the Lake Bonneville water body must have depressed the Earth's crust causing flexure. Gilbert (1890) recognized that each set of paleo-shorelines must have formed as level surfaces. After the removal of the water body, the crust experienced rebound to its present state (Watts, 2001). By mapping the paleo-shorelines, the extent and shape of the loading-induced flexure for each highstand can be obtained (Currey, 1982; Burr and Currey, 1988; Bills et al., 1994). In addition, a distinct Lake Bonneville lake level history has been derived by Oviatt et al. (1992) using radiocarbon dating and sequence stratigraphy (Fig. 48). To model the load cycle of Lake Bonneville, the major three highstands, i.e. the Bonneville at 17.5 ka, the Provo at 16.7 ka and the Gilbert highstand at 10.2 ka, have been taken into account.

To calculate the volume of the water body at each highstand, digital elevation data of the Bonneville basin, using SRTM (Shuttle Radar Topography Mission) raster data with a grid spacing of 100 m, and paleo-shoreline point elevation data by Bills et al. (1994) have been gathered in a GIS (Geographic Information System). From the

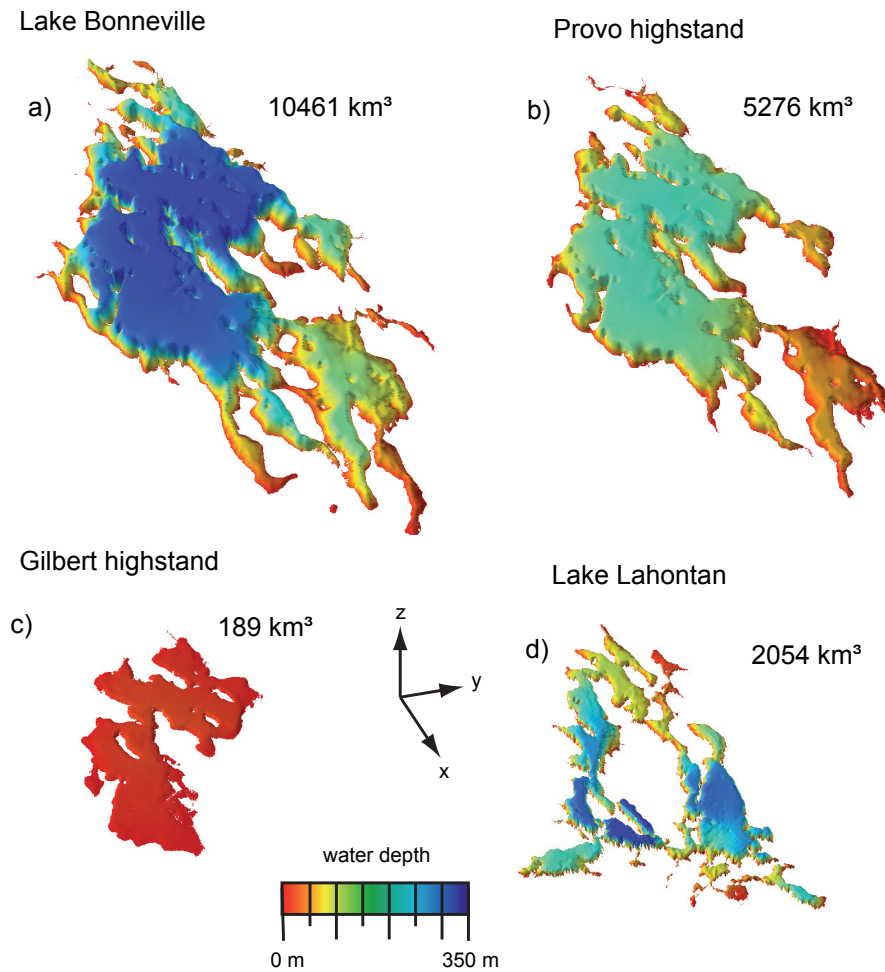


**Fig. 50:** Reconstructed water bodies of the three major highstands of Lake Bonneville: a) Bonneville highstand at 17.5 ka BP, b) Provo highstand at 16.7 ka BP, and c) Gilbert highstand at 10.2 ka BP. d) Reconstructed water body of Lake Lahontan at 15 ka BP.

paleo-shoreline point elevation data, the points for the three highstands have been extracted and interpolated to raster data sets, representing the geometry of the flexure at Bonneville, Provo, and Gilbert highstand. The calculation of the volume of a water body assumes that the exact bathymetry of the lake is known while the surface of the lake is represented by a horizontal plane. The lake itself represents a load that causes a flexure of the Earth's crust and thus modulates its own bathymetry. For the Bonneville, Provo and Gilbert highstands the bathymetry has been reconstructed by subtracting the rebound pattern raster datasets from the digital elevation model of the Bonneville Basin (Fig. 49). The reconstructed bathymetric raster datasets have been calculated with a grid spacing of 100 m to preserve vertical accuracy. The lake's water surface elevation over sea level of each highstand is given by the lake level curve published by Oviatt et al. (1992). Subtracting the elevation for each highstand from the corresponding reconstructed bathymetric dataset and erasing all negative values, three datasets were generated that represent the water bodies at the Bonneville, Provo and Gilbert highstands. The reconstructed Lake Bonneville water body has a volume of 10461 km<sup>3</sup>. For the Bonneville water bodies during the Provo and Gilbert highstand, volumes of 5276 km<sup>3</sup> and 189 km<sup>3</sup> were calculated.

Following the same procedure the water body volume of Lake Lahontan has been calculated using lake level data from Adams and Wesnousky (1998), Benson and Thomson (1987), Benson et al. (1992, 1995, 1996, 1997) and Davis (1983, 1987) compiled in Bills et al. (2007). In contrast to Lake Bonneville, only one major highstand has been described for the Lake Lahontan (Bills et al., 2007). The flexural rebound pattern after the removal of Lake Lahontan has been calculated using paleo-shoreline elevation data of Adams et al. (1999) and Bills et al. (2007). The reconstructed volume of Lake Lahontan at its highstand is 2054 km<sup>3</sup> (Fig. 50).

### ***Model approach***

Two models have been designed to investigate the response of faults to loading by Lake Bonneville and Lake Lahontan (Karow and Hampel, in prep). The models use a similar setup as introduced in the parameter study, i.e. a 1000 km x 1000 km wide and 100 km thick lithosphere, subdivided into an elastic upper crust, a viscoelastic lower crust and a viscoelastic lithospheric mantle. The rheology used for the three layered model lithosphere has been chosen according to viscosity profiles determined by Nakiboglu and Lambeck (1983), Bills and May (1987) and Bills et al. (1994, 2007). The viscoelastic lower crust has been implemented with a viscosity of  $1 \times 10^{22}$  Pa s and the viscoelastic lithospheric mantle with a viscosity of  $1 \times 10^{18}$  Pa s. The models are extended at 6 mm/a (Wernicke et al., 2000) (Fig. 51a). Similar to the reference models, the faults are implemented in the center of the model lithosphere. The Wasatch Fault in the Lake Bonneville model dips with 30° (Friedrich et al., 2003) (Fig. 51b). Only the six central segments of the Wasatch Fault are implemented in the model, starting in the North with the Collinston segment reaching to the Nephi segment in the South. The Lake Lahontan model contains eleven of the most prominent faults (Fig. 51c) of the region, implemented as discrete fault planes, the Pyramid Lake Fault and the Honey Lake Fault, being vertical and act as strike-slip faults, the other faults, (nomenclature according to Fig. 47) dipping 45° to the East, some to the West acting as normal faults. In contrast to any other model designed in this study, the Lake Lahontan model represents a fault array of eleven faults. The lake loads on both models are implemented by using several surface partitions, on which different pressures reflecting different water depth can be applied (Fig. 51b, c). In addition, partitions representing the location of the glacial ice on the Uinta and Wasatch Mountains are included on the surface of the Lake Bonneville model (Fig. 51b). As in the reference models in the parameter study, the temporal evolution of the load is controlled by a loading function. In the Lake Bonneville model, this loading function follows the lake level history by Oviatt et al. (1992) (Fig. 48). The function starts with 14.9 ka of loading to Lake Bonneville highstand, lasting for 1 ka. This highstand is followed by the Bonneville flood, lasting for 0.1 ka, unloading to the Lake Provo highstand. This highstand lasts for 0.7 ka, before the lake level drops further to 5 m over a time of 2.9 ka. The following rise of Lake Gilbert takes 2.4 ka and is ended by a drop of the lake level to present Great Salt Lake water level of 5 m again. The lateral extension during the different highstands of Lake Bonneville is simulated by different sub-functions. These sub-functions follow the timing of the main loading function and deactivate the surface partition, if the lake level falls below the terrain

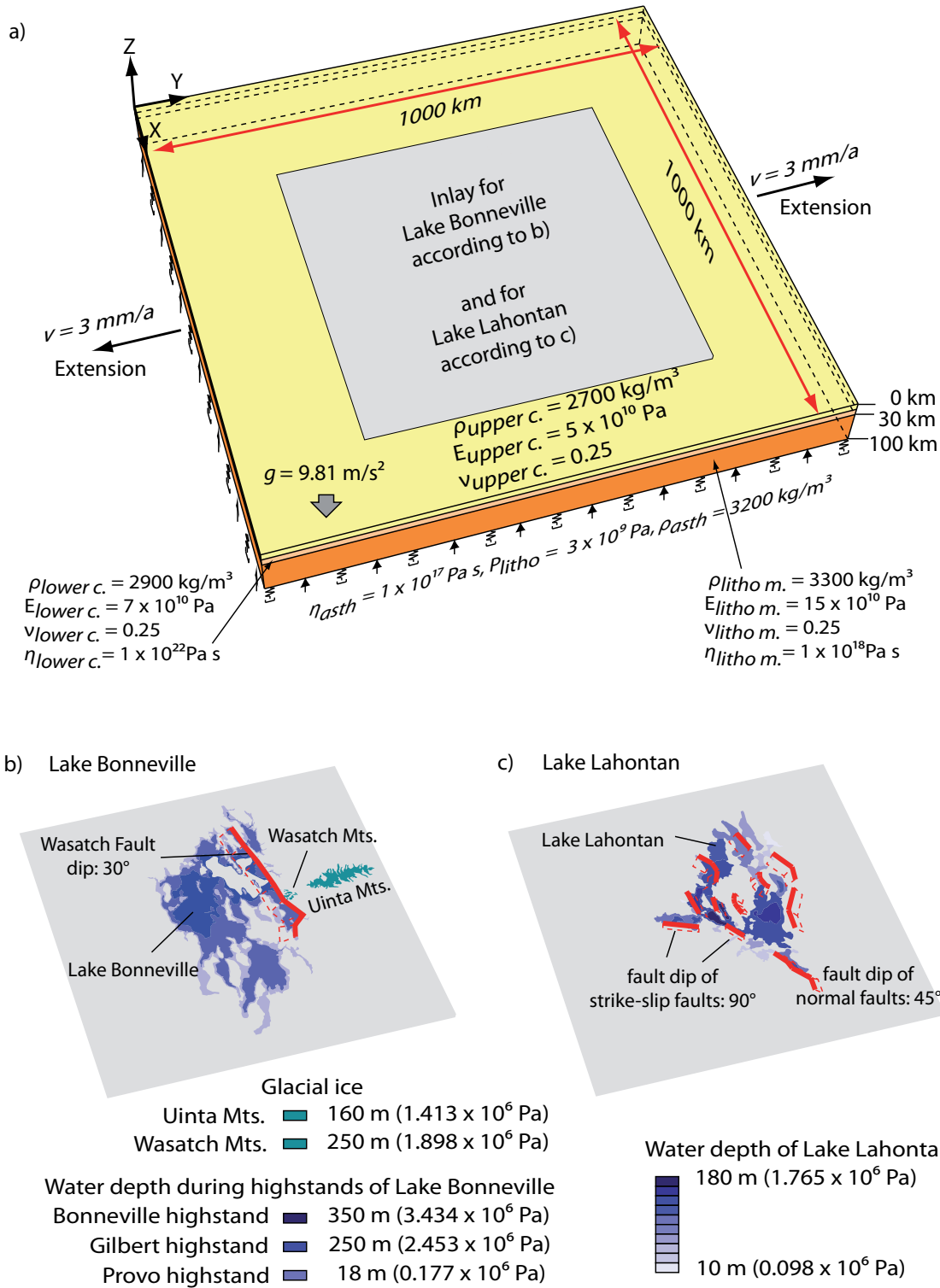


**Fig. 51:** a) Setup of the Lake Bonneville and Lake Lahontan model lithosphere. The rheological parameters are density ( $\rho$ ), elastic modulus ( $E$ ), Poisson ratio ( $\nu$ ), viscosity ( $\eta$ ), acceleration due to gravity ( $g$ ), surface load ( $L$ ), velocity ( $v$ ) and lithostatic pressure ( $P_{litho}$ ). Isostasy is implemented by the boundary conditions at the bottom of the model, which is free to move in  $z$  direction. The sides of the model parallel to the  $xz$ -plane are fixed in  $y$ -direction. The model is extended by applying a velocity boundary condition to the sides in the  $y$ - $z$  plane. b) Geometry of Lake Bonneville and the Wasatch Fault as implemented in the Lake Bonneville model. The 370-km-long Wasatch Fault is situated in the center of the model cutting through the upper crust. The fault dips with 30°. The surface partitions used to simulate Lake Bonneville with respect to the bathymetry and the partitions used to simulate the glacial load of the Uinta- and Wasatch Mountains are marked by the blue areas. c) Geometry of Lake Lahontan and 11 faults as implemented in the Lake Lahontan model. The faults are located in the center of the model cutting through the upper crust. All faults apart from the two strike-slip faults (Pyramid Lake Fault and Honey Lake Fault) being vertical dip with 45°. The different surface partitions used to simulate Lake Lahontan with respect to the bathymetry are marked by the blue areas. The different shades of blue of the surface partitions in b) and c) stand for different pressures applied to the model surface.



surface height for the partitions representing shallow portions of the lake. For the Lake Lahontan model, the loading function has been designed after Bills et al. (2007). In contrast to the Lake Bonneville model, the loading function used in this experiment is kept simple, starting with 20 ka of loading followed by 6 ka of unloading and 9 ka without load. Here the loading function controls the pressure applied to all surface partitions representing Lake Lahontan (Fig. 51c). The model time in the reference and parameter study starts with the onset of loading. In the Lake Bonneville and Lake Lahontan model, the model time is always referred to as time before present to make it easier to compare the results the paleoseismological record.

### ***Lake Bonneville, model and nature***

By extending the model lithosphere with a rate of 6 mm/a, the Wasatch Fault in the Bonneville model prior to loading reaches a maximum slip rate of 0.7 mm/a in the center of the Weber Segment. This slip rate is intended to fit the long-term average vertical displacement rate of the Wasatch Fault of 0.3 mm/a as suggested for the last 250 ka by Friedrich et al. (2003) (Fig. 54b, c) derived from geologic and geodetic data from the Wasatch region. The results of the Lake Bonneville model show a decrease in the slip rate of the fault from 0.7 mm/a to 0.5 mm/a in the center of the Weber segment during the rise of Lake Bonneville to its highstand at 18.5 ka followed by a slip rate of 0.6 mm/a throughout the Bonneville highstand from 18.5 ka to 17.5 ka. The 100 m drop of the lake level during the Bonneville flood between 17.5 ka and 17.4 ka (Fig. 52) leads to a pronounced increase in the slip rate. The maximum slip rate during the Bonneville flood reaches values of up to 8.5 mm/a, which is ten times larger than the steady-state slip rate prior to loading. The second larger lake level drop between 16.7 ka and 13.8 ka leads to an increased slip rate of 1.8 mm/a. After the Bonneville flood, the slip rate does not drop beneath 0.8 mm/a, neither in the interval of the Provo highstand between 17.4 ka and 16.7 ka, nor in the interval between the onset of rise of Lake Gilbert at 13.8 ka until today.

Regarding the slip rate distribution on the fault it becomes obvious that the point of maximum slip rate falls into the center of the Weber Segment of the Wasatch Fault prior to loading. During the intervals of Bonneville rise (33.4 ka – 18.5 ka) and the Bonneville highstand (18.5 ka – 17.5 ka) this point shifts southwards up to the northern Provo Segment and later back to the southern border of the Weber segment. In contrast, during the Bonneville flood (17.5 ka – 17.4 ka), the Provo highstand (17.4 ka – 16.7 ka), the Provo regression (16.7 ka – 13.8 ka), and for the final interval until today, the point of maximum slip rate shifts towards the northern tip of the fault, reaching the Brigham City segment during the Bonneville flood and afterwards the northern part of the Weber segment. The slip histories in Figure 53 show that the increase in the slip rate of the fault happens coevally with the drop of the lake level. This becomes clear by looking at the slip rate evolution of the four segments north of the Provo segment of the Wasatch Fault (Fig. 53c, d, e, f).

The results of the Lake Bonneville model show an increase of the slip rate as a response of the slip behavior of the Wasatch Fault to the lake regression. Friedrich et al. (2003) report an increase in the integrated vertical displacement rates over the last 15 ka. The integrated vertical

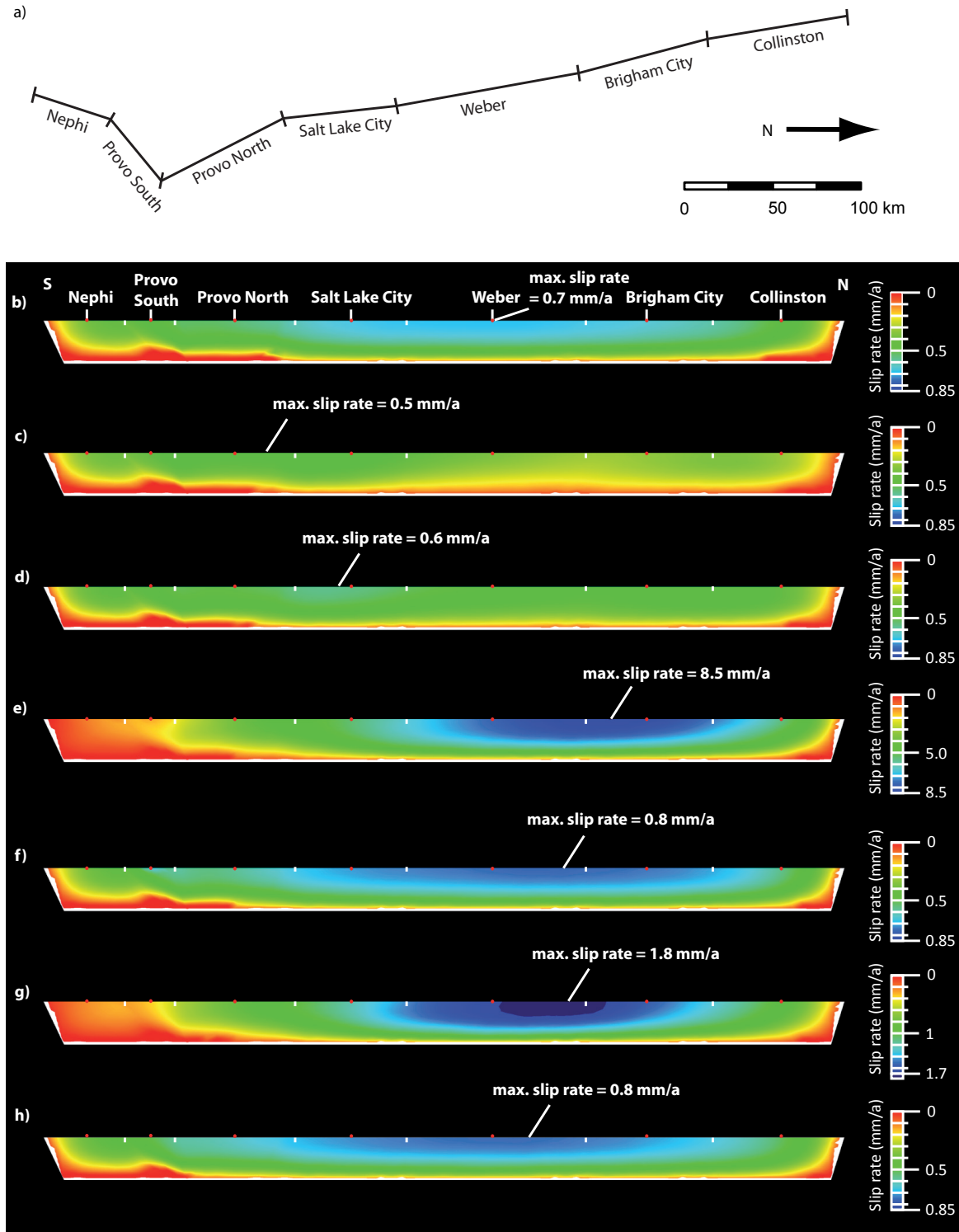


**Fig. 52:** Contour plots of the slip rate distribution on the Wasatch Fault (orientation shown in a)) b) prior to loading, during c) the interval of Lake Bonneville rise from 33.4 ka BP to 18.5 ka BP, d) during the Bonneville highstand between 18.5 ka BP and 17.5 ka BP, e) during the Bonneville flood ranging from 17.5 ka BP to 17.4 ka BP, f) during the Provo highstand between 17.4 ka BP and 16.7 ka BP, g) in the interval of lake level after the Provo highstand to the onset of the rise to the Gilbert highstand between 16.7 ka BP and 13.8 ka BP, and h) 13.8 ka BP until today.

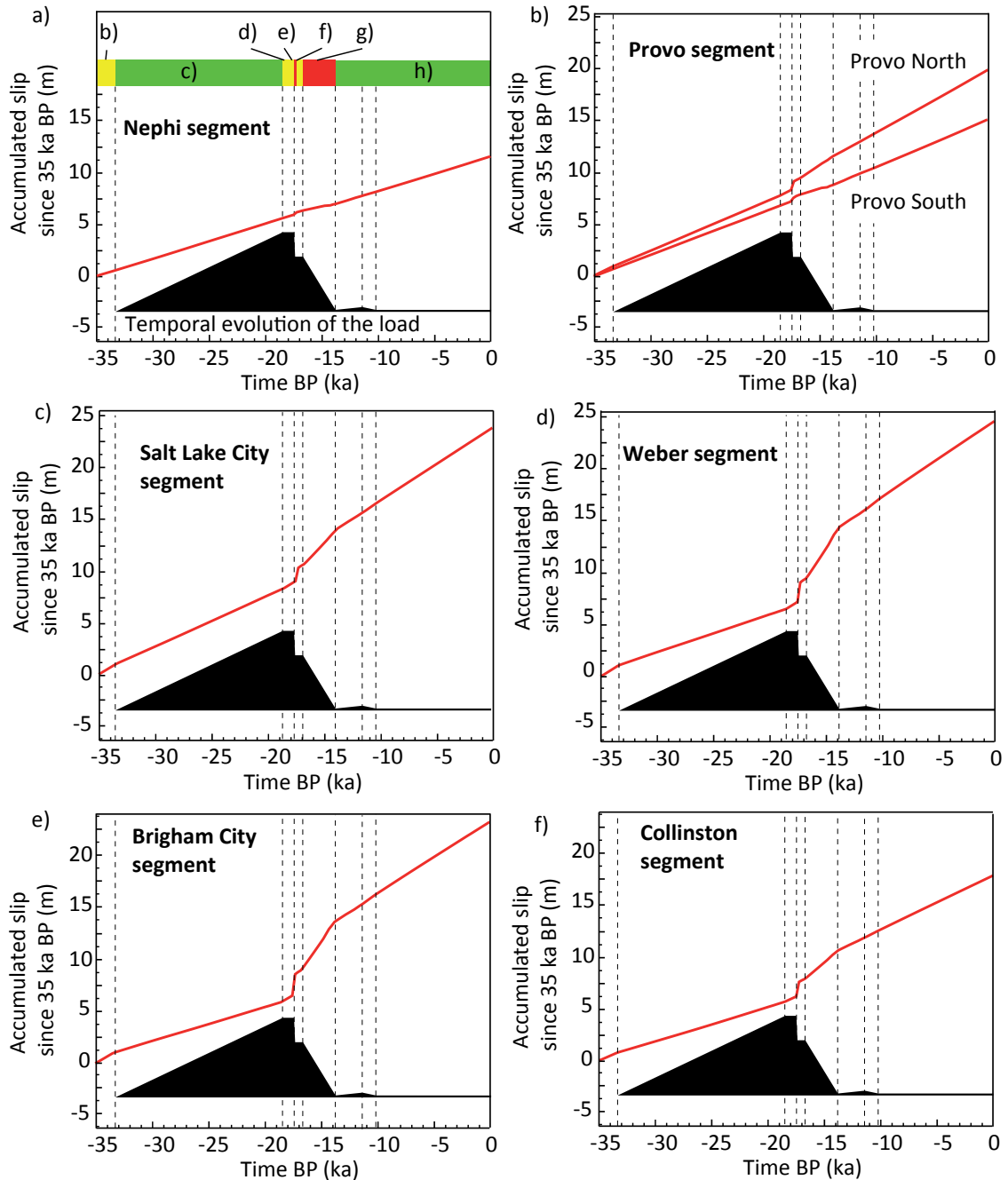


**Fig. 53:** Slip history plots of the six segments of the Wasatch Fault in the model for the last 35 ka. The slip history has been plotted for: a) the Nephi segment, b) the Provo Segment, c) the Salt Lake City segment, d) the Weber segment, e) the Brigham City segment, and f) the Collinston segment. The temporal evolution of the load, derived from a generalized version of the Lake Bonneville Lake level history after Oviatt et al. (1992), is indicated by the black polygon inset.

displacement rate over the last 15 ka has been estimated to be 1 mm/a or larger while the long-term vertical displacement rate for the last 250 ka gives an average of 0.3 mm/a (Friedrich et al., 2003) (Fig. 54b, c). A fault dip of  $30^\circ$  as used for the Wasatch Fault in the model, gives a slip rate of about 2 mm/a for the last 15 ka and 0.6 mm/a over the last 250 ka. While the geologic and geodetic data of Friedrich et al. (2003) show an ongoing increase of the slip rate towards today, the model results of the Lake Bonneville model show a peak in the slip rate, starting with the Bonneville flood at 17.5 ka, continuing to the onset of Lake Gilbert rise at 13.8 ka, and an increased slip rate of 0.8 mm/a compared to 0.7 mm/a prior to loading during the last 13.8 ka. Paleoseismologic data

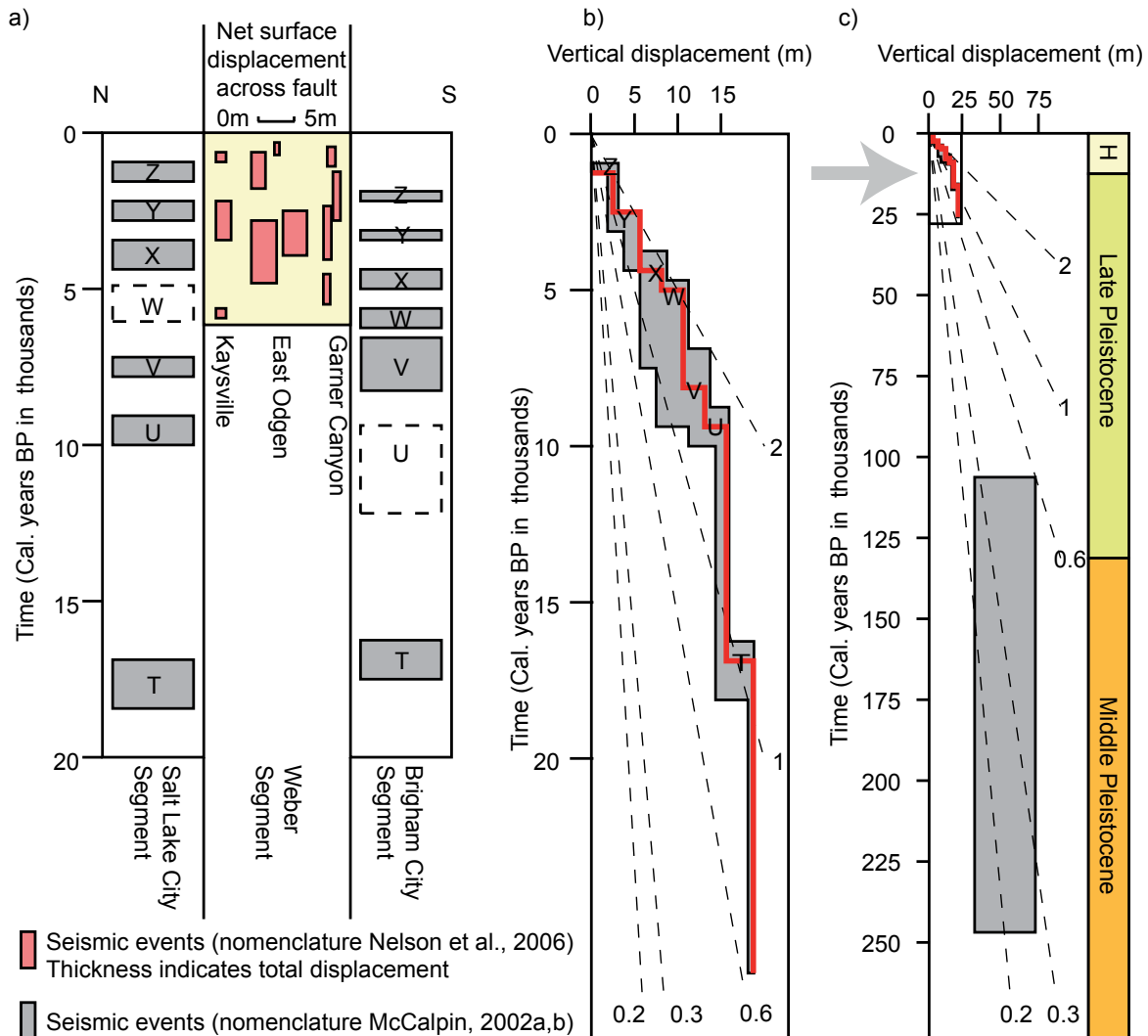


**Fig. 54:** Paleoseismological record of the Wasatch Fault compiled from McCalpin (2002a, 2002b), Nelson et al. (2006) and Friedrich et al. (2003) showing a) the earthquake history of the Salt Lake City, Weber and Brigham City segments of the Wasatch Fault, b) the vertical displacement for the Wasatch Fault Zone for the last 25 ka BP and c) for the last 250 ka BP (after Friedrich et al., 2003).

by McCalpin (2002a, 2002b) and Nelson et al. (2006) show an increasing number of seismic events for the Salt Lake City, the Weber and the Brigham City segment of the Wasatch Fault during the last 10 ka, as compiled in Figure 54a. The paleoseismologic datasets are consistent with the results of the lake Bonneville model, as both report a higher seismicity on the fault during the last 20 ka - 25 ka. The data by McCalpin (2002a, 2002b) shows two large seismic events occurring coevally on the Salt Lake City and on the Brigham City segment of the fault at about 17 ka. These events fall together with the Bonneville flood event. The model results indicate that these events may be a consequence of the lake level drop of Lake Bonneville and the resulting change of the principal stresses.

#### **Lake Lahontan, model and nature**

Regarding the results of the Lake Lahontan model, a similar slip rate evolution as in the models of the parameter study and the Lake Bonneville model can be seen. The slip rate in the center of the faults, prior to loading reaches values between minimum 0.23 mm/a (Fig. 55h) on the Bonham

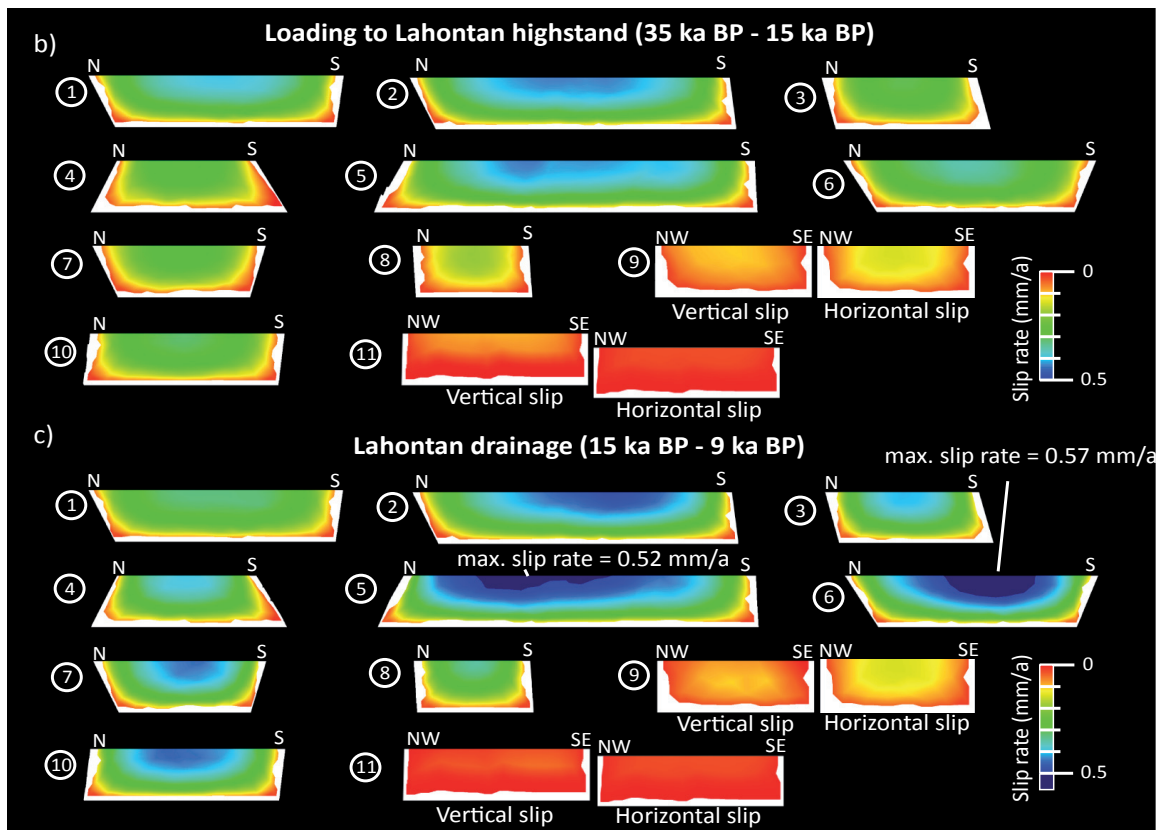
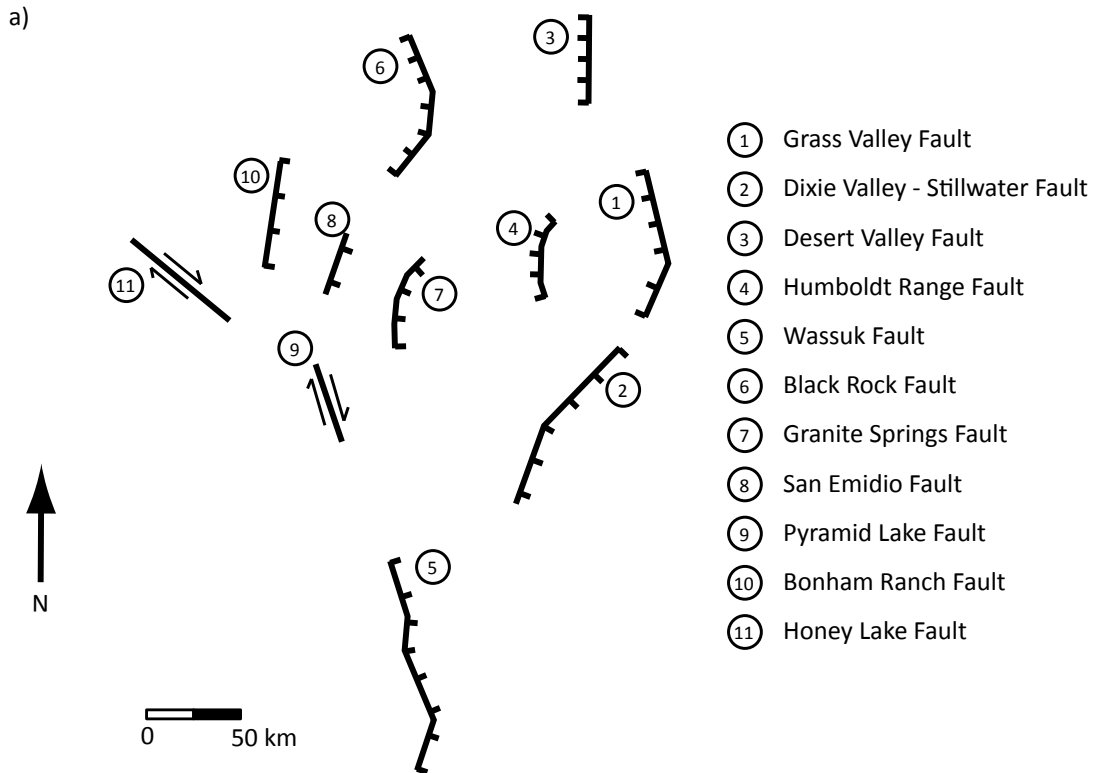


**Fig. 55:** Contour plots of the slip rate distribution on the modeled faults of the Lake Lahontan region (location shown in a)) during b) the interval of Lake Lahontan rise from 35 ka BP to 15 ka BP, c) during the drainage of Lake Lahontan between 15 ka BP and 9 ka BP. Note that the point of maximum slip jumps from the center of the Dixie Valley-Stillwater Fault and the Wassuk Fault during lake level rise to the Black Rock Fault during lake regression.

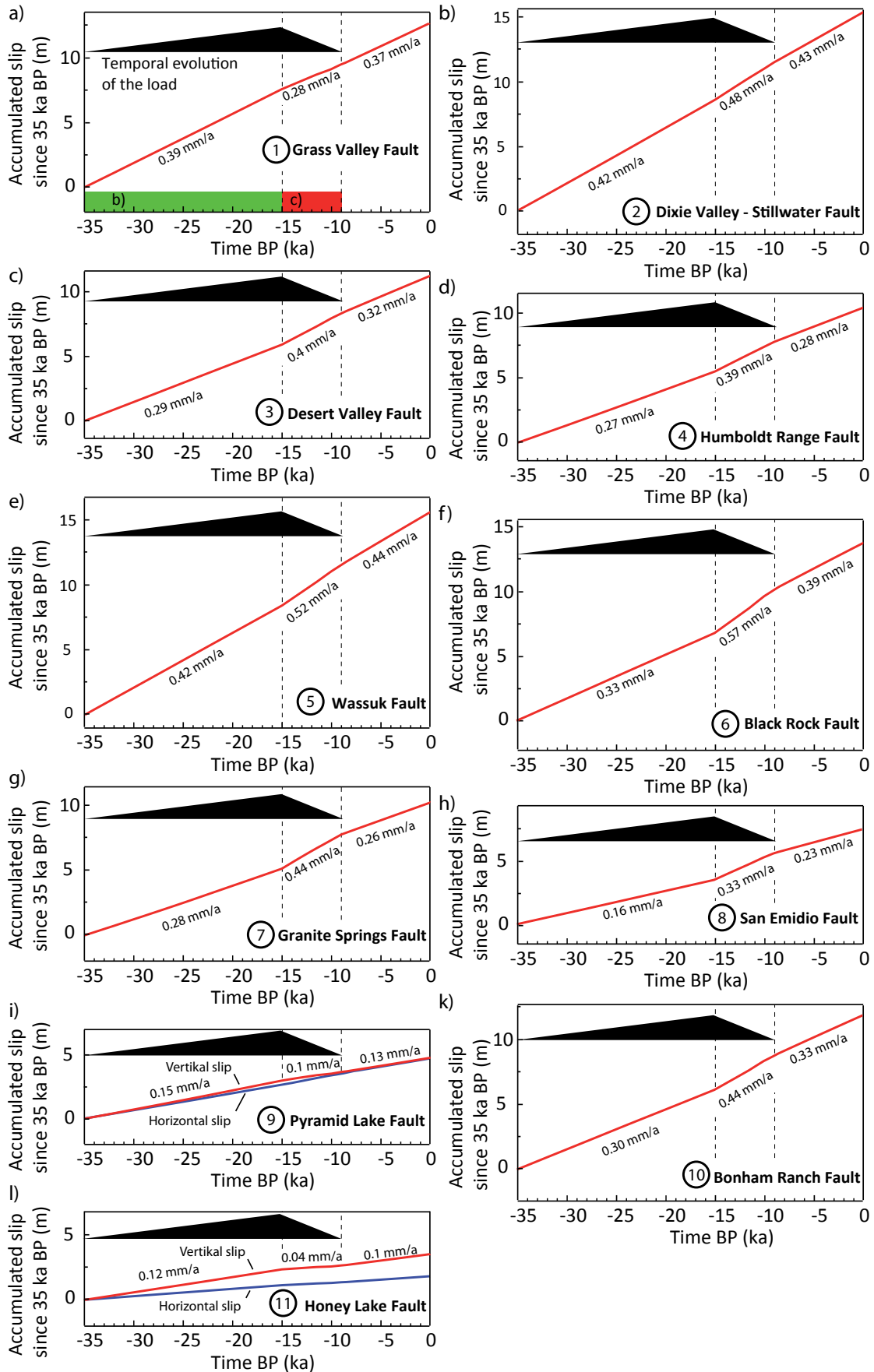


**Fig. 56:** Slip history plots of the eleven faults of the Lake Lahontan model for the last 35 ka. The slip history has been plotted for: a) the Grass Valley Fault, b) the Dixie Valley-Stillwater Fault, c) the Desert Valley Fault, d) the Humboldt Range Fault, e) the Wassuk Fault, f) the Black Rock Fault, g) the Granite Springs Fault, h) the San Emidio Fault, i) the Pyramid Lake Fault, k) the Bonham Ranch Fault, and l) the Honey Lake Fault. The temporal evolution of the load, derived from the Lake Lahontan Lake level history after Bills et al. (2007), is indicated by the black polygon inset.

Ranch Fault and maximum 0.43 mm/a (Fig. 55b) on the Dixie Valley fault. In general, loading leads to a decrease of the slip rate on the faults, ranging from a 5% drop in the slip rate on the Humboldt Fault and Wassuk Fault (Fig. 56) up to a 30% drop of the slip rate of the San Emidio Fault (Fig. 51). The regression of Lake Lahontan over 6 ka instead leads to an increase of the slip rate on most faults. The slip rates reach values that are 1.23 times (Wassuk Fault, Fig. 56) to 2.06 times (San Emidio Fault, Fig. 56) higher than the decelerated slip rates during loading. The highest slip rates during unloading are measured in the center of the Black Rock Fault (0.57 mm/a) and also in the center of the Wassuk Fault (0.52 mm/a) (Fig. 56). In contrast to the slip behavior of all other faults, the Grass Valley Fault shows an increase of the slip rate during the rise of Lake Lahontan while the decline of the Lake leads to a decrease of the slip rate, compared to the pre-loading slip rate. A look at the map (Fig. 47) reveals that the Grass Valley Fault dipping to the West offsets about 25 km to 40 km from the eastern Lake Lahontan coastline during maximum highstand, and thus is located at the outer border of the lithospheric flexure caused by Lake Lahontan water mass. In contrast to the Grass Valley Fault, the Dixie Valley-Stillwater Fault, also located East of Lake Lahontan, but dipping to the East, shows the expected deceleration-acceleration-pattern of the slip rate during loading and unloading. The difference between the decelerated slip rate of 0.42 mm/a during loading and the accelerated slip rate of 0.48 mm/a during unloading is rather small compared to faults situated in the center of Lake Lahontan, like the Granite Springs, the San Emidio, or the Black Rock Fault (Fig. 55). The way that the faults are affected by lake level changes of Lake Lahontan depends on the location of the fault relative to the lake load. As the plots in Figure 55 show, the faults experiencing the largest difference in the slip rate between loading and unloading are located at the deepest parts of Lake Lahontan with water load on the hanging - and footwall simultaneously. The Granite Springs Fault is located in the center of the ring shaped lake load and also of the loading-induced flexure. Faults situated along the coastline of Lake Lahontan, with either the hanging- or foot wall covered by the lake like the Bonham, or the Wassuk Fault, are less affected by a change of the lake size and volume.

#### 4.4.2 Thrust faults

The model results from the thrust fault experiments predict ceased to low seismicity during glaciation and a phase of high seismicity during deglaciation. Reverse faults of the length of up to 150 km, having an offset of about 10 - 15 m are described for Scandinavia, each having formed during one single  $M_w \approx 8$  event shortly after the Last Glacial Maximum (Mörner, 1995; Arvidson, 1996, Mörner, 2005). Two of the most prominent Scandinavian postglacial faults are the 150-km-long Pärve Fault in northern Sweden (Lundtquist and Lagerbäck, 1976, Mörner, 2005) and the 80-km-long Stuoragurra Fault in Finnmark County (Dehls et al., 2000). By compiling the earthquake record for Scandinavia, Mörner (2005) identifies a clear maximum in the number of seismic events between 9 ka to 11 ka BP having a magnitude of  $M_w \approx 5$  up to  $M_w \approx 8$ . This phase of high seismicity falls together with the deglaciation of Scandinavia after the Last Glacial Maximum. Although the load used in the parameter study is not comparable to the glacial load on the Scandinavian shield

during the Last Glacial Maximum, the model results support the interpretation that the postglacial faults formed owing to deglaciation of the region.

Even in regions glaciated today like Alaska, a close correlation between ice mass fluctuation in human time scales of 10 a to 100 a and changes in the seismicity has been described (Sauber et al., 2000; Sauber and Molnia, 2004). The ice mass fluctuation between 1995 and 2000 during which the Bering and Malaspina glaciers in south central Alaska lost up to 5 m/a in thickness (Sauber and Molnia, 2004). Sauber and Molnia (2004) recorded, by means of GPS measurements, vertical uplift rates of up to 50 mm/a relative to stable North America and observed an increase in the background seismicity of  $M_L \geq 2.5$  during ice thinning and a decrease of seismicity during ice thickening. These observations are consistent with the results of the thrust fault parameter study which strongly support a direct correlation of climate induced ice mass changes even in the dimension of a single glacier and the seismicity of neighboring faults. Sauber and Molnia (2004) also see a direct connection of the overall loss of hundreds of meters of ice above the plate boundary under Icy Bay between 1899 and 1979 and the occurrence of the second of two major earthquakes during the last century in that region. Prior to the 1979 St. Elias earthquake ( $M_S \approx 7.2$ ) the plate interface beneath Icy Bay was locked, accumulating tectonic strain. Sauber and Molnia (2004) propose that the ice loss after the 1899 Yakataga and Yakuta earthquake ( $M_w \approx 8.1, 8.1$ ) and the 1979 St. Elias earthquake ( $M_S \approx 7.2$ ) lead to prominent changes in the crustal stress field and promoted the second earthquake and subsequent aftershocks. The behavior of the thrust faults in the parameter study shows analogies to this slip behavior. During glaciation, slip on the model fault ceases, leading to seismic quiescence. By the onset of deglaciation, the stress field is altered in such way, that the differential stress dramatically increases, leading to the reactivation of the fault and to highly increased seismicity on the fault.

#### 4.4.3 Strike-slip faults

The Dead Sea Transform separating the Arabia plate from the Sinai plate is a sinistral strike-slip fault system. This fault system is characterized by several pull-apart basins, one of the most prominent ones being the Dead Sea basin that following the Jordan Valley to the South. Today's lake level of the Dead Sea is at about 415 m below sea level, making this the deepest depression in the world. During the Pleistocene the Jordan Valley as also the Dead Sea valley were covered by the precursor of the Dead Sea, being Lake Lisan. This Pleistocene lake existed between 70 ka to 15 ka BP (Bartov et al., 2002) reaching lake levels of 165 m below sea level around 25 ka BP. Like Lake Lahontan and Lake Bonneville, the Dead Sea experienced a massive loss of water volume during the last 20 ka to 25 ka with a total lake level drop of 250 m (Bartov et al., 2002, Bookman et al., 2004). The results of experiment made for strike-slip faults in the parameter study predict a decrease of seismicity during lake level rise and an increased seismicity for phases of lake regression. A 48-ka-long slip rate history for the Jordan Valley segment of the Dead Sea Fault by Ferry et al. (2007) shows an increase in seismicity for the last 10 ka with slip rates of maximum 11 mm/a between 10 ka to 7 ka BP, which is twice as fast as the long-term slip rate of 4.9 mm/a reconstructed for



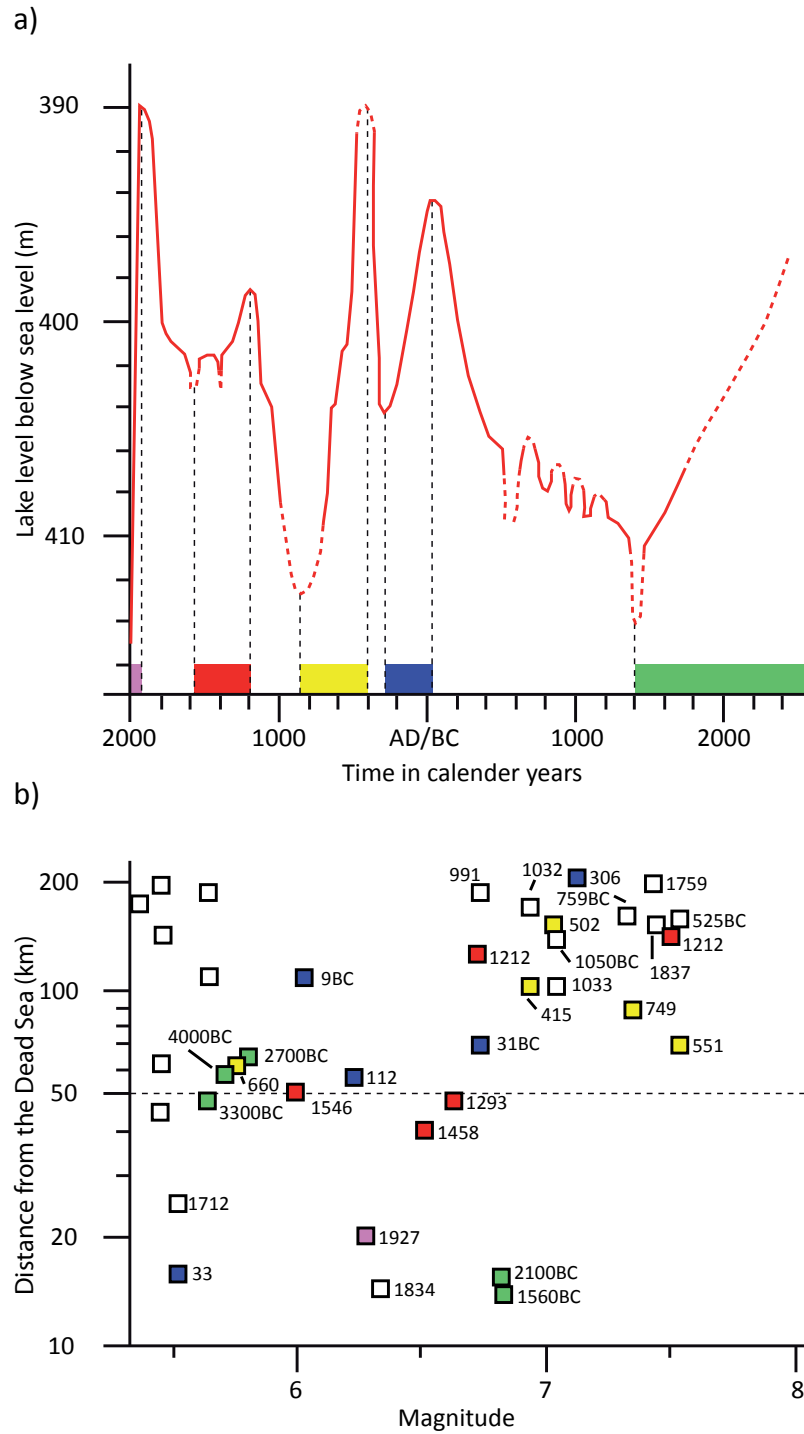


**Fig. 57:** a) Lake level curve of the Dead Sea during the past 4 ka (modified after Bookman et al., 2004). b) All available magnitudes of historical earthquakes for a distance of up to 200 km around the Dead Sea on a logarithmic scale. Undated earthquakes are marked by gray squares, all other earthquakes are color coded according to the colored bars in a) (after Migowski et al., 2004).

the last 48 ka. Compared to the results of the parameter study, this increase in seismicity may have been a consequence of the lake level regression. The lake-level curve published by Bookman et al. (2004) for Lake Lisan covers the lake level history of the last 4.5 ka, showing four major intervals of lake regression, the first at the beginning of the lake level history, lowering the lake level by >10 m and lasting until 3.4 ka before present, the second one from 2 ka to 1.8 ka leading to 8 m of lake level drop, the third one between 1.5 ka and 1.2 ka lowering the lake level about 8 m, and the last one starting at 0.2 ka and lasting until today with up to now 25 m of regression (Fig. 57a). These phases were interrupted by intervals of transgression. The earthquake record compiled by Migowski et al. (2004) for the last 6 ka, sorted by distance from the Dead Sea, reveal that most earthquakes registered in this record within a radius of 50 km around the Dead Sea basin coincide with an interval of lake regression (Fig. 57b). The results of the parameter study imply that all of these earthquakes may have been promoted by unloading of the lithosphere due to regression of Lake Lisan. Working on the southern portion of the San Andreas Fault and on the San Jacinto Fault, Luttrell et al. (2007) show by analyzing the effect of Coulomb stress perturbation on local faults due to changes in the lake level of ancient Lake Cahuille, that four of the past five ruptures on the southern San Andreas fault have occurred near a time of substantial lake level change. Luttrell et al. (2007) also state that the recurrence interval of Lake Cahuille, which covered large portions of the southern San Andreas Fault, is similar to the recurrence interval of ruptures on the southern San Andreas Fault and the San Jacinto fault.

## 5 Conclusions and outlook

The present study investigates the behavior of faults subjected to changes in the load to the Earth's surface using three dimensional finite element models. These models reveal the influence of transient vertical stress changes caused by a temporal variation of a surface load as well as horizontal stress changes caused by the loading-induced flexure on the slip behavior of active faults. The results of the parameter study imply that:

- Changes in the load on the Earth's surface strongly affect the slip behavior of a thrust fault, a normal fault and a strike-slip fault.
- The general reaction of faults to an increasing load on the surface is characterized by a decrease in seismicity. The removal of the load is accompanied by a pronounced increase in seismicity.
- The magnitude of the decrease in seismicity during loading and the increase during unloading strongly depends on the amount of the load applied to the Earth's surface.
- It is not the load itself that affects the seismicity but the change in load over time that leads to transient changes in the stress field of the lithosphere and to short-term variations in the slip rate on the faults as a constant load leads to a readjustment of the stress state similar to the pre-loading state.
- It is mainly the influence of the horizontal stresses in the model that affects the slip behavior of a fault during loading and unloading.

The models applied to natural faults as the Wasatch Fault or a fault array in the western Basin and Range Province in the area of ancient Lake Lahontan show that the paleoseismological record collected at these locations agrees well with the result observed in the models. Regarding the experiments of the parameter study for the thrust fault and normal fault models show, when compared to the results of field studies of thrust faults in Alaska and the Dead Sea Transform fault, that changes in seismicity may have been caused by fluctuations in the surface load.

The short-term changes in seismicity as observed in the paleoseismologic record from the Basin and Range Province can be explained by the regression of large pluvial lakes like Lake Bonneville and Lake Lahontan. Lake level data from the Dead Sea (Bartov et al., 2002, Bookman et al., 2004) predict an ongoing regression of the Dead Sea for the future. The comparison of the timing of local earthquakes in the vicinity of the Dead Sea (Migowski et al., 2004) with the lake level curve of the Dead Sea, reveals a connection between lake regression and the promotion of earthquakes. As a consequence, an ongoing lake level drop of the Dead Sea might promote further earthquakes in that region.

The increased seismicity in the South-East of Alaska is the consequence of ice mass fluctuations of glaciers as assumed by Sauber and Molnia (2004). Johnson et al. (2008) reconstructed the long-term ice thinning history of the West Antarctic Ice Sheet by the means of exposure ages derived from cosmogenic nuclides from the Amundsen Sea Embayment. They propose an average ice thinning rate of  $3.8 \pm 0.3$  cm/a over the last 4.7 ka and compare them to thinning rates gained

from satellite altimetry of 1.6 m/a for the Pine Island Glacier (West Antarctic Ice Sheet). This increase in the thinning rates of the West Antarctic Ice Sheet might promote local seismicity of the type observed by Sauber and Molnia (2004). The thinning of the Antarctic inland ice might even lead to large scale postglacial fault scarps as known from Scandinavia (Dehls et al., 2000, Lundqvist and Lagerbäck, 1976). In analogy to the recent accelerated thinning of the West Antarctic Ice Sheet, similar ice thinning scenarios have been reported by Krabill (2004) for the Greenland inland ice and by Keller et al. (2007) for parts of Patagonia due to climate change. As proposed by the model results of this study, the seismicity in these regions might be affected in the future as a consequence of the melting of glacial ice due to climate change.

## References

- Adams, J., 1989. Postglacial faulting in eastern Canada: nature and origin and seismic hazard implications. *Tectonophysics*, 163, 323-331.
- Adams, J., 1996. Paleoseismology in Canada: A dozen years of progress. *J. Geophys. Res.*, 101, 6193-6207.
- Adams, J. and P.W. Basham, 1989. The seismicity and seismotectonics of Canada east of the Cordillera. *Geosci. Canada*, 16, 3-16.
- Adams, K.D. and S.G. Wesnousky, 1998. Shoreline processes and the age of Lake Lahontan highstand in the Jessup embayment. *Bull. Geol. Soc. Am.*, 110, 1318-1332.
- Adams, K.D. and S.G. Wesnousky, and B.G. Bills, 1999. Isostatic rebound, active faulting, and potential geomorphic effects in the Lake Lahontan basin, Nevada and California. *Bull. Geol. Soc. Am.*, 111, 1739-1756.
- Al-Zoubi, A. and U. ten Brink, 2002. Lower crustal flow and the role of shear in basin subsidence: an example from the Dead Sea basin. *Earth Planet. Sci. Lett.*, 199, 67-79.
- Amelung F. and J. W. Bell, 2003. Interferometric synthetic aperture radar observations of the 1994 Double Spring Flat, Nevada, earthquake (M5.9): Main shock accompanied by triggered slip on a conjugate fault. *J. Geophys. Res.*, 108, 2433, doi:10.1029/2002JB001953.
- Armstrong, P.A., A.R. Taylor and T.A. Ehlers, 2004. Is the Wasatch fault footwall (Utah, United States) segmented over million-year time scales?. *Geology*, 32, 5, 385–388, doi: 10.1130/G20421.1.
- Arvidson, R., 1996. Fennoscandian earthquakes: whole crustal rupturing related to postglacial rebound. *Science*, 274, 744-746.
- Bartov, Y., M. Stein, Y. Enzel, A. Agnon and Z.E. Reches, 2002. Lake Levels and Sequence Stratigraphy of Lake Lisan, the Late Pleistocene Precursor of the Dead Sea. *Quat. Res.*, 57, 9–21
- Bartsch, M., 2006. Rekonstruktion des Paläogletschervolumens während des letzten glazialen Maximums in den Wasatch Mountains, Utah (USA). BSc-thesis, Westfälische Wilhelms-Universität Münster.
- Beaumont, C., P. Fullsack and J. Hamilton, 1994. Styles of crustal deformation in compressional orogens caused by the subduction of the underlying lithosphere. *Tectonophysics*, 232, 119-132.
- Bennett, R.A., J.L. Davis and B.P. Wernicke, 1999. Present-day pattern of Cordilleran deformation in the western United States. *Geology*, 27, 371–374.
- Benson, L.V., D.R. Currey, Y. Lao and S.W. Hostetler, 1992. Lake-size variations in the Lahontan and Bonneville basins between 13,000 and 9,000 (super 14) C yr B. P.. *Palaeogeogr., Palaeoclimatol., Palaeoecol.*, 95 (1-2), 19-23.

- Benson, L.V., M. Kashgarian and M. Rubin, 1995. Carbonat deposition, Pyramid Lake subbasin, Nevada. 2. Lake levels and polar-jet stream positions reconstructed from radiocarbon ages and elevations of carbonates (tufas) deposited in the Lahontan basin. *Palaeogeogr., Palaeoclimatol., Palaeoecol.*, 117, 1-30.
- Benson, L.V., J.P. Smoot, M. Kashgarian, W.M.A. Sarna and J.W. Burdett, 1997. Radiocarbon ages and environments of deposition of the Wono and Trego Hot Springs tephra layers in the Pyramid Lake subbasin, Nevada. *Quat. Res.*, 47, 251-260.
- Benson, L.V. and R.A. Thomson, 1987. Lake level variation in the Lahontan basin for the past 50,000 years. *Quat. Res.*, 28, 69-85.
- Benson, L.V., L.D. White and Rye R., 1996. Carbonat deposition, Pyramid Lake subbasin, Nevada. Comparison of stable isotope values of carbonate deposits (tufas) and the Lahontan lake level record. *Palaeogeogr., Palaeoclimatol., Palaeoecol.*, 119, 201-213.
- Bills, B.G., K.D. Adams and S.G. Wesnousky, 2007. Viscosity structure of the crust and upper mantle in western Nevada from isostatic rebound patterns of the late Pleistocene Lake Lahontan high shorelines. *J. Geophys. Res.*, 112, B06405, doi:10.1029/2005JB003941.
- Bills, B.G., D.R. Currey and G.A. Marshall, 1994. Viscosity estimates of the crust and upper-mantle from patterns of shoreline deformation in the Eastern Great-Basin. *J. Geophys. Res.*, 99, 22,059-22,086.
- Bills B.G. and G.M. May, 1987. Lake Bonneville: Constraints on lithospheric thickness and upper mantle viscosity from isostatic warping of Bonneville, Provo, and Gilbert stage shorelines. *J. Geophys. Res.*, 92, 11,493-11,508.
- Bookman, R., Y. Enzel, A. Agnon and M. Stein, 2004. Late Holocene lake levels of the Dead Sea. *Geol. Soc. Amer. Bull.*, 116, 555-571.
- Brace, W.F. and D. L. Kohlstedt, 1980. Limits on lithostatic stress imposed by laboratory experiments. *J. Geophys. Res.*, 85, 6248-6252.
- Brown, E.T., D.L. Bourles, B.C. Burchfiel, D. Quidong, L. Jun, P. Molnar, G.M. Raisbeck and F. Yiou, 1998. Estimation of slip rates in the southern Tien Shan using cosmic ray exposure dates of abandoned alluvial fans. *Geol. Soc. Am. Bull.*, 110, 377-386.
- Burg, J.-P. and Y.Y. Podladchikov, 2000. From buckling to asymmetric folding of the continental lithosphere: numerical modelling and application to the Himalaya syntaxes, From: *Tectonics of the Nanga Parbat Syntaxis and the Western Himalaya* (eds. M.A. Khan, P.J. Treloar, M.P. Searle, M.Q. Jan). *Geol. Soc. Spec. Publ.*, 170, 219-236.
- Burov, E.B., and A.B. Watts, 2006. The long-term strength of the continental lithosphere: „jelly sandwich“ or „crème brûlée“?. *GSA Today*, 16, 1, 4-10.
- Burr, T.N. and D.R. Currey, 1988. The Stockton Bar, edited by M.N. Machette, In the *Footsteps of G.K. Gilbert-Lake Bonneville and Neotectonics of the Eastern Basin and Range Province*. *Utah Geol. Miner. Surv. Misc. Publ.*, 88-1, 66-73.

- Caskey, J. and S.G. Wesnousky, 1997. Static Stress Changes and Earthquake Triggering during the 1954 Fairview Peak and Dixie Valley Earthquakes, Central Nevada. *Bull. Seism. Soc. America*, 87, 51-527.
- Chen, W-P. and P. Molnar, 1983. Focal depths of intracontinental and intraplate earthquakes and their implications for the thermal and mechanical properties of the lithosphere. *J. Geophys. Res.*, 88, 4183–4214.
- Cowie, P.A., 1998. A healing-reloading feedback control on the growth rate of seismogenic faults. *J. Struct. Geol.*, 20, 1075-1087.
- Cowie, P.A., and G.P. Roberts, 2001. Constraining slip rates and spacings for active normal faults. *J. Geophys. Res.*, 23, 1902-1915.
- Currey, D.R., 1982. Lake Bonneville: Selected features of relevance to neotectonic analysis. U.S. Geol. Surv. Open File Rep., 82-1070, 31 p.
- Davis, J.O., 1983. Level of Lake Lahontan during deposition of the Trego Hot Spring Tephra about 23,400 years ago. *Quat. Res.*, 19, 312-324.
- Davis, J.O., 1987. Introduction to the Pleistocene Geology of Northwestern Lake Lahontan, Nevada, 28pp.. Friends of the Pleistocene Pacific Cell fieldtrip guidebook, Reno, Nevada.
- Dehls J.F, O.Olesen, L.Olsen and L.H. Blikra, 2000. Neotectonic faulting in northern Norway; the Stouragurra and Nordmannvikdalen postglacial faults. *Quat. Sci. Rev.*, 19, 1447-1460.
- Dixon, T.H., M. Miller, F. Farina, C.M. Wang and D. Johnson, 2000. Present-day motion of the Sierra Nevada block and some tectonic implications for the Basin and Range province, North American Cordillera. *Tectonics*, 19, 1-24.
- Dohrenwend, J.C., B.A. Schell, C.M. Menges, BC. Moring and M.A. McKittrick, 1996. Reconnaissance photogeologic map of young (Quaternary and Tertiary) faults in Nevada, in Singer, D.A., ed., An analysis of Nevada's metal-bearing mineral resources. Nevada Bureau of Mines and Geology Open-File Report, 96-2.
- Ekman, M., 1989. Impacts of geodynamic phenomena on systems for height and gravity. *Bull. Geod.*, 63, 181-196.
- England, P. and D. McKenzie, 1982. A thin viscous sheet model for continental deformation, *Geophys. J. R. astr. Soc.*, 70, 295-321.
- Evans, D.M., 1966. The Denver area earthquakes and the Rocky Mountain Arsenal disposal well. *The Mountain Geologist*, 3, 1, 23-26.
- Ferry, M., M. Meghraoui, N.A. Karaki, M. Al-Taj, H. Amoush, S. Al-Dhaisat and M. Barjous, 2007. A 48-kyr-long slip rate history for the Jordan Valley segment of the Dead Sea Fault. *Earth and Planet. Sci. Lett.*, 260, 394–406.
- Friedrich, A., B.P. Wernicke, N.A. Niemi, R.A. Bennett and J.L. Davis, 2003. Comparison of geodetic and geologic data from the Wasatch region, Utah, and implications for the spectral character of Earth deformation at periods of 10 to 10 million years. *J. Geophys. Res.*, 108, 2199, doi:10.1029/2001JB000682.

- Gerya, T.V., D.A. Yuen and W.V. Maresch, 2004. Thermomechanical modelling of slab detachment. *Earth Planet. Sci. Lett.*, 226, 101-116.
- Gilbert, G. K., 1890. Lake Bonneville. U. S. Geological Survey Monograph, 1, 438 p.
- Gourmelen, N. and F. Amelung, 2005. Postseismic mantle relaxation in the Central Nevada Seismic Belt. *Science*, 310, 1473-1476.
- Gupta, H.K., 2002. A review of recent studies of triggered earthquakes by artificial water reservoirs with special emphasis on earthquakes in Koyna, India. *Earth-Science Reviews*, 58, 279–310
- Hampel, A. and R. Hetzel, 2006. Response of normal faults to glacial-interglacial fluctuations of ice and water masses on Earth's surface. *J. Geophys. Res.*, 111, B06406, doi:10.1029/2005JB004124.
- Hampel, A., R. Hetzel and A.L. Densmore, 2007. Postglacial slip rate increase on the Teton normal fault, northern Basin and Range Province, caused by melting of the Yellowstone ice cap and deglaciation of the Teton Range?. *Geology*, 35 (12), 1107–1110. doi:10.1130/G24093A.1.
- Hearn, E.H. and E.D. Humphreys, 1998. Kinematics of the southern Walker Lane belt and motion of the Sierra Nevada block. *J. of Geoph. Res.*, 103, 27033-27049.
- Hetzel, R. and A. Hampel, 2005. Slip rate variations on normal faults during glacial-interglacial changes in surface loads. *Nature*, 435, 81-84.
- Hetzel R., S. Niedermann, M. Tao, P.W. Kubik, S. Ivy-Ochs, B. Gao and M.R. Strecker, 2002. Low slip rates and long-term preservation of geomorphic features in Central Asia. *Nature*, 417, 428-432.
- Hibbitt, Karlsson, Sorenson, 2007. ABAQUS/Standard User's Manual, version 6.7. Pawtucket, R.I., USA.
- Hodgkinson, K.M., R.S. Stein and G.C.P King, 1996. The 1954 Rainbow Mountain-Fairview Peak-Dixie Valley earthquakes: a triggered normal faulting sequence. *J. Geophys. Res.*, 101, 25459-25471.
- Houseman, G. and P. England, 1986. Finite-strain calculations of continental deformation 1. Method and general results for convergent zones. *J. Geophys. Res.*, 91, 3651-3663.
- Iwata, T. and I. Nakanishi, 2004. Hastening of occurrences of earthquakes due to dynamic triggering: The observation at Matsushiro, central Japan. *J. Seismology*, doi: 10.1023/B:JOSE.0000021378.64563.c0.
- Jackson, J., 2002. Faulting, flow, and the strength of the continental lithosphere. *Int. Geol. Rev.*, 44, 39-61
- Johnson, J.S., M.J. Bently, K. Gohl, 2008. First exposure ages from the Amundsen Sea Embayment, West Antarctica: The Late Quaternary context for recent thinning of Pine Island, Smith, and Pope Glaciers. *Geology*, 36, 3, 223-226, doi: 10.1130/G24207A.1.
- Johnston, A.C., 1987. Suppression of earthquakes by large continental ice sheets. *Nature*, 330, 467-469.



- Johnston, A.C. , 1989. The effect of large ice sheets on earthquake genesis. In *Earthquakes at North-Atlantic Passive Margins: Neotectonics and Postglacial Rebound*. S. Gregersen and P. W. Basham, Eds. (Kluwer, Dordrecht, Netherlands, 1989), pp. 581-599.
- Johnston, P. and Wu, P. and Lambeck, K., 1998. Dependence of horizontal stress magnitude on load dimension in glacial rebound models. *Geophys. J. Int.*, 132, 41–60.
- Kaufmann, G. and F. Amelung, 2000. Reservoir-induced deformation and continental rheology in vicinity of Lake Mead, Nevada. *J. Geophys. Res.*, 105, 16,341-16358.
- Laabs, B.J.C. and E.C. Carson, 2005. Glacial Geology of the Southern Uinta Mountains, in Dehler, C.m., J.I. Pederson, D.a. Sprinkel, B.J. Kowallis, editors, *Uinta Mountains geology*. Utah Geol. Association Publ., 33, 235-253.
- Lagerbäck, R., 1992. Dating of Late Quaternary faulting in northern Sweden. *J. Geol. Soc. London*, 149, 285-291.
- Lagerbäck, R., 1979. Neotectonic structures in northern Sweden. *Geol. Fören. Stockh. Förh.*, 100, 271-278.
- Lin C.H. 2005. Seismicity increase after the construction of the world's tallest building: An active blind fault beneath the Taipei 101. *Geophys. Res. L.*, 32, L22313, doi:10.1029/2005GL024223.
- Lundquist, J., 1986. The Weichselian glaciation and deglaciation in Scandinavia. *Quat. Sci. Rev.*, 5, 269-292.
- Lundqvist, J., 2000. Palaeoseismicity and De Geer morains. *Quat. Int.* 68-71, 175–186.
- Lundqvist J. and R. Lagerbäck, 1976. The Pärve fault: a late-glacial fault in the Precambrian of Swedish Lapland. *Geol. Fören. Stockh. Förh.*, 98, 51-54.
- Lundquist, J. and V. Mejdahl, 1995. Luminescence dating of the deglaciation in northern Sweden. *Quat. Int.*, 28, 193-197.
- Luttrell, K., D. Sandwell, B. Smith-Konter, B. Bills and Y. Bock, 2007. Modulation of the earthquake cycle at the southern San Andreas fault by lake loading. *J. Geophys. Res.*, 112, B08411, doi:10.1029/2006JB004752.
- Keller, K., G. Casassa, A. Rivera, R. Forsberg, N. Gundestrup, 2007. Airborne laser altimetry Survey of Glaciar Tyndall, Patagonia. *Gl. Plan. Ch.*, 59, 101–109
- Krabill, W.,E. Hanna,P. Huybrechts,W. Abdalati,J. Cappelen,B. Csatho,E. Frederick,S. Manizade,C. Martin,J. Sonntag,R. Swift,R. Thomas and J. Yungel, 2004. Greenland Ice Sheet: Increased coastal thinning. *Geophys. Res. L.*, 31, L24402, doi:10.1029/2004GL021533.
- Machette, M.N., S.F. Personius, A.R. Nelson, D.P. Schwartz and W.R. Lund, 1991. The Wasatch fault zone, Utah – Segmentation and history of Holocene Earthquakes. *J. Struct. Geol.*, 13, 137-149.
- Marco, S., M. Stein, A. Agnon and H. Ron, 1996. Long-term earthquake clustering: A 50,000-year paleoseismic record in the Dead Sea Graben. *J. Geophys. Res.*, 101, 6179–6191, doi:10.1029/95JB01587.

- McCalpin, J. P., 2002a. Post-Bonneville Paleoearthquake Chronology of The Salt Lake City Segment, Wasatch Fault Zone, from the 1999 „Megatrench“ Site. Misc. Publ., 02-7, Utah Geol. Survey.
- McCalpin J. P., 2002b. Post-Provo Paleoearthquake Chronology of the Brigham City Segment, Wasatch Fault Zone, Utah. Misc. Publ., 02-9, Utah Geol. Survey.
- McCalpin, J.P.a and S.P. Nisenko, 1996. Holocene paleoseismicity, temporal clustering, and probabilities of future large ( $M > 7$ ) earthquakes on the Wasatch fault zone, Utah. *J. Geophys. Res.*, 101, 6233-6253.
- Maniatis G., CH. Lempp and H. Heinisch, 2003. 3D Monitoring of onshore active faults at the eastern end of the Gulf of Corinth (Greece). *J. Geodyn.*, 36, 95-102.
- Medvedev, S.E., 2002. Mechanics of viscous wedges: Modeling by analytical and numerical approaches. *J. Geophys. Res.*, 107, 10.1029/2001JB000145.
- Medvedev, S.E. and Y.Y. Podladchikov, 1999. New extended thin-sheet approximation for geodynamic applications - Model formulation. *Geophys. J. Int.*, 136, 567-585.
- Migowski, C., A. Agnon, R. Bookman, J.F.W. Negendank and M. Stein, 2004. Recurrence pattern of Holocene earthquakes along the Dead Sea transform revealed by varve-counting and radio-carbon dating of lacustrine sediments. *Earth and Planetary Sc. L.*, 222, 301– 314.
- Milne, G.A., J.L. Davis, J.X. Mitrovica, H.-G. Scherneck, J.M. Johansson, M. Vermeer and H. Koivula, 2001. Space-geodetic constraints on glacial isostatic adjustment in Fennoscandia. *Science*, 291, 2381-2385.
- Mörner, N.-A., 1978. Faulting, fracturing and seismic activity as a function of glacial-isostasy in Fennoscandia. *Geology*, 6, 41-45.
- Mörner, N.-A., 1980. The Fennoscandian uplift: geological data and their geodynamical implication. In: Mörner, N.-A. (Ed.), *Earth Rheology, Isostasy and Eustasy*. Wiley, Chichester, 251–284.
- Mörner, N.-A., 1995. Paleoseismicity - the Swedish case. *Quat. Int.*, 25, 75-79.
- Mörner, N.-A., 2004. Active faults and paleoseismicity in Fennoscandia, especially Sweden. Primary structures and secondary effects. *Tectonophysics*, 380, 139-157.
- Mörner, N.-A., 2005. An interpretation and catalogue of paleoseismicity in Sweden. *Tectonophysics*, 408, 265-307.
- Muir-Wood, R., 2000. Deglaciation Seismotectonics: a principal influence on intraplate seismogenesis at high latitudes. *Quat. Sci. Rev.*, 19, 1399-1411.
- Munroe, J.S., 2005. Glacial Geology of the Northern Uinta Mountains, in Dehler, C.m., J.I. Pederson, D.a. Sprinkel and B.J. Kowallis, editors, *Uinta Mountains geology*. Utah Geol. Association Publ., 33, 214-234.
- Nakiboglu S. M. and K. Lambeck, 1983. A reevaluation of the isostatic rebound of Lake Bonneville. *J. Geophys. Res.*, 88, 439-447.
- Nelson, A. R., M. Lowe, S. Personius, L. Bradley, S. L. Forman, R. Klauk and J. Garr, 2006. Holocene Earthquake History of the Northern Weber Segment of the Wasatch Fault Zone, Utah. Misc. Publ. 05-8, Utah Geological Survey.

- Nishimura, T. and W. Thatcher, 2003. Rheology of the lithosphere inferred from post seismic uplift following the 1959 Hebgen Lake earthquake. *J. Geophys. Res.*, 108, 2389, doi:10.1029/2002JB002191.
- Nocquet, J.-M., E. Calais and B. Parsons, 2005. Geodetic constraints on glacial isostatic adjustment in Europe. *Geophys. Res. Lett.*, 32, L06308, doi:10.1029/2004GL022174.
- Oviatt, C. G., D. R. Currey and D. Sack, 1992. Radiocarbon chronology of Lake Bonneville, Eastern Great Basin, USA. *Palaeogeogr. Palaeoclimatol. Palaeoecol.*, 99, 225–241.
- Reid, H.F., The California earthquake of April 18, 1906. The mechanics of the earthquake, In Report of the (California) State Earthquake Investigation Commission (Calif. State Earthquake Invest. Comm. Sacramento, vol. 2. Publ. 87, (1910) , 1-192.
- Roth, J.C., 2006. Digitale Rekonstruktion von Paläo-Gletschereisvolumen des letzten glazialen Maximums am Beispiel der Uinta Mountains, Utah (USA). Diploma-thesis, Westfälische Wilhelms-Universität Münster.
- Sauber, J., G. Plafker, B.F. Molnia and M.A. Bryant, 2000. Crustal deformation associated with glacial fluctuations in the eastern Chugach Mountains. Alaska, *J. Geophys. Res.*, 105, 8055-8077.
- Sauber, J. and B.F. Molnia, 2004. Glacier ice mass fluctuations and fault instability in tectonically active southern Alaska. *Global Planet. Change*, 42, 279-293.
- Scholz, C.H., 2002. The mechanics of earthquakes and faulting, 2nd edition. Cambridge Univ. Press., 471 p..
- Schwartz D.P., and K.J Coppersmith, 1984. Fault behavior and characteristic earthquakes: Examples from the Wasatch and San Andreas fault zones. *J. Geophys. Res.*, 89, 5681-5698.
- Schwarz, M. and A. Henk, 2004. Evolution and structure of the Upper Rhine Graben: insights from three-dimensional thermomechanical modeling. *Int. J. Earth Sci*, 94, doi:10.1007/s00531-004-0451-2.
- Segall P. and R. Harris, 1986. Slip Deficit on the San Andreas Fault at Parkfield, California, as Revealed by Inversion of Geodetic Data. *Science*, 233, 4771, 1409-1413.
- Seyferth M. and A. Henk, 2004. Syn-convergent exhumation and lateral extrusion in continental collision zones - insights from three-dimensional numerical models. *Tectonophysics*, 382, 1-29.
- Shilts, W.W., M. Rappol and A. Blais, 1992. Evidence of late and postglacial seismic activity in the Temiscouata-Madawaska Valley, Quebec-New Brunswick, Canada. *Can. J. Earth. Sci.*, 29, 1043-1059.
- Shimazaki, K. and T. Nakata, 1980. Time-predictable recurrence model for large earthquakes. *Geophys. Res. Lett.*, 7, 279-282.
- Stewart, S., J. Sauber and J. Rose, 2000. Glacio-seismotectonics: ice sheets, crustal deformation and seismicity. *Quat. Sci. Rev.*, 19, 1367-1389.
- Swan, F.H., 1988. Temporal clustering of paleoseismic events on the Oued Fodda Fault, Algeria. *Geology*, 16, 1092-1095.

- Swan F.H., D.P. Schwartz III and L.S.Cluff, 1980. Recurrence of moderate to large magnitude earthquakes produced by surface faulting on the Wasatch fault zone. *Utah. Seism. Soc. of Am. Bull.*, 70, 1431-1462.
- Talbot, C. J., 1999. Ice ages and nuclear waste isolation. *Engineering Geol.*, 52, 177-192.
- Talwani, P., 2000. Seismogenic properties of the crust inferred from recent studies of reservoir-induced seismicity – Application to Koyna. *Current Sci.*, 79, 1327-1333
- Thatcher, W., G.R. Foulger, B.R. Julian, J. Svarc, E. Quilty, and G.W Bawden, 1999. Present-day deformation across the Basin and Range province, western United States. *Science*, 283, 1714-1718.
- Turpeinen, H., A. Hampel, T. Karow and G. Maniatis, 2008. Effect of ice sheet growth and melting on the slip evolution of thrust faults. *Earth Planet. Sci. Lett.*, 269, 1-2,230-241, doi:10.1016/j.epsl.2008.02.017.
- Twiss, R.J., E.M. Moores, 1992. *Struktural Geology*. W.H. Freeman New York.
- Walcott, R.L., 1970. Flexural rigidity, thickness, and the viscosity of the lithosphere. *J. Geophys. Res.*, 75, 3941–3954.
- Wallace, R.E., 1987. Grouping and migration of surface faulting and variation in slip rates on faults in the Great Basin province. *Bull. Seismol. Soc. Am.*, 77, 868-877.
- Watts, A.B., 2001. *Isostasy and Flexure of the Lithosphere*. Cambridge Univ. Press, 458p.
- Wernicke, B., A.M. Friedrich, N.A. Niemi, R.A. Bennett and J.L. Davis, 2000. Dynamics of Plate Boundary Fault Systems from Basin and Range Geodetic Network (BARGEN) and Geologic Data. *GSA Today*, 10(11), 1–7.
- Wernicke, B., and Snow, J.K., 1998. Cenozoic tectonism in the central Basin and Range; motion of the Sierran. Great Valley block. *Intern. Geol. Rev.*, 40, 402-420.
- Willett, S.D., C. Beaumont and P. Fullsack 1993. Mechanical model for the tectonics of doubly vergent compressional orogens. *Geology*, 21, 371-374.
- Wu, P. and Hasegawa, H.S., 1996b. Induced stresses and fault potential in eastern Canada due to a realistic load: a preliminary analysis. *Geophys. J. Int.*, 127,215-229.
- Wu, P. and Hasegawa, H.S., 1996a. Induced stresses and fault potential in eastern Canada due to a disc load: a preliminary analysis. *Geophys. J. Int.*, 125, 415-430.
- Wu, P., P. Johnston and K. Lambeck, 1999. Postglacial rebound and fault instability in Fennoscandia, *Geophys. J. Int.*, 139, 657-670.
- Zoback M.L., M.D. Zoback, J. Adams, M. Assumpcao, S. Bell, E.A. Bergman, P. Blümling, N.R. Brereton, D. Denham, J. Ding, K. Fuchs, N. Gay, S. Gregersen, H.K. Gupta, A. Gvishiani, K. Jacob, R. Klein, P. Knoll, M. Magee, J.L. Mercier, B. Müller, C. Paquin, K. Rajendran, O. Stephansson, G. Suarez, M. Suter, A. Udias, Z.H. Xu and, M. Zhizhin, 1989. Global patterns of tectonic stress. *Nature*, 341, 291-298.

---

## Acknowledgements

First of all I would like to thank my supervisor Dr. Andrea Hampel for offering me the opportunity to undertake this project, being a member of her Emmy-Noether Research Group for Numerical Modeling of Tectonics and Surface Processes. I am sincerely thankful for her outstanding supervision and guidance throughout this study. Her valuable discussion, stimulating ideas as well as her outstanding motivation abilities are very much appreciated.

I would like to thank Prof. Dr. Bernhard Stöckhert for financial support at the beginning of my work, funded within the scope of the Collaborative Research Centre 526 (DFG).

I am also indebted to Dr. Georgios Maniatis for valuable discussion on fault kinematics and topics of modeling issues.

Further I like to thank I would like to thank Dr. Sandra Birtel, Dr. Jens Nüchter, Dr. Claudia Trepmann, and Dipl. Geol. Katharina Telenga for fruitful discussions as well as Dr. Klaus Röller for support in computational issues.

I am greatly indebted to M.Sc. Maren Hübers for thoughtful comments on the manuscript of this thesis.

The German Research Foundation (DFG) is gratefully acknowledged for funding this project in the framework of the Emmy-Noether program (grant HA 3473/2-1).

## Curriculum Vitae

### Personal Data

Date of birth	28.07.1978
Place of birth	Osnabrück
Nationality	German

### School

1985 - 1989	Theodor-Heuss-Schule, Osnabrück
1989 - 1991	Orientierungsstufe Sebastopol, Osnabrück
1991 - 1998	Ernst-Moritz-Arndt Gymnasium, Osnabrück

### Study

10/1999 - 6/2005	Study of Geology, Westfälische Wilhelms-Universität Münster
6/2005	Graduation as "Diplom-Geologe", Westfälische Wilhelms-Universität Münster

### Employment record

1/2006 – recent	Research assistant at the Ruhr-Universität Bochum
-----------------	--